

MAGNETIC FRUSTRATION IN THREE DIMENSIONS

Dissertation

zur Erlangung des akademischen Grades

Doctor rerum naturalium

(Dr. rer. nat.)

vorgelegt

dem Bereich Mathematik und Naturwissenschaften

der Technischen Universität Dresden

ROBIN SCHÄFER

geb. 25.07.1993 in Hagen-Hohenlimburg

MAGNETIC FRUSTRATION IN THREE DIMENSIONS

Robin Schäfer

ABSTRACT

Frustrated magnets realize exotic forms of quantum matter beyond conventional order. Due to a lack of controlled and unbiased methods to study frustration in three dimensions, many questions remain unanswered. While most established numerical techniques have limited applicability, approaches based on cluster expansions are promising alternatives. By design, they do not suffer from dimensionality or frustration and generate reliable insights into the thermodynamic limit without any restriction in the parameter space. This thesis makes significant methodological progress in controlled numerical approaches tailored to study frustration in three dimensions. It covers (i) an automatic detection algorithm for symmetries in generic clusters, (ii) a general approach to the numerical linked cluster algorithm to study finite – and zero – temperature properties, and (iii) an expansion method based on the linked cluster theorem to obtain a suitable dressing for valence-bond crystals.

In particular, we study one of the archetypal problems of frustrated magnetism in three dimensions: the pyrochlore Heisenberg antiferromagnet. For the first time, we are able to unbiasedly resolve its thermodynamic quantities to a temperature far beyond the scale on which the Schottky anomaly occurs. The broad applicability of the numerical linked cluster algorithm allows for the systematic investigation of different spin-liquid candidate materials such as the Cerium-based pyrochlores $\text{Ce}_2\text{Zr}_2\text{O}_7$ and $\text{Ce}_2\text{Sn}_2\text{O}_7$. Despite a similar chemical composition, the algorithm finds fundamental differences in their quantum mechanical nature by constraining their microscopic exchange parameters.

Zero temperature properties are even less accessible: Neither the nature of the ground state nor an estimate of its energy are known for the pyrochlore antiferromagnet. Large-scale density matrix renormalization group calculations pushed to three dimensions provide the first reliable estimate of its ground-state energy and yield robust evidence for a spontaneous inversion symmetry breaking manifesting itself as an energy density difference on the tetrahedral sublattice. The symmetry-breaking tendency of the model is further observed in the presence of an external magnetic field where similar calculations suggest a stable $1/2$ -magnetization plateau. Continuing the investigation of low-energy states, we propose a new family – exponentially numerous in the linear system size – of valence-bond crystals as potential ground states. Understanding the stability of the previously overlooked family of states suggests a remarkable change of perspective on frustration with a focus on unfrustrated motifs. In sum, these discoveries present significant progress towards resolving long-standing questions regarding the nature of the ground state of the quantum pyrochlore $S = 1/2$ antiferromagnet.

MAGNETIC FRUSTRATION IN THREE DIMENSIONS

Robin Schäfer

KURZFASSUNG

Frustrierte Magnete realisieren exotische Formen von Quantenmaterie, welche gewöhnliche Ordnungen übersteigen. Viele etablierte numerische Methoden versagen bei Frustration in drei Dimensionen, da sie entweder nicht anwendbar sind, unkontrolliert sind oder bestimmte Zustände vorziehen. Clusteralgorithmen bilden eine vielversprechende Alternative. Sie erfahren keine Einschränkung durch die Dimensionalität oder die Frustration des Problems und erlauben daher zuverlässige Einblicke in den thermodynamischen Limes. Diese Arbeit präsentiert methodische Fortschritte von kontrollierbaren Ansätzen, welche auf frustrierte Systeme in drei Dimensionen zugeschnitten sind. Sie beinhaltet (i) die Entwicklung eines Algorithmus zur automatischen Detektion räumlicher Symmetrien für allgemeine Cluster, (ii) einen allgemeinen Zugang zum “numerical linked cluster algorithm”, um Eigenschaften bei endlicher Temperatur und dem absoluten Nullpunkt zu studieren und (iii) einen Clusteralgorithmus zur Optimierung des Zustands eines “valence-bond” Kristalls.

Die methodischen Fortschritte dieser Arbeit tragen zur Lösung eines archetypischen Problems von frustriertem Magnetismus in drei Dimensionen bei: dem Pyrochlor Heisenberg Antiferromagnet. Sie erlauben zuverlässige Einblicke in die Thermodynamik bis hin zu nicht-trivialen Temperaturen weit unter der Schottky-Anomalie. Die weiten Anwendungsmöglichkeiten des Clusteralgorithmus macht die systematische Untersuchung von Spinflüssigkeitskandidaten, wie die auf Cer basierenden Pyrochlore $\text{Ce}_2\text{Zr}_2\text{O}_7$ und $\text{Ce}_2\text{Sn}_2\text{O}_7$, möglich. Trotz einer ähnlichen chemischen Komposition, findet der Algorithmus fundamentale Unterschiede in ihrer quantenmechanischen Struktur.

Frustration in drei Dimensionen ist am absoluten Nullpunkt ähnlich unzugänglich wie bei endlicher Temperatur und weder der Grundzustand, noch Schätzungen der Grundzustandsenergie des Pyrochlor Antiferromagneten sind bekannt. Groß angelegte Dichtematrixrenormierungsgruppenrechnungen in drei Dimensionen ermöglichen erstmals eine verlässliche Schätzung der Energie und finden eine spontan gebrochene Inversionssymmetrie, welche durch einen Unterschied in der Energiedichte auf dem tetraedrischen Untergitter ausgedrückt ist. Die Tendenz, die Symmetrie des Systems zu brechen, ist auch in der Präsenz eines externen magnetischen Feldes zu beobachten. Rechnungen deuten die Stabilität des $1/2$ -Magnetisierungsplateaus an. Einen signifikanten Beitrag zum Verständnis des Heisenberg-Modells auf dem Pyrochlor wird durch eine Familie von potentiellen Grundzuständen geleistet, welche als harte Hexagone im Gitter visualisiert werden können. Ihre Anzahl skaliert exponentiell in der linearen Systemgröße und ihre niedrige Energie eröffnet eine neue Sichtweise auf frustrierte Magnete, welche den Fokus auf unfrustrierte Geometrien lenkt. Im Widerspruch zu der prominenten Spinflüssigkeitsannahme deuten die Ergebnisse dieser Arbeit auf Ordnung im Pyrochlor Antiferromagneten hin.

ACKNOWLEDGEMENTS

Words cannot express my gratitude for the many people who supported me throughout my PhD journey. First and foremost, this endeavor would not have been possible without the continuous and patient supervision of Prof. David J. Luitz. He generously provided knowledge and expertise to help me navigate my research projects. I am also deeply indebted to Prof. Roderich Moessner whose ideas shaped both my scientific thinking as well as my projects in an important way. Special thanks to Dr. Owen Benton for his guidance throughout the last year of my PhD as well as Benedikt Placke for sharing his knowledge with me. I would also like to acknowledge Dr. Imre Hagymasi and Prof. Jan C. Budich for fruitful collaboration and tremendous support. I am thankful to everyone within the Max Planck Institute for the Physics of Complex Systems for creating the infrastructure for innovative research and a great work environment. In particular, I would like to mention Hubert Scherrer-Paulus for his outstanding IT support in many situations. Finally, my scientific career would not have taken this path without Prof. Joachim Stolze, who guided me from my Undergraduate Education up to this day.

I would like to express my deepest appreciation for my family and friends for their support throughout the last four years. I am grateful for my parents, Heike and Carsten Schäfer, whose love and guidance are always with me. Special thanks to my grandmother, Helga Budde, for being always available to talk and take my mind off things for a while. My paternal grandparents, Wolfgang and Christiane Schäfer, supported my curiosity since I was young. Unfortunately, Wolfgang passed away in 2020 but I know that he is very proud of me. I am also grateful for my sister Lena Schäfer as well as her partner Rahul Bhui for their tremendous help. I hope to continue to profit from their scientific advice but most importantly from their friendship. I could not have undertaken this journey without my fiancée, Pauline Glaß – I am unable to describe her support in words.

PUBLICATIONS

- [1] **Pyrochlore $S = \frac{1}{2}$ Heisenberg antiferromagnet at finite temperature**
[Phys. Rev. B 102, 054408 \(2020\)](#)
R. Schäfer, I. Hagymási, R. Moessner, and D. J. Luitz
- [2] **Possible Inversion Symmetry Breaking in the $S = 1/2$ Pyrochlore Heisenberg Magnet**
[Phys. Rev. Lett. 126, 117204 \(2021\)](#)
I. Hagymási, R. Schäfer, R. Moessner, and D. J. Luitz
- [3] **Case for a $U(1)_\pi$ Quantum Spin Liquid Ground State in the Dipole-Octupole Pyrochlore $\text{Ce}_2\text{Zr}_2\text{O}_7$**
[Phys. Rev. X 12, 021015 \(2022\)](#)
E. M. Smith, O. Benton, D. R. Yahne, B. Placke, R. Schäfer, J. Gaudet, J. Dudemaine, A. Fitterman, J. Beare, A. R. Wildes, S. Bhattacharya, T. DeLazzer, C. R. C. Buhariwalla, N. P. Butch, R. Movshovich, J. D. Garrett, C. A. Marjerrison, J. P. Clancy, E. Kermarrec, G. M. Luke, A. D. Bianchi, K. A. Ross, and B. D. Gaulin
- [4] **Magnetization process and ordering of the $S = 1/2$ pyrochlore Heisenberg antiferromagnet in a magnetic field**
[Phys. Rev. B 106, L060411 \(2022\)](#)
I. Hagymási, R. Schäfer, R. Moessner, and D. J. Luitz
- [5] **Symmetry protected exceptional points of interacting fermions**
[Phys. Rev. Research 4, 033181 \(2022\)](#)
R. Schäfer, J. C. Budich, and D. J. Luitz
- [6] **Abundance of hard-hexagon crystals in the quantum pyrochlore antiferromagnet**
[10.48550/ARXIV.2210.07235 \(2022\)](#)
R. Schäfer, B. Placke, O. Benton, and R. Moessner

- [7] **Dipolar spin ice regime proximate to an all-in-all-out Néel ground state in the dipolar-octupolar pyrochlore $\text{Ce}_2\text{Sn}_2\text{O}_7$**

[10.48550/ARXIV.2211.15140 \(2022\)](#)

D. R. Yahne, B. Placke, R. Schäfer, O. Benton, R. Moessner, M. Powell, J. W. Kolis, C. M. Pasco, A. F. May, M. D. Frontzek, E. M. Smith, B. D. Gaulin, S. Calder, and K. A. Ross

PREFACE

This thesis is separated into two parts: the methodical development and its application.

[Part I](#) introduces the computational quantum many-body problem and discusses algorithms tailored to frustrated magnetism in three dimensions derived in this thesis.

[Chapter 1](#) – [The many-body problem of quantum mechanics](#)

[Chapter 2](#) – [Controlled methods advanced in this thesis](#)

Their application to the pyrochlore Heisenberg antiferromagnet – the archetype of frustration in three dimensions – is discussed in [Part II](#). After a brief introduction to the pyrochlore model and its exotic phenomena, it individually covers insights into its finite and zero temperature properties.

[Chapter 3](#) – [The pyrochlore Heisenberg antiferromagnet ...](#)

[Chapter 4](#) – [... at finite temperature](#)

[Chapter 5](#) – [... and zero temperature](#)

Only the advancements from [Part I](#) make the physical results presented in [Part II](#) possible.

Note that Ref. [\[5\]](#) was obtained as a part of this thesis but is not discussed here.

TABLE OF CONTENTS

ABSTRACT	ii
ACKNOWLEDGEMENTS	v
PUBLICATIONS	vii
PREFACE	ix
TABLE OF CONTENTS	ix
 I COMPUTATIONAL QUANTUM MANY-BODY PHYSICS	 1
1 The many-body problem of quantum mechanics	3
1.1 Magnetism in solids	5
1.2 Quantum mechanics and spin systems	8
1.3 Many-body problem and numerical techniques	13
2 Controlled methods advanced in this thesis	17
2.1 Symmetries in spin systems	19
2.2 Numerical linked cluster expansions	35
2.3 Cluster expansion for exponentials	46
 II THE ARCHETYPE OF FRUSTRATED MAGNETISM	 55
3 The pyrochlore Heisenberg antiferromagnet ...	57
3.1 Spin liquids	59
3.2 Quantum spin ice	61
3.3 Materials	65

4	... at finite temperature	67
4.1	Thermodynamics in spin systems	68
4.2	Thermodynamics of the pyrochlore Heisenberg antiferromagnet	72
4.3	The dipolar-octupolar $\text{Ce}_2\text{Zr}_2\text{O}_7$ and $\text{Ce}_2\text{Sn}_2\text{O}_7$	83
5	... and zero temperature	97
5.1	Possible inversion symmetry breaking	98
5.2	Magnetization process and ordering	104
5.3	Hard-hexagon crystal	109
6	CONCLUSION AND OUTLOOK	121
	LIST OF TABLES	xiii
	LIST OF ILLUSTRATIONS	xvi
	BIBLIOGRAPHY	xvi

Part I

**COMPUTATIONAL QUANTUM
MANY-BODY PHYSICS**

Chapter 1

THE MANY-BODY PROBLEM OF QUANTUM MECHANICS

A condensed matter physicist's task is to predict properties of macroscopically large systems characterized by a vast amount of, sometimes quite exotic, degrees of freedom. These are diverse and can be described within various frameworks such as first principle calculations, quasi-particle descriptions, or effective theories that already simplify the initial problem. In particular, solid-state physics studies crystalline materials where already a few grams contain up to $\sim 10^{24}$ atoms exhibiting different degrees of freedom. To grasp the enormity of that number, note that the current population of humanity just reached $8 \cdot 10^9$ [8], and a conservative estimate of ants on earth is $2 \cdot 10^{16}$ [9]. Despite this enormous number, we know how to deal with this problem *classically* and even *quantum mechanically* – *in principle*. In the non-relativistic limit of quantum mechanics, which is a valid approximation in many cases, all particles (*e.g.* nuclei and electrons) interact via electromagnetism described by a Hamiltonian operator. The Hamiltonian defines all thermodynamic properties, and Schrödinger's equation [10, 11] governs the dynamics of this macroscopically large system. Without interactions between particles, simple solutions exist even for systems containing a vast number of particles. Indeed, in that case, either an efficient sampling or an analytical calculation permits predictions as the problem collapses into many, but individual particles and properties of the whole system are expressed by summing over single-particle properties. The story drastically complicates if interactions enter the stage. Given the exponentially increasing complexity of generic interacting systems in quantum mechanics, a direct calculation is hopeless.

As Philip W. Anderson emphasized in his seminal article, *More is Different* [12], collective processes give rise to the exotic phenomena found in condensed matter systems. While quantum mechanical solutions are exponentially hard to obtain, interactions allow for correlation effects between particles that are responsible for these collective many-body processes. Indeed, the fascinating phases found in condensed matter do not emerge from individual properties of the single particles: the essential ingredients are collective phenomena emerging from the interactions between many particles.

Based on experimental advances and novel theoretical approaches, the condensed matter community made significant progress towards a better understanding of interacting many-body systems. While many theoretical insights are obtained by pen and paper calculations, our limited mathematical capabilities do not allow for an analytic solution to the quantum many-body problem. Starting in 1953 [13], the growing technological development in the *Information Age* began entering all areas of science. This opened up the possibility to derive new insights that were previously inaccessible and led to the development of a new field: *computational physics*! Today's progress in theoretical condensed matter physics is based on uniting analytical theories, powerful numerical capacities, and highly optimized algorithms that are tailored to specific problems.

The contribution of this thesis is clearly in the latter field – the algorithmic development – which is discussed in [Part I](#). It presents methodological advances that permit the investigation of exotic phenomena associated with frustration in three dimensions at finite and zero temperatures. The combination of three-dimensionality and frustration limits the use of established techniques and thus calls for improvements in generating reliable insights into these long-standing problems.

This chapter provides an introduction into magnetism in solids and its quantum mechanical description which causes the many-body problem. The first section briefly motivates the origin of microscopic magnetic moments in crystalline materials, introduces suitable mathematical models describing it, and discusses the typical features of magnetic systems. The quantum mechanical formulation is presented in the second section and introduces notations used throughout this thesis. This formulation reveals the exponential complexity induced by quantum mechanics. Hence, the third section provides a brief overview of commonly used techniques to study quantum magnetism using statistical methods, approximate methods, and numerical brute force.

1.1 Magnetism in solids

While Maxwell's theory of electrodynamics treats the electric and magnetic fields as continuous variables, the theoretical approach to magnetism in solids is discrete. Ions are placed in fixed positions according to the crystal structure of the specific material and attract electrons filling up the atomic shells. Individual magnetic moments arise from partially filled shells of these ions. The precise nature of these moments and their interactions depend on various microscopic processes, the Pauli exclusion principle [14], phononic excitations, the electron's wavefunction, other symmetries like time-reversal, and many more [15, 16, 17, 18]. Further, relativistic effects of the electrons induce spin-orbit coupling [19, 20], which, together with the surrounding electric crystal field [21, 22], generate anisotropies breaking some symmetries of the model. Hence, magnetism in solids is described by localized moments with interactions depending on diverse microscopic details.

Many simplifications are made to arrive at toy models suited for theoretical studies. While these approximations are based on legitimate arguments like well-separated energy scales, they should not be taken for granted and should be validated on a case-by-case basis. Therefore, theory and experiments have to go hand in hand to provide and improve our current understanding of magnetism. Experiments on the scale of quantum effects require high-quality samples and advanced technological equipment to verify the theoretical simplifications. The connection between experiment and theory is illustrated in Section 4.3, which presents an extensive analysis of experimental results obtained from the rare-earth pyrochlores $\text{Ce}_2\text{Sn}_2\text{O}_7$ and $\text{Ce}_2\text{Zr}_2\text{O}_7$ [3].

Both numerical and analytical calculations require a well-defined mathematical framework describing the magnetic moments and the interactions among them. The most prominent model of classical magnetism is the n -vector model, also known as the $O(n)$ model. The individual magnets exhibit a fixed length associated with their moment and orientation characterized by an n -component vector $\mathbf{S}_i \in \mathbb{R}^n$. Fixing the magnitude of each moment, often also called spin, induces $n - 1$ continuous degrees of freedom represented on an n -dimensional sphere. The Ising model ($n = 1$), the XY-model ($n = 2$) and the classical Heisenberg model ($n = 3$) are frequently studied. The Hamilton formalism governs the classical equations of motion. As long as no time-dependent constraints are present, the Hamilton function H , also called Hamiltonian, determines the system's total energy in generalized coordinates. It is derived as the Legendre transformation of the Lagrange function of the system. In the case of magnetic moments, a simple Hamiltonian depends on the orientation of the individual spins \mathbf{S}_i :

$$H = J \sum_{\langle i, j \rangle} \mathbf{S}_i \cdot \mathbf{S}_j + \sum_i \mathbf{h} \cdot \mathbf{S}_i \text{ with } \|\mathbf{S}_i\| = 1 \quad (1.1)$$

Both the global coupling constant J and the external field \mathbf{h} are in units of energy. The sum runs over a collection of edges $\langle i, j \rangle$, defining a graph on which two moments can interact. The model can include more complex anisotropic exchanges J_{ij} and external fields \mathbf{h}_i . The Hamiltonian

exhibits a global continuous $O(n)$ -symmetry for $n > 1$ and $\mathbf{h} = \mathbf{0}$ as the scalar product between two vectors is invariant under a global rotation. The continuous symmetry is replaced by a discrete one for $n = 1$ where the spins simply point in either of two directions.

As Philip W. Anderson emphasized [12], the exciting phenomena in condensed matter do not arise from a simple collection of single isolated moments; the crucial ingredient is the interaction between these microscopic magnets. Various types of interactions provide a fertile ground for possible collective behaviors and exotically ordered and disordered magnetic phases [23, 24, 25]. Even in the classical case, determining these phases is far from trivial and is strongly model-dependent. Predicting specific phases includes many ingredients like lattice geometry, dimensionality, or the underlying symmetry of the interaction, *e.g.* discrete or continuous.

Phase transitions of physical systems are driven by temperature. At temperatures that are much larger than the interaction strength, all spins are essentially uncorrelated, and thermal fluctuations prevent the system from ordering. The system is in the disordered *paramagnetic* phase. Individual particles can be essentially viewed as independent similar to a *gas* where all thermodynamic properties are derived from thermal distributions of single-particle quantities. Lowering the temperature induces correlations between the moments and enables the possibility of ordering or more complex collective phenomena to occur. If a system favors a particular order, it undergoes a phase transition from the paramagnetic phase into an ordered state at finite or zero temperature. At zero temperature, the system realizes the *ground state*, the lowest possible energy configuration allowed by the Hamiltonian. An important question concerns the degeneracy of the ground state. It can be uniquely defined or degenerated, meaning multiple configurations exhibit the same lowest energy. The degenerate manifold can contain a finite number or even macroscopically many states [26, 27, 28]. The ground state(s) or even low energy configurations often possess some kind of order which goes along with a broken symmetry. Landau's theory [29, 30, 31, 32, 33] describes the transitions from a paramagnetic phase into an ordered state in terms of an order parameter associated with the broken symmetry. Typical order parameters are the magnetization per site and the correlation between different moments, but they can also involve more complex operators. Some condensed matter systems host more exotic transitions beyond Landau's paradigm involving, for example, topological order [34, 35].

The most prominent examples of ordered states are the ferromagnet and the antiferromagnet. In the ferromagnetic case, $J < 0$, the energy of H is minimized if $\mathbf{S}_i \cdot \mathbf{S}_j = 1$, which corresponds to an alignment of neighboring spins. The corresponding ferromagnetic order parameter is the total magnetization, and the critical transition temperature is known as Curie temperature [36]. For example, a ferromagnetic interaction in magnetite, Fe_3O_4 , favors an alignment of magnetic moments, inducing the spontaneous magnetization of the material below the critical temperature. In contrast, antiferromagnetic couplings, $J > 0$, minimize the energy if $\mathbf{S}_i \cdot \mathbf{S}_j = -1$, which corresponds to an anti-alignment of neighboring spins. This configuration, known as the Néel state, is realized on bipartite lattices. They can be decomposed into two sublattices, \mathcal{A} and \mathcal{B} , such that sites in \mathcal{A} are only adjacent to sites in \mathcal{B} and vice versa. The corresponding

critical temperature is the Néel temperature [37, 38]. A system is geometrically frustrated if a non-bipartite lattice exhibits antiferromagnetic couplings. Then, not all exchange terms in Equation 1.1 can be minimized simultaneously, and the system fails to host a simple Néel order. This yields a complex low-energy landscape and a plethora of exotic phenomena, as discussed in Chapter 3. Frustration occurs in both classical and quantum systems. The following section introduces the basic notations used in quantum magnetism.

1.2 Quantum mechanics and spin systems

Following Richard P. Feynman’s famous quote¹, treating magnetic moments classically is insufficient, as nature follows the laws of quantum mechanics on an atomic level. Starting from 1923, many brilliant physicists, like de Broglie [40, 41], Heisenberg [42, 43, 44, 45], Schrödinger [10], Dirac [46, 47], Pauli [48, 14], and many more [49, 50, 51, 52, 53], have established the theory of quantum mechanics we know today. The first revolution of quantum mechanics faced many obstacles and skepticism as it contradicts established theories and launched an entirely new perspective. More and more seminal experiments confirmed the ideas of quantum mechanics, thereby reshaped our understanding of nature [54, 55, 56, 57].

Elementary particles building up the matter surrounding us carry an internal degree of freedom called *spin* [58]: $= 1/2, 1, 3/2, \dots$. In quantum mechanics, an electron is described by a wavefunction referring to its probability distribution in space and time as well as a spin degree of freedom ($S = 1/2$) which can point “up” $|\uparrow\rangle$ and “down” $|\downarrow\rangle$. In contrast to classical physics, quantum mechanics allows a superposition of possible configurations with a probabilistic interpretation [49, 59, 60, 61]:

$$|\Psi\rangle = \alpha|\uparrow\rangle + \beta|\downarrow\rangle, \text{ with } \alpha, \beta \in \mathbb{C} \text{ and } |\alpha|^2 + |\beta|^2 = 1 \quad (1.2)$$

A measurement aiming at the orientation of the spin, up or down, results in probabilities, $|\alpha|^2$ or $|\beta|^2$, obtained from the respective *amplitudes*. This induces the collapse of the wavefunction to the eigenstate associated with the measurement result.

Mathematically, the states $|\uparrow\rangle$ and $|\downarrow\rangle$ form the basis of a two-dimensional Hilbert state. While we refer to the basis vectors as *ket* states, their *dual* vectors are known as *bra* states, $\langle\uparrow|$ and $\langle\downarrow|$, fulfilling the orthogonality relation:

$$\langle\uparrow|\uparrow\rangle = 1, \langle\downarrow|\downarrow\rangle = 1, \langle\uparrow|\downarrow\rangle = 0 \text{ and } \langle\downarrow|\uparrow\rangle = 0 \quad (1.3)$$

Instead of a representation using arrows, $|0\rangle$ and $|1\rangle$ are frequently used such that the orthogonality relation can be expressed using the *Kronecker-delta* $\langle i|j\rangle = \delta_{ij}$. The corresponding bra vectors are used to define the dual vector $\langle\Psi|$ associated with the state vector $|\Psi\rangle$ such that $\langle\Psi|\Psi\rangle = 1$

$$\langle\Psi| = \bar{\alpha}\langle\uparrow| + \bar{\beta}\langle\downarrow|. \quad (1.4)$$

Quantum mechanical states are defined modulo a global phase $e^{i\varphi} \in U(1)$ as it does not violate the probabilistic interpretation and the normalization $\langle\Psi|\Psi\rangle = 1$. The state of a classical Heisenberg spin ($n = 3$ vector model) is represented on the three-dimensional Bloch sphere, and

¹ *Nature isn’t classical, dammit, and if you want to make a simulation of nature, you’d better make it quantum mechanical, and by golly it’s a wonderful problem, because it doesn’t look so easy* [39].

the vector exhibits two continuous degrees of freedom [62, 63]. Similarly, the quantum mechanical state of a spin-1/2 is analogously defined on a Bloch sphere. Reducing the ambiguity induced by the global $U(1)$ phase by choosing a specific gauge and using the normalization, both amplitudes α and β are uniquely defined using a three-dimensional sphere. The sphere is parameterized by two angles $\varphi \in [0, 2\pi)$ and $\theta \in [0, \pi)$:

$$|\Psi\rangle = \cos(\theta/2)|\uparrow\rangle + e^{i\varphi} \sin \theta/2|\downarrow\rangle \quad (1.5)$$

The measurement of an observable is associated with a linear and hermitian operator. The space of possible operators that act on the state of a spin-1/2 particle is generated from the $SU(2)$ algebra defined by the Pauli matrices [14]

$$\sigma^x = \begin{pmatrix} 0 & 1 \\ 1 & 0 \end{pmatrix}, \sigma^y = \begin{pmatrix} 0 & i \\ -i & 0 \end{pmatrix}, \text{ and } \sigma^z = \begin{pmatrix} 1 & 0 \\ 0 & -1 \end{pmatrix}. \quad (1.6)$$

The specific choice of matrices has useful properties as they are involutory, $\sigma_0 = \sigma^{\alpha^2} = \mathbb{1}_2$, their determinants are -1 , $\det(\sigma^\alpha) = -1$, and they are traceless, $\text{Tr}(\sigma^\alpha) = 0$. The notation via x , y , and z refers to the representation of a state on the three-dimensional Bloch sphere, whereas σ^α corresponds to a π -rotation around the α -axis.

In the following, the state $|\uparrow\rangle$ ($|\downarrow\rangle$) is associated with the north (south) pole in the z -direction. Since $SU(2)$ is a non-abelian group, the Pauli operators, similar to angular momentum operators, follow a non-trivial commutation relation:

$$[\sigma^\alpha, \sigma^\beta] = \sigma^\alpha \sigma^\beta - \sigma^\beta \sigma^\alpha = 2i\varepsilon_{\alpha\beta\gamma} \sigma^\gamma \quad (1.7)$$

$$\{\sigma^\alpha, \sigma^\beta\} = \sigma^\alpha \sigma^\beta + \sigma^\beta \sigma^\alpha = 2\delta_{\alpha\beta} \mathbb{1}_2 \quad (1.8)$$

The *Levi-Civita* symbol $\varepsilon_{\alpha\beta\gamma} \in \{-1, 0, 1\}$ is an extension of the Kronecker-symbol $\delta_{\alpha\beta} \in \{0, 1\}$.

It is useful to introduce the non-hermitian ladder operators:

$$\sigma^\pm = \frac{1}{2} (\sigma^x \pm i\sigma^y) \quad \Rightarrow \quad \sigma^+ = \begin{pmatrix} 0 & 1 \\ 0 & 0 \end{pmatrix} \text{ and } \sigma^- = \begin{pmatrix} 0 & 0 \\ 1 & 0 \end{pmatrix} \quad (1.9)$$

We usually use spin operators $S^\alpha = 1/2 \sigma^\alpha$ and $S^\pm = \sigma^\pm$ for $S = 1/2$. More generally, higher spin- S representations contain $2S + 1$ states: $|S; m\rangle$ with $m = -S, \dots, S - 1, S$.

Their spin operators are defined as follows:

$$\langle S; m' | S^x | S; m \rangle = (\delta_{m'm+1} + \delta_{m'+1m}) \frac{1}{2} \sqrt{S(S+1) - m'm} \quad (1.10)$$

$$\langle S; m' | S^y | S; m \rangle = (\delta_{m'm+1} - \delta_{m'+1m}) \frac{1}{2i} \sqrt{S(S+1) - m'm} \quad (1.11)$$

$$\langle S; m' | S^z | S; m \rangle = \delta_{m'm} m \quad (1.12)$$

$$\langle S; m' | S^+ | S; m \rangle = \delta_{m'm+1} \sqrt{S(S+1) - m'm} \quad (1.13)$$

$$\langle S; m' | S^- | S; m \rangle = \delta_{m'+1m} \sqrt{S(S+1) - m'm} \quad (1.14)$$

$$\langle S; m' | \mathbf{S} \cdot \mathbf{S} | S; m \rangle = \delta_{m'm} S(S+1) \quad (1.15)$$

The total spin operator, also known as *Casimir* operator, is $\mathbf{S} \cdot \mathbf{S}$ with $\mathbf{S} = \begin{pmatrix} S^x & S^y & S^z \end{pmatrix}$. It represents, together with *one* generator S^α , the maximal commuting subset of the $SU(2)$ algebra in representation theory. This is discussed in [Section 2.1](#).

The introduced mathematical framework can be extended to multiple particles, allowing us to define toy models describing the interplay of many particles. Let $|\Psi_i\rangle$ denote a normalized quantum mechanical state of a spin-1/2, then the state of the whole system $|\Psi\rangle$ composed of N *identical* particles is given by their tensor product:

$$|\Psi\rangle = \bigotimes_{i=1}^N |\Psi_i\rangle = |\Psi_1\rangle \otimes \cdots \otimes |\Psi_N\rangle \quad (1.16)$$

In the case of spin-1/2 particles, where a single-particle state is described as a normalized vector in \mathbb{C}^2 , the whole state of N spins is a normalized vector in \mathbb{C}^{2^N} . The tensor product induces an exponentially growing vector space. Similar to the physical state, an operator acting on the whole system is defined by the tensor product of individual Pauli operators. Each hermitian operator O acting on the exponentially large Hilbert space can be represented by a linear combination of different *Pauli strings*:

$$O = \sum_{\{\alpha_1, \dots, \alpha_N\}} c_{\{\alpha_1, \dots, \alpha_N\}} \bigotimes_{i=1}^N \sigma^{\alpha_i} \text{ with } \alpha_i = 0, x, y, z \quad (1.17)$$

The hermiticity requires $c_{\{\alpha_1, \dots, \alpha_N\}} \in \mathbb{R}$. Most operators of interest are local such that many σ_{α_i} are given by identity $\mathbb{1}_2$ and leave a specific site unchanged. A local operator acting only on a single site i is defined by:

$$\sigma_i^\alpha = \mathbb{1}_2 \otimes \cdots \otimes \underbrace{\sigma^\alpha}_{\text{site } i} \otimes \cdots \otimes \mathbb{1}_2 \quad (1.18)$$

Operators acting on different sites commute: $[\sigma_i^\alpha, \sigma_j^\beta] = 2i\delta_{ij}\varepsilon_{\alpha\beta\gamma}\sigma^\gamma$.

Constructing a realistic Hamiltonian of microscopic particles is non-trivial. One of the most

straightforward approaches to describe electrons in a crystal is the Hubbard model, where electrons exhibit a spin degree of freedom and can move between fixed positions in the lattice. Further constraints are induced by the Pauli exclusion principle forbidding two electrons with the same spin at the same position and Coulomb repulsion inducing an energy penalty if two electrons with opposite spin are at the same position. At half filling and in the limit of strong repulsion, the low-energy states are known as Mott insulators, and their effective low-energy theory includes only the spin degrees of freedom leading us to the most prominent approach to quantum magnetism: the Heisenberg model [45, 64].

The simplest nearest-neighbor Heisenberg Hamiltonians are:

$$H_{XYZ} = J_x \sum_{\langle i,j \rangle} S_i^x S_j^x + J_y \sum_{\langle i,j \rangle} S_i^y S_j^y + J_z \sum_{\langle i,j \rangle} S_i^z S_j^z \quad (1.19)$$

$$H_{XXZ} = J_{\pm} \sum_{\langle i,j \rangle} (S_i^x S_j^x + S_i^y S_j^y) + \Delta \sum_{\langle i,j \rangle} S_i^z S_j^z \quad (1.20)$$

$$H_{XXX} = J \sum_{\langle i,j \rangle} (S_i^x S_j^x + S_i^y S_j^y + S_i^z S_j^z) = J \sum_{\langle i,j \rangle} \mathbf{S}_i \cdot \mathbf{S}_j \quad (1.21)$$

The first Hamiltonian, H_{XYZ} , is the most general among the three and does not preserve any symmetry in spin space. H_{XXZ} and H_{XXX} conserve the total magnetization, which follows from $S_i^x S_j^x + S_i^y S_j^y = \frac{1}{2} (S_i^+ S_j^- + S_i^- S_j^+)$, but can also be shown using the commutation relations defined in Equation 1.7. The isotropic Heisenberg model, H_{XXX} , incorporates a global $SU(2)$ symmetry. Additional symmetries and their implementation are discussed in detail in Section 2.1 as they reduce the complexity of the problem.

The quantum mechanical Hamiltonian H , as its classical counterpart, determines the energy of a system. The energy of a state $|\Psi\rangle$ is its expectation value with respect to the Hamiltonian

$$E = \frac{\langle \Psi | H | \Psi \rangle}{\langle \Psi | \Psi \rangle}. \quad (1.22)$$

Expectation values of arbitrary observables like total magnetization or correlation functions are evaluated similarly. The Hamiltonian determines the partition function and free energy and, therefore, the thermodynamic properties of the system.

Different formalisms describe the evolution of a quantum mechanical system in time. Werner Heisenberg introduced the matrix mechanics [42, 65, 50], Richard Feynman developed the path integral formalism [66, 67] and Paul Dirac formulated the relativistic description [46]. In condensed matter, where relativistic effects can often be neglected, the Schrödinger equation [10, 11] governs the evolution of a quantum mechanical state $|\Psi(t)\rangle$:

$$i\hbar \frac{d}{dt} |\Psi(t)\rangle = H |\Psi(t)\rangle \quad (1.23)$$

$\hbar \approx 1.054 \cdot 10^{-34} \text{JHz}^{-1}$ is the reduced Planck constant which will be set to one throughout

this thesis. The equation is particularly simple if we have access to the eigenspectrum of the Hamilton operator acting on a D -dimensional Hilbert space:

$$H|\Psi_i\rangle = E_i|\Psi_i\rangle \text{ for } i = 1, \dots, D \text{ with } E_1 \leq \dots \leq E_D \quad (1.24)$$

$$|\Psi(t=0)\rangle = \sum_{i=1}^D c_i |\Psi_i\rangle \text{ induces } |\Psi(t)\rangle = \sum_{i=1}^D c_i e^{-iE_i t/\hbar} |\Psi_i\rangle \quad (1.25)$$

The hermiticity of the Hamiltonian operator ensures the orthogonality and completeness of its eigenstates. The eigenstates do not only determine the evolution in time but also the thermodynamic properties of a quantum system. Hence, knowing the full spectrum allows us to evaluate all properties of the system. However, analytical solutions offering the full spectrum or only the ground state for interacting many-body systems are rare. Hans Bethe derived the solution [64] for the one-dimensional spin-1/2 isotropic Heisenberg model in Equation 1.21. Another famous analytical solution is the AKLT state [68], which is represented as a matrix-product state. Further important solvable models are the Kitaev model on the honeycomb [69] and the toric code [70], both introduced by Alexei Kitaev, which realize a quantum spin-liquid phase at low temperatures. Even the simplest interacting Hamiltonians face the exponential complexity induced by quantum mechanics. The scaling is induced by the tensor product in Equation 1.16, defining the Hilbert space of N quantum mechanical spins. It leads to exponential growth, *e.g.* $D = 2^N$ for a spin-1/2 system, making straightforward computational and analytical approaches in the full Hilbert space impossible for many particles.

This is the *quantum many-body problem*.

1.3 Many-body problem and numerical techniques

When analytical approaches are exhausted, a computational physicist tries to derive properties of interacting many-body systems using numerical methods – despite their exponential complexity. To do so, the field of computational physics offers a variety of different numerical methods aiming at different problems. Some applications were imported from other fields, many were heavily optimized or even developed within the condensed matter community. Choosing the appropriate algorithm is crucial since each has advantages and disadvantages. The correct choice depends on the model and the quantity of interest. In condensed matter, areas of interest are quantum magnetism, such as the Heisenberg Hamiltonians in [Equation 1.19](#) to [Equation 1.21](#), correlated electrons, dissipative systems, quantum simulators, driven systems, and many more. Possible quantities to study in these systems are the ground state, its excitations as well as finite-temperature properties in and out of equilibrium. Also, dynamical properties like the evolution in time, information spreading, or dissipation rates are frequently studied. This section presents a brief overview of the most important techniques for strongly correlated problems: (i) *quantum Monte Carlo* (QMC), (ii) *matrix-product state* (MPS) methods and (iii) *exact diagonalization* (ED).

(i) Quantum Monte Carlo If applicable, MC-based methods serve as an extremely powerful tool to study classical and quantum systems in arbitrary dimensions. The name refers to the famous casinos in Monte Carlo as a similar mechanism applies. Even if some people win and extract money from the casino, averaging over many bets yields a predictable outcome: *The house always wins!*

Similar to the concept of casinos, the MC-based algorithms generate an enormous number of samples such that observables are evaluated on average. Even if certain samples generate unexpected results, according to stochastics, the observable will converge to its correct value – if the number of samples is *large* enough.

This raises several questions: What does large mean in this context? What is the scaling of the computational complexity? How to generate *good* samples and evaluate them efficiently? Answering these questions is not trivial as they depend on the model, temperature, system size, and the specific method. There is a *zoo* of different MC methods suited to different quantum systems. Nevertheless, there are some general statements regarding computational complexity. Taking the *stochastic series expansion* (SSE) [[71](#), [72](#), [73](#)] as an example, the world line length increases linearly with inverse temperature β , and so does the computational complexity. In addition, the system size enters linearly inducing a cubic scaling in three dimensions. While sampling the high-temperature regime is trivial, generating reliable low-temperature data involves large computational power. Smart sample updates suited to specific problems induce a considerable speedup necessary to study systems with a complicated low-energy landscape [[74](#)].

While the algorithm allows for an efficient determination of thermodynamic quantities in

arbitrary dimensions, it faces a fundamental limitation induced by its probabilistic nature. The anti-commutation relation of fermions and frustrated spin models induce the infamous *sign problem* [75]. This generically prohibits QMC in frustrated models such as the pyrochlore Heisenberg antiferromagnet. It is, however, possible to overcome the sign problem for certain unfrustrated parameter regimes permitting the application to frustrated lattices with ferromagnetic transverse couplings [76, 77]. More details on MC based methods can be found in Ref. [78, 79, 80, 81, 82].

(ii) Matrix-product states Steve R. White introduced the *density-matrix-renormalization-group* (DMRG) algorithm in 1992 to examine the ground state of one-dimensional problems [83, 84]. This soon became the method of choice for one-dimensional strongly correlated systems [85, 86, 87], and its connection to MPS was realized shortly after [88, 89]. Even though MPSs cover only a tiny fraction of the exponentially large Hilbert space, most relevant states are represented extremely well.

The MPS formalism is one-dimensional. Applying it to higher dimensions requires linearizing the system and embedding a one-dimensional *snake* topology, which comes at the cost of long-range interactions. The great success in one-dimensional systems (ground states up to machine precision) is not observed in higher dimensions as the computational complexity grows exponentially with system size. Soon it was realized that the inability to capture ground states in higher dimensions originates from the fundamentally different scaling of entanglement in quantum many-body systems, which follows an area law [90, 91, 92, 93]. Nevertheless, the method still serves as a powerful tool in two- and even three-dimensional systems [94, 2, 4, 95, 6]. The MPS formalism allows for extensions beyond DMRG. Since 2004, many algorithms for real- [96, 97, 98] and imaginary-time evolution [99, 100] have been proposed. Assuming translational invariance, some ideas can be generalized for an infinite system [101, 102, 103]. Even though MPS-based approaches have led to remarkable findings over past decades, they do not provide the ultimate tool we are looking for. MPS methods are biased towards low-entangled (often ordered) states. Therefore, reliable calculations in more than one dimension require careful finite-size scaling, extrapolation in the bond dimension and truncated weight. Additionally, various initial states and, importantly, different linearizations of the system must be considered since the one-dimensional topology crucially influences the performance.

To overcome the one-dimensional nature of the algorithm and its limitations, generalizations of the method are desirable. Higher-dimensional tensor networks offer this opportunity, but contracting these networks is computationally highly demanding [104]. The great success of MPS-based methods in quantum physics led to the development of state-of-the-art libraries like ITensor [105], providing a large toolbox for various applications utilized within this thesis. Further details can be found in Ref. [85, 87, 80, 105].

(iii) Exact diagonalization The great advantage of ED-based methods is their applicability without being biased towards weakly entangled states or fundamental limitations like the sign problem.

The Hamiltonian is a linear operator in an exponentially large Hilbert space. ED accepts the exponential complexity in system size. While the computational effort is feasible for a small number of particles, the exponential growth limits the approach quickly. However, highly optimized linear algebra routines and today's supercomputers allow extensive numerical simulations, continuously pushing state-of-the-art numerics. Exploiting the massive parallelization² with *matrix-free* (MF) applications allows handling Hilbert spaces of dimension $D \approx 4 \cdot 10^{12} \approx 2^{42}$. Depending on symmetries in the model, the complexity can be reduced, making calculations up to 50 spin-1/2 particles feasible [106, 107]. The number of particles can be further increased by constraining the Hilbert space by simply discarding states [108].

ED methods are divided into two types of linear algebra routines: methods that rely on the *sparsity* of the Hamiltonian and methods that do not! Exploiting the sparsity of the Hamiltonian allows fast matrix-vector multiplications. Based on Krylov spaces, these methods can tackle a small corner of the spectrum, like the ground state [109, 110], to evolve an initial state in time or to determine a typical thermal state at a finite temperature [111, 107]. They can be scaled up in large computing centers to multiple nodes using *Message Passing Interface* (MPI). In contrast, sparsity can not be exploited if the entire spectrum is desired. In that case, the full matrix has to be stored, and the required memory scales quadratically with the dimension. Highly optimized libraries like *BLAS* and *LAPACK* provide the necessary routines. Despite enormous computational resources that can be accessed nowadays, memory is the limiting barrier in most cases. Therefore, state-of-the-art MF computations that calculate matrix elements *on the fly* provide a powerful ansatz. The required memory³ to leading order for a Hilbert of dimension D for the MF solver and full ED is

$$\text{mem}_{\text{MF}} = \frac{2 \cdot 16 \cdot D}{1024^4} \text{TB} \text{ and } \text{mem}_{\text{FULL}} = \frac{3 \cdot 16 \cdot D^2}{1024^4} \text{TB}. \quad (1.26)$$

The significant advantages of these methods are their *exactness* and *applicability*. While MC methods are limited by the sign-problem and MPS methods develop biases towards weakly entangled states, ED does not face these subtleties. If a calculation is numerical feasible, it allows evaluating all physical quantities with machine precision. Exploiting symmetries is crucial for ED methods and is discussed in the following chapter, as it is heavily utilized in many parts of this thesis.

²The Cobra supercomputer at the *Max Planck Computing and Data Facility* allows an allocation of 620 nodes with 40 cores each providing an accessible memory of $\sim 109\text{TB}$.

³Spatial symmetries induce a complex-valued Hilbert space requiring 16 bytes to represent a scalar with double precision. The MF solver uses two vectors for input and output. *LAPACK* routines require three times the memory of the matrix.

Chapter 2

CONTROLLED METHODS ADVANCED IN THIS THESIS

Constructing analytical solutions for interacting many-body systems succeeds only in very few non-generic cases. Therefore, numerical approaches are necessary. None of the methods summarized in [Section 1.3](#) is the ultimate tool for studying frustrated magnets in three dimensions since each has its limitation: the sign problem, entanglement growth, and the cubic scaling in system size. Thus, this chapter focuses on algorithms tailored to study frustration in three dimensions. Each section provides methodological progress which allows for controlled and unbiased calculations as demonstrated in [Part II](#) and is one of the main contribution of this thesis.

The first section discusses the use of various symmetries in spin systems. An extensive number of symmetries is the key to solving interacting quantum systems analytically as they correspond to quantities that are conserved by the Hamiltonian. For example, the Kitaev honeycomb model [\[69\]](#) hosts plaquette operators that mutually commute. Their number is extensive and therefore allows for an analytic solution to the model. However, such models are rare. Nevertheless, even a subextensive number of conserved quantities simplifies the problems so that computations are possible in many cases. This reduction is crucial for methods based on ED as it makes larger system sizes accessible and is discussed in the first section. Most importantly, we introduce an automatic detection algorithm that maximizes the benefits of spatial symmetries. It exploits graph- and group-theoretical tools to determine all graph automorphisms for a finite cluster and to identify the largest commuting subgroup corresponding to the largest number of conserved quantities.

Numerical approaches are often restricted to clusters of finite size, making reliable predictions in three dimensions difficult when taking the cubic scaling in the linear system size into account. Cluster expansion methods that build up the lattice systematically do not face these finite-size effects as they produce the correct results in the thermodynamic limit – *if they are converged*. Their convergence is restricted by other parameters such as temperature. The second section introduces the numerical linked cluster expansion, which is in a spirit similar to a high-temperature expansion. Starting from pre-defined unit cells, it systematically includes larger clusters made up

of these units order by order. It provides unbiased thermodynamic data in the thermodynamic limit at finite temperatures and is well suited to study three-dimensional frustrated systems. In particular, combining the symmetries presented in the first section with the numerical linked cluster algorithm has proven valuable.

The third section introduces another cluster expansion based on the linked cluster theorem [112, 113]. It is a systematic approach to evaluate observables of wavefunctions evolved in imaginary time. While it provides an alternative way to determine finite-temperature properties in the thermodynamic limit, we apply the expansion to obtain a suitable dressing of low-energy product states to potentially describe the ground state of the pyrochlore Heisenberg antiferromagnet in Section 5.3. Note that both cluster expansions are fundamentally different even though the procedures seem similar.

2.1 Symmetries in spin systems

Symmetries and their consequences are pervasive in *all* areas of physics. We characterize different phases of matter according to its conserved – and broken – symmetries. One of the simplest examples in condensed matter is the transition from a disordered paramagnetic into a ferromagnetic phase in the classical n -vector model on a three-dimensional lattice. While the disordered paramagnetic phase preserves the continuous symmetry for $n \geq 2$, it spontaneously breaks the $O(n)$ -symmetry below the phase transition. Another example discussed in [Section 3.1](#) is spin liquids characterized by the symmetry of an emergent gauge theory describing their low-energy excitations. Symmetries in physics are described within the framework of group theory. However, this section presents a rather practical route focusing on spin systems to maximize the benefits of different symmetries and make larger system sizes accessible for ED methods.

A system is invariant under a certain symmetry operation if the associated operator Q commutes with the Hamiltonian:

$$[H, Q] = HQ - QH = 0 \quad (2.1)$$

The symmetry induces a conserved quantity [\[114\]](#), *e.g.* total momentum or total magnetization. [Equation 2.1](#) implies the conversation law for Q using Heisenberg’s equation of motion. Another important consequence of [Equation 2.1](#) is that the application of H to an eigenstate of Q does not change its eigenvalue q : $QH|q\rangle = HQ|q\rangle = qH|q\rangle$

Hence, representing the Hamiltonian in the eigenbasis of Q automatically generates a *block structure* where each block refers to an eigenvalue of Q – the conserved quantity. This is achieved by a unitary transformation in the eigenbasis of Q , which corresponds to a basis change in quantum mechanics. Following the same strategy, it is possible to exploit multiple symmetry operations Q_i for $i = 1, \dots, n$ simultaneously. The operators have to commute with the Hamiltonian and are required to commute amongst them.

$$[H, Q_i] = 0 \text{ and } [Q_i, Q_j] = 0 \quad \forall i, j \quad (2.2)$$

The symmetry operators can be applied successively to further reduce the block sizes such that each block corresponds to eigenvalues (q_1, \dots, q_n) associated with the respective symmetry operators Q_i . [Figure 2.1](#) illustrates this successive application of multiple symmetries. While the first blue block represents the full Hamiltonian matrix, the gray arrow represents a unitary transformation given by eigenstates of Q_1 , inducing a simplified red block structure. Instead of focusing on the dense matrix in blue, only the individual red blocks are treated independently. Further symmetries yield additional unitary transformations, which further reduce the block sizes are shown green and yellow. The figure uses realistic symmetries and dimensions, thereby visualizing the great benefits of symmetries as the block sizes shrink significantly.

The symmetries considered in this chapter are divided into two classes: symmetries acting

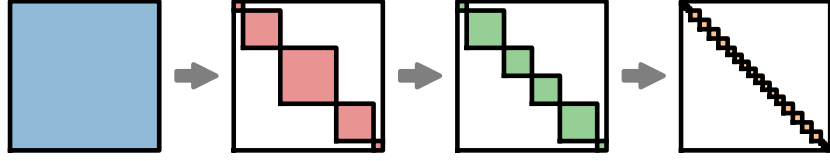


Figure 2.1: Utilization of different symmetries to block-diagonalize the Hamiltonian. The image illustrates the successive application of commuting symmetries for a system of spin-1/2 particles. Non-colored regions indicate zeros that are discarded in numerical simulations. The blue area refers to the dense 2^N -dimensional matrix; the red blocks exploited the total magnetization; the green blocks are obtained by applying the spin inversion symmetry for the largest blocks with $m_z = 0$ and spatial symmetries were applied in the last step to achieve the yellow block structure.

globally on the spin space and spatial symmetries depending on the underlying lattice. We discuss different spin symmetries like total magnetization, spin inversion, or $SU(2)$. Lastly, we introduce an automatic detection algorithm maximizing the number of mutually commuting spatial transformations for arbitrary geometries developed within this thesis. Some models, like the Kitaev honeycomb model, require symmetries composed of spatial transformations and rotations in spin space.

In principle, all symmetries discussed in this section commute and could be utilized simultaneously (when allowed by the Hamiltonian). However, combining spatial symmetries with the $SU(2)$ -symmetry of the isotropic XXX -Hamiltonian is theoretically possible but not very useful practice for two reasons. First, it is not apparent how to simultaneously diagonalize both symmetry operators to generate the required block structure. When both are diagonalized independently, the Gram-Schmidt process or other methods like QR or LU decomposition can be applied to remove redundant states in the combined basis. However, as attempted in this thesis, this procedure exceeds the computational complexity of directly diagonalizing the Hamiltonian in one basis. Second, the obtained basis is not sparse and, therefore, not suited for Krylov space and MF methods. In contrast, combining the total magnetization, spin inversion, and spatial symmetries serves as a powerful ansatz for XXZ -Hamiltonians. Most importantly, the symmetrized basis preserves the sparsity of Hamiltonian, making it appealing for MF methods. Figure 2.2a compares the reduction of various symmetries for spin-1/2 system.

Besides implementing the efficient usage of symmetries, it is essential to know the computational architecture and identify bottlenecks of the applied algorithm. There are powerful libraries for full diagonalization and sparse linear algebra operations like *PETSc* and *SLEPc* [115, 116, 117, 118] for distributed memory machines. However, MF applications exploiting various symmetries [106] are not publicly available and must be coded from scratch. Figure 2.2b shows the lowest eigenenergies for a system with $N = 42$ spin-1/2 sites using a MF solver by combining the total magnetization, spin inversion (for zero-magnetization sector), and the spatial symmetries.

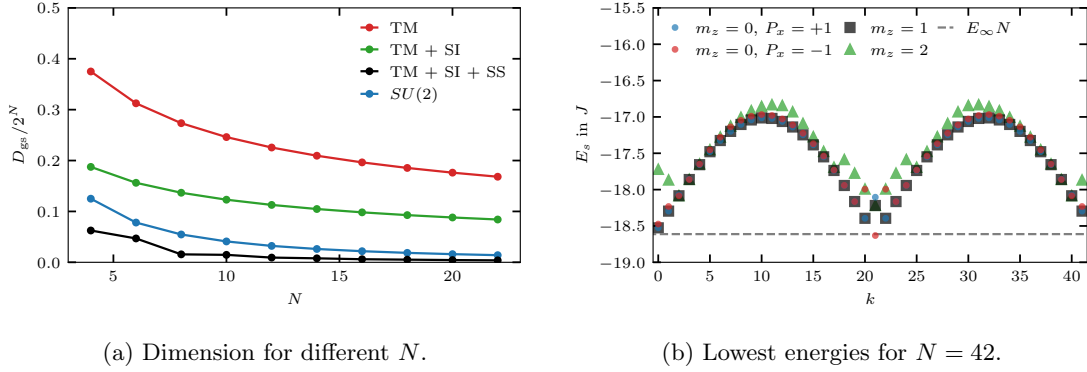


Figure 2.2: (a) The maximal block sizes of the ground-state sector for antiferromagnetic couplings on a chain with periodic boundary conditions divided by the full Hilbert space dimension 2^N for $S = 1/2$. The following symmetries are used: $SU(2)$, total magnetization (TM), spin inversion (SI), and spatial symmetry (SS). (b) Lowest energy E_s in different symmetry sectors for an antiferromagnetic chain with periodic boundary conditions with a coupling strength J , $N = 42$, and $S = 1/2$ using a MF solver. The x -axis refers to the discrete conserved momenta. Total magnetization, spin inversion (if possible), and the total momentum $\exp(2\pi i k/N)$ are utilized. $E_\infty = 1/4 - \ln(2)$ is the ground-state energy per site in the thermodynamic limit.

Defining symmetry operations requires establishing a mathematical framework and introducing the computational basis \mathcal{S}^S . It is a complete and orthogonal basis of the exponentially large Hilbert space. Analogously to Equation 1.16, the basis states are simple product states. In the case of spin-1/2, the state of an individual site is a superposition of $|\uparrow\rangle$ and $|\downarrow\rangle$. Therefore, the basis states of N spin-1/2 are:

$$\mathcal{S}^{1/2} = \left\{ \bigotimes_{|\Psi_i\rangle \in \{|\uparrow\rangle, |\downarrow\rangle\}} |\Psi_1\rangle \otimes \cdots \otimes |\Psi_N\rangle = |\Psi_1 \dots \Psi_N\rangle \right\} \quad (2.3)$$

The computational basis is easily extended to higher spin models by introducing more degrees of freedom per site. The full Hilbert space dimension is $|\mathcal{S}^S| = (2S+1)^N$. Similarly, the notation can be adapted to fermions where for example, $|\uparrow\rangle$ refers to the occupation of a specific orbital.

2.1.1 Total magnetization

The total magnetization is conserved for the XXZ - and XXX -Hamiltonian introduced in Equation 1.20 and Equation 1.21. As we are interested in spin systems, we refer to the total magnetization. However, the concept is equivalent to the conservation of particle numbers in the Hubbard model. For simplicity, we refer to the magnetization along the z -axis in spin-space:

$$m_z = \sum_i S_i^z. \quad (2.4)$$

The conservation follows immediately by replacing $S_i^x S_j^x + S_i^y S_j^y = \frac{1}{2} (S_i^+ S_j^- + S_i^- S_j^+)$ but can also be obtained by evaluating the commutation relations using [Equation 1.7](#).

The implementation is straightforward as the unitary transformation generating the block structure is a simple basis permutation since the computational basis are eigenstates of m_z . It naturally arises from aligning all states from \mathcal{S}^s according to their total magnetization m_z . From a numerical point of view, it is simpler to label different blocks according to the number of up-spins n_{up} than m_z . For arbitrary spin models, n_{up} is an integer in $\{0, \dots, 2Ns\}$. Fully polarized states corresponds to $n_{\text{up}} = 0$ and $n_{\text{up}} = 2Ns$. The total magnetization for a given n_{up} configuration is $m_z = n_{\text{up}} - Ns$. The block sizes are obtained directly from combinatorial arguments and reduces to the binomial coefficient

$$\mathcal{C}(N, n_{\text{up}}) = \binom{N}{n_{\text{up}}} = \frac{N!}{n_{\text{up}}!(N - n_{\text{up}})!} \quad (2.5)$$

for $S = 1/2$. The first reduction in [Figure 2.1](#) is obtained by the total magnetization for $N = 4$ spin-1/2 sites. Each red block corresponds to an eigenvalue of $m_z = -2, \dots, 2$ or $n_{\text{up}} = 0, \dots, 4$. Determining the dimensions of individual blocks for higher spin S is more evolved than the simple binomial coefficient. [Alg. 1](#) determines the dimension for a given S , N , and n_{up} .

State-of-the-art MF solvers often access the basis states without saving them explicitly. Hence, highly optimized code requires an efficient mapping between the physical states within a total-magnetization sector

$$\mathcal{S}_{n_{\text{up}}}^S = \left\{ |\Psi\rangle = \bigotimes_{|\Psi_i\rangle \in \{|\uparrow\rangle, |\downarrow\rangle\}} |\Psi_i\rangle \otimes \dots \otimes |\Psi_N\rangle \mid \text{s. t. } m_z|\Psi\rangle = n_{\text{up}} - 2SN \right\} \subset \mathcal{S}^S \quad (2.6)$$

and their indices $\{1, \dots, D\}$ with $D = |\mathcal{S}_{n_{\text{up}}}^S|$. Simply storing an exponentially large dictionary mapping the states to their indices requires a large amount of memory. While the additional cost is negligible for full ED calculations (as the memory scales with D^2), this will become a bottleneck for sparse applications on distributed memory machines. Lin tables [\[119\]](#) provide an *efficient* way to quickly map states and their indices and vice versa with a reduced memory cost. Based on two lookup tables, the algorithm splits the system into two subsystems, reducing the required memory from $\mathcal{O}(2^N)$ to $\mathcal{O}(2 \cdot 2^{N/2})$. Optimized ED methods can currently handle up to $N \sim 48$ spin-1/2 sites [\[107\]](#) using up to $\sim 20\,000$ MPI processes. While a naive dictionary requires $\sim 5 \cdot 10^5$ GB per MPI process (what is impossible), Lin's original proposal reduces the memory cost to approximately ~ 0.25 GB per MPI process. Scaling the reduced memory by the number of processes requires ~ 5 TB, which is not very practical. Therefore, we generalized the approach by Hai-Qing Lin by introducing multiple subsystems such that the memory consumption and run time is reduced for larger system. For example, splitting up the system using three tables demands only ~ 1 MB, which can be efficiently stored for each process.

Algorithm 1: Determining the dimension of a total-magnetization sector for a system for a given N , S , and n_{up} .

Data: $1 < N$ and $0 \leq n_{\text{up}} \leq 2sN$

Function `get_dimension`(N, n_{up}, S):

```

    dim = 0
    if  $S == 1/2$  then
        return  $\mathcal{C}(N, n_{\text{up}})$ 
    else
        for  $i = 0; i < n_{\text{up}} // (2S) + 1; i++$  do
            // ‘//’ refers to the integer division
            if  $N == i$  then
                dim = dim + 1
            else if  $(N - i) \cdot (2S - 1) + 2Si \geq n_{\text{up}}$  then
                dim = dim +  $\mathcal{C}(N, i) \cdot \text{get\_dimension}(N - i, n_{\text{up}} - 2Si, S - 1/2)$ 
            end
        end
    end
    return dim

```

2.1.2 Spin inversion

The spin inversion inverts the spin state by mapping up- to down-spins and vice versa in the $S = 1/2$ case. Alternatively, it can be interpreted as a mapping between particles and holes in the fermionic case. The reduction from red to green in [Figure 2.1](#) is due to spin inversion. Obtaining the symmetrized basis in this case is more evolved than a simple permutation as above but still somewhat simple. The associated operator is

$$P_x = \prod_j S_j^x, \quad (2.7)$$

which acts on each site. Note that the operator is defined as a product, whereas [Equation 2.4](#) uses a sum. Applying P_x to a state in computational basis with m_z maps it to $-m_z$, thereby destroying the block structure for $m_z \neq 0$. It is conserved for the XXZ - and XXX -Hamiltonian in the $m_z = 0$ sector and commutes with the total magnetization in that case: $[P_x, m_z] = 2m_z P_x$. Note that the $m_z = 0$ sector does not exist for odd system sizes N and half integer spin S . The zero-magnetization sector is the largest and of particular interest as it contains the ground state for the Hamiltonians discussed in this thesis.

Squaring the inversion operator generates the identity yielding two possible eigenvalues ± 1 for P_x . The zero-magnetization sector is block diagonal in the eigenbasis of P_x where both blocks correspond to its two eigenvalues. The symmetrized basis is generated by *representative* states \mathcal{R} such that the full zero-magnetization sector ($n_{\text{up}} = NS$) has to be covered

$$\mathcal{S}_{n_{\text{up}}=NS}^S = (\mathcal{R} \cup P_x \mathcal{R}) \text{ with } (\mathcal{R} \cap P_x \mathcal{R}) = \emptyset. \quad (2.8)$$

Determining \mathcal{R} is particularly simple in this case. $|r\rangle \in \mathcal{S}_{n_{\text{up}}=NS}^S$ is added to \mathcal{R} if and only if the integer representation of $|r\rangle$ is smaller than $P_x|r\rangle$. The representative set is not uniquely defined. Each representative state $|r\rangle \in \mathcal{R}$ generates two eigenstates with eigenvalues $+1$ and -1 :

$$P_x = \pm 1 : \quad |r_{\pm}\rangle = (|r\rangle \pm P_x|r\rangle) / \sqrt{2} \quad (2.9)$$

Evaluating the Hamiltonian in the eigenbasis given by $\langle r_{\pm} | H_{XXX} | r_{\pm} \rangle$ yields the desired block structure where the zero-magnetization sector splits into blocks associated with the eigenvalues $(m_z = 0; P_x = \pm 1)$. Both have an equal dimension such that the dimension of the ground-state sector is halved. Hence, the maximal block size of the Hamiltonian is found in $m_z = \pm 1$ sector.

Even though spin inversion symmetry does not reduce the block sizes for other sectors, it projects m_z to $-m_z$. This equivalence induces the equality of the blocks in the Hamiltonian associated with H_{m_z} and H_{-m_z} . Therefore, numerical simulations can be restricted to $m_z \leq 0$.

2.1.3 SU(2)

The XXX-Hamiltonian in Equation 1.21 is invariant under the $SU(2)$ algebra. Rather than presenting a detailed discussion [120, 121] including the irreducible representations, Lie groups, and characters, this section focuses on the practical application to spin systems. It presents a general way to construct $SU(2)$ -symmetric states such that the Hamiltonian naturally exhibits the desired block structure. The rest of this subsection is divided into three parts. We (i) introduce $SU(2)$ -symmetric states, (ii) describe the decomposition of a tensor product space into two irreducible spin representations, and (iii) apply the procedure successively to generate symmetric states for N individual spins.

(i) The representation space of a state with a *total spin* S contains $2S + 1$ states labeled by $m_z = -S, \dots, S$: $|S; m_z\rangle$. The states are normalized and orthogonal $\langle S; m'_z | S; m_z \rangle = \delta_{m'_z m_z}$. A spin state with $S = 0, 1/2, 1, 2$ is named a *singlet*, *doublet*, *triplet* and *quintuplet*, referring to the dimension of representation space. The corresponding algebra acting on the space is given by the familiar operators $S^{\pm} = S^x \pm iS^y$ and S^z :

$$S^z |S; m_z\rangle = m_z |S; m_z\rangle \text{ and } S^{\pm} |S; m_z\rangle = \sqrt{(S \pm m_z + 1)(S \mp m_z)} |S; m_z \pm 1\rangle \quad (2.10)$$

It follows from Equation 2.10 that $S^+ |S; S\rangle = 0$ and $S^- |S; -S\rangle = 0$. The maximal set of commuting operators is obtained by combining the *Casimir* operator, $S^2 = \mathbf{S} \cdot \mathbf{S} = S^x^2 + S^y^2 + S^z^2$, with one of the individual spin operators $\alpha = x, y, z$: $[S^2, S^{\alpha}] = 0$. Without loss of generality, we set $\alpha = z$ such that the operator is identified as the magnetization similar to the last part. The Casimir operator is associated with the total spin as it yields

$$S^2 |S; m_z\rangle = S(S + 1) |S; m_z\rangle \text{ and } S^z |S; m_z\rangle = m_z |S; m_z\rangle, \quad (2.11)$$

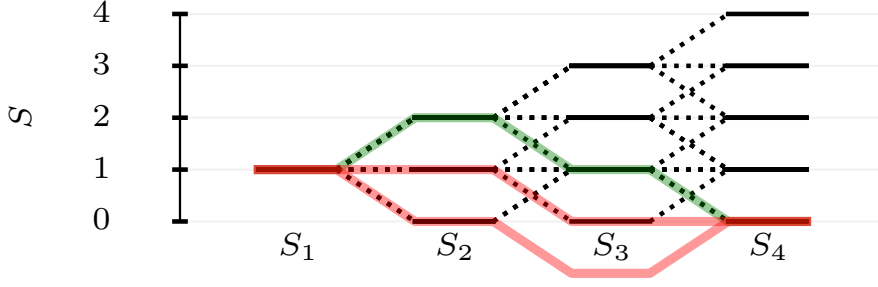


Figure 2.3: Possible paths to generate $SU(2)$ -symmetric states for $N = 4$ and $S = 1$. The solid lines represent the possible spin plateaus S_n , and the dashed lines show the allowed transitions from a spin plateau S_n to S_{n+1} by adding another spin. While the green line fulfills the constraint in Equation 2.15, the red lines violate the rule and do not represent a possible path to generate a singlet state with $S_4 = 0$.

Similar to the case of a single spin, the same descriptions applies to multiple spins. Their tensor product space can be decomposed into irreducible representations characterized by total spin S and magnetization m_z referring to the full system. They are eigenstates of the Casimir operator and the total-magnetization operator [Equation 2.4]:

$$S^2 = \left(\sum_i \mathbf{S}_i \right)^2 \quad \text{and} \quad m_z = \sum_i S_i^z \quad (2.12)$$

The raising and lowering operators are defined analogously for multiple spins.

The isotropic XXX -Hamiltonian commutes with both operators, thereby conserving not only the total magnetization but also the total spin. Therefore, it is possible to diagonalize them simultaneously and find sets of eigenvectors corresponding to the eigenvalues $(S; m_z)$, which block-diagonalize the Hamiltonian. However, constructing $SU(2)$ -symmetric states is more involved than the previously discussed symmetries.

(ii) Decomposing a tensor product space of two irreducible representation spaces \mathcal{H}_{AB} into the direct sum of irreducible representation space relies on Clebsch-Gordan coefficients (CGCs) [122]. The two irreducible spin spaces exhibit a total spin of S_A and S_B such that their tensor product space

$$\mathcal{H}_{AB} = \{ |S_A; m_A\rangle \otimes |S_B; m_B\rangle \mid m_A = -S_A, \dots, S_A \text{ and } m_B = -S_B, \dots, S_B \} \quad (2.13)$$

has dimension $D = (2S_A + 1)(2S_B + 1)$. CGCs allow its decomposition into irreducible representation spaces with the total spin $S_C = |S_A - S_B|, \dots, S_A + S_B$. A representation space with a total spin S_C exhibits $2S_C + 1$ states such that $D = \sum_{k=|S_A-S_B|}^{S_A+S_B} (2k + 1)$.

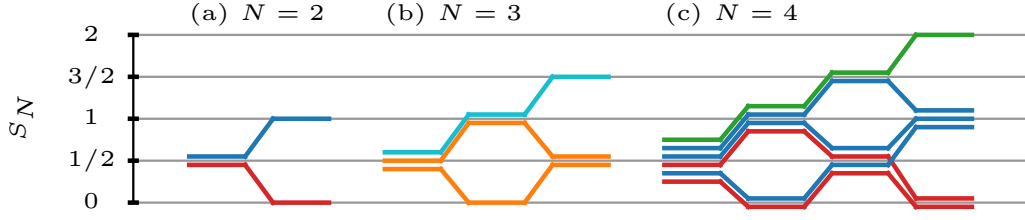


Figure 2.4: Different paths to generate $SU(2)$ -symmetric states for a system with $N = 2, 3, 4$ and $S = 1/2$ in panels (a), (b), and (c). Each path represents a possible spin state with total spin S_N , which is color resolved. Each state/path exhibits $2S_N + 1$ states: $|S_N; -S\rangle, \dots, |S_N; S\rangle$.

CGCs, $C_{(S_A; m_A), (S_B; m_B)}^{S_C; m_C}$, are used to construct the basis states $|S_C; m_C\rangle$ from the product states defined Equation 2.13. They depend on the six parameters, are real, follow selection rules¹, and ensure the normalization and orthogonality of the newly generated states. More details and their efficient derivation can be found in Ref. [122, 121]. A specific state $|S_C; m_C\rangle$ is generated from the initial states $|S_A; m_A\rangle$ and $|S_B; m_B\rangle$ in the following way:

$$|S_C; m_C\rangle = \sum_{m_A=-S_A}^{S_A} \sum_{m_B=-S_B}^{S_B} C_{(S_A; m_A), (S_B; m_B)}^{S_C; m_C} |S_A; m_A\rangle \otimes |S_B; m_B\rangle \quad (2.14)$$

(iii) This paragraph describes how symmetrized basis states $|\Psi_i^{(S_N; m)}\rangle$, $i = 1, \dots, D$, for a given total spin S_N and magnetization m_z are obtained in a system of N individual spin- S . The construction of a specific state for multiple spin- S is done successively by adding the n th spin to the irreducible representation containing the previous $n - 1$ spins. This diagrammatic approach is illustrated in Figure 2.3.

The basic recipe is as follows: Starting from the first spin state, the second spin is added, and their tensor product space is reduced following Equation 2.14. The irreducible representations describing the first two spins are merged with the third, and their tensor product space is again reduced. This procedure will be carried on to merge all spins successively. Merging n individual spin- S allows only certain total spin plateaus labeled by S_n . The spin plateaus generate a diagram illustrating permitted transitions from S_n to S_{n+1} . A transition from a plateau S_n to

¹ $C_{(S_A; m_A), (S_B; m_B)}^{S_C; m_C}$ is only non-zero if

$m_C = m_A + m_B$, $|S_A - S_B| \leq S_C \leq S_A + S_B$ and $S_A + S_B + S_C \in \mathbb{N}_0$

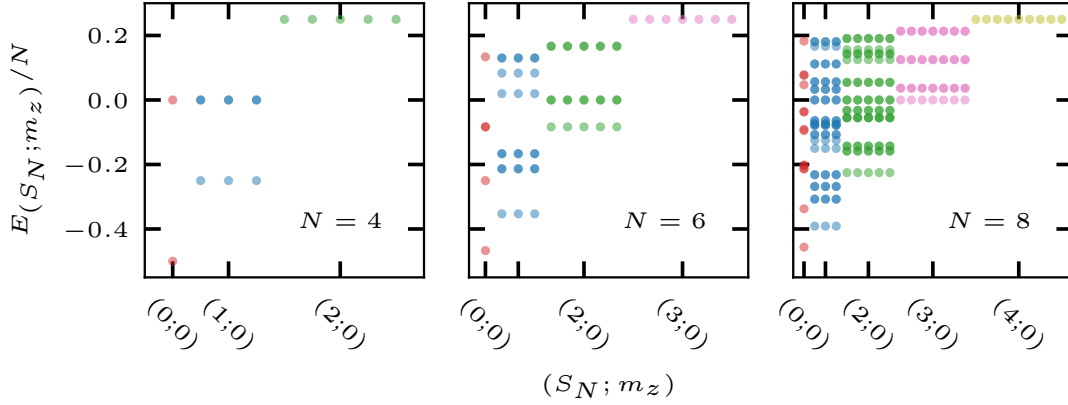


Figure 2.5: Eigenvalues of the isotropic Heisenberg Hamiltonian H_{XXX} ($J = 1$) from Equation 1.21 organized by $SU(2)$ quantum numbers $(S_N; m_z)$ for a periodic chain with $N = 4, 6, 8$ and $S = 1/2$. The transparency reflects the degeneracies.

the next plateau S_{n+1} by adding another spin- S has to fulfill the following constraint:

$$S_{n+1} \in \{|S_n - s|, \dots, S_n + s\} \quad (2.15)$$

Figure 2.3 shows all possible paths for a system with $N = 4$ spin-1 states. The first plateau corresponds to the first spin $S_1 = 1$. Following Equation 2.14, combining it with the second generates irreducible representations with $S_2 = 0, 1, 2$. The next spin-1 is merged with all possible three spin states of S_2 , and the allowed paths are indicated by transitions to $S_3 = 0, 1, 2, 3$. Finally, the last spin has five possible irreducible representations: $S_N = S_4 = 0, 1, 2, 3, 4$.

Different paths start from S_1 and terminate at some S_N of interest, traversing different S_n on the way. Each path i consistent with the constrain in Equation 2.15 corresponds to a state in the symmetrized basis $|\Psi_i^{(S_N; m)}\rangle$. Hence, there are exponentially many ways to generate different states for a specific S_N . The $SU(2)$ -eigenbasis generating a specific block $(S_N; m_z)$ in the Hamiltonian is obtained by finding all valid paths. Figure 2.4 shows all possible paths for $N = 2, 3, 4$ and $S = 1/2$. Panel (a) reveals one singlet state in red and one triplet state in blue for $N = 2$. Four spins, panel (c), generate two different singlet states corresponding to the red paths. Therefore, the subspace for $S_4 = 0$ and $m_z = 0$ is spanned by $|\Psi_0^{(0;0)}\rangle$ and $|\Psi_1^{(0;0)}\rangle$. Additionally, the three triplet paths in blue form three subspaces of dimension three spanned by $|\Psi_0^{(1; m_z)}\rangle$, $|\Psi_1^{(1; m_z)}\rangle$ and $|\Psi_2^{(1; m_z)}\rangle$ for $m_z = -1, 0, 1$. Finally, the quintuplet path in green exhibits five individual blocks of size one corresponding to $|\Psi_0^{(2; m_z)}\rangle$ for $m_z = -2, -1, 0, 1, 2$.

The symmetrized basis has many useful properties. First, CGCs ensure the orthogonality and normalization of the basis states for different paths. Second, the isotropic Hamiltonian converses

S_N and m_z by construction such that it is block diagonal:

$$\langle \Psi_i^{(S'_N; m'_z)} | \Psi_j^{(S_N; m_z)} \rangle = \delta_{ij} \delta_{S'_N S_N} \delta_{m'_z m_z} \quad (2.16)$$

$$\langle \Psi_i^{(S'_N; m'_z)} | H_{XXX} | \Psi_j^{(S_N; m_z)} \rangle = 0 \text{ for } S'_N \neq S_N \text{ and } m'_z \neq m_z \quad (2.17)$$

Third, the eigenvalues for all magnetization subspaces, $m_z = -S_N, \dots, S_N$, for a fixed total spin S_N are identical. The eigenvalues for systems with $N = 4, 6, 8$ spin-1/2 sites on a chain with periodic boundary conditions are shown in [Figure 2.5](#). Lastly, the full magnetization subspace, $m_z = -S_N, \dots, S_N$, of a particular state $|\Psi_i^{(S_N; m_z)}\rangle$ can be generated by the lowering and raising operators.

The general procedure to derive the basis and the Hamiltonian is summarized by four steps:

- (a) Generate the diagram with allowed transition from S_n to S_{n+1} .
- (b) Find all valid paths connecting S_1 with the S_N of interest.
- (c) Determine the basis states $|\Psi_i^{(S_N; m_z)}\rangle$ according to [Equation 2.14](#) along each path i .
- (d) Derive the specific block of the Hamiltonian the by $H_{ij}^{(S_N; m_z)} = \langle \Psi_i^{(S_N; m_z)} | H_{XXX} | \Psi_j^{(S_N; m_z)} \rangle$

Exploiting the $SU(2)$ -symmetry reduces the maximal dimension of the blocks compared to the total magnetization alone. The maximal block dimension depends on the spin- S and number of sites. However, generating the basis states and the Hamiltonian is expensive, so the benefits are limited. Also, it is only applicable to the fully isotropic Hamiltonian. The main disadvantage is the loss of sparsity. While the Hamiltonian is sparse when represented in the computational basis states, it is dense in the $SU(2)$ -symmetrized basis. The dense structure is inherited from the basis states, which are a massive superposition of states in the computational basis. Therefore, exploiting $SU(2)$ -symmetry is only practical for full diagonalization where the complete Hamiltonian is stored.

2.1.4 Spatial symmetries

Whereas previously discussed symmetries act globally on the whole spin space, spatial symmetries take the actual lattice structure into account. Translational invariance is an essential concept in physics. For example, single-particle eigenstates are labeled by their momentum, thereby defining the first Brillouin zone. In interacting many-body systems, spatial symmetries provide a powerful tool to reduce the complexity as it block-diagonalizes the Hamiltonian, which conserves the total “many-body” momentum. While the allowed momenta in the thermodynamic limit become continuous, numerical simulations handling a finite number of sites are restricted to a discrete set of momenta. This section describes an automatic algorithm to identify, optimize, and apply spatial symmetries in spin systems. The approach extends beyond usually applied spatial symmetries like translations, rotations, or reflections and by using abstract automorphisms, which

have proven extremely valuable in the case of the pyrochlore lattice. The ideas were developed within this thesis.

A finite lattice is described by a graph. The simplest form of the graph includes (uniform) nodes and edges. We identify the spins in the lattice with its nodes; the nearest-neighbor exchange terms are its edges. More generally, nodes and edges can exhibit a specific color or direction. For example, different bonds in the Kitaev model or weaker next-nearest-neighbor interactions are described by an edge color. Different node colors can be induced by a non-uniform magnetic field which is the case for the dipolar-octupolar pyrochlores, *cf.* [Section 3.3](#).

The spatial symmetries of a Hamiltonian are graph automorphisms. An automorphism is a (bijective) permutation of nodes and an element of the symmetric group S_N for N sites. Given a set of nodes $\mathcal{N} = \{1, \dots, N\}$ and edges \mathcal{E} , $\sigma \in S_N$ is an automorphism if it conserves the edges and thereby leaving the Hamiltonian invariant:

$$\{i, j\} \in \mathcal{E} \quad \Rightarrow \quad \{\sigma(i), \sigma(j)\} \in \mathcal{E} \quad \text{for } i, j \in \mathcal{N} \quad (2.18)$$

If the graph additionally exhibits different color attributes, these have to be fulfilled as well. That means the color of node i has to be identical to the color of $\sigma(i)$, and the edge color of $\{i, j\}$ has to be identical to the edge color of $\{\sigma(i), \sigma(j)\}$. The automorphism implies the commutation between the operator P_σ associated with the permutation and the Hamiltonian. Therefore, diagonalizing the operator induces the block structure in the Hamiltonian labeled by its eigenvalues – the discrete momenta. The action of a permutation σ to the computational basis is as follows:

$$P_\sigma |\alpha_1, \alpha_2, \dots, \alpha_N\rangle = |\alpha_{\sigma(1)}, \alpha_{\sigma(2)}, \dots, \alpha_{\sigma(N)}\rangle \quad \text{with } \alpha_i \in \{-S, \dots, S\} \quad (2.19)$$

The matrix representation P_σ associated with the permutation σ is orthogonal, $P_\sigma^T P_\sigma = \mathbb{1}$, and idempotent with $n_\sigma < N$: $P_\sigma^{n_\sigma} = \mathbb{1}$. The orthogonality of P_σ induces $\langle \Psi | P_\sigma^T = \langle \Psi | P_\sigma^{-1} = \langle \Psi | P_{\sigma^{-1}}$, where $\sigma^{-1} \in S_N$ is the inverse permutation of σ . Similar to the total momentum in a periodic chain with length N , a single permutation induces n_σ blocks with eigenvalues $e^{2\pi i k / n_\sigma}$ for $k = 0, \dots, n_\sigma - 1$, which follows from $P_\sigma^{n_\sigma} = \mathbb{1}$.

In general, the underlying graph exhibits a vast number of independent automorphisms. Two automorphisms σ and η are said to be independent if $\eta \neq \sigma^k$ for any k , *e.g.* translations along different axes, x and y . Applying multiple automorphisms and deriving the symmetrized basis takes several steps: (i) we need to identify all automorphisms, (ii) find the largest commuting subgroup, (iii) determine a set of generators, and (iv) generate the basis to calculate the Hamiltonian.

- (i) First, the group of all automorphism \mathcal{A} has to be determined, which can be done using highly optimized graph tools like *Nauty & Traces* [123]. Typically, the automorphisms do *not commute* among themselves!

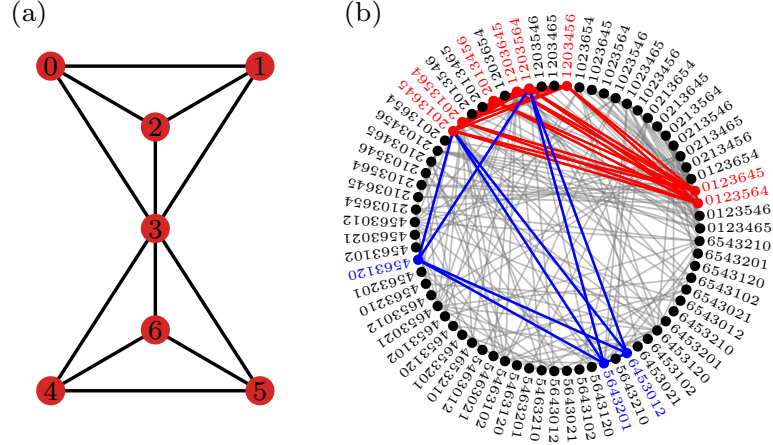


Figure 2.6: Illustration of the maximal commuting subgroup $\mathcal{C} \subseteq \mathcal{A}$, (ii). The sample graph, two coupled tetrahedra with a single node and edge color, is shown in panel (a). All 71 non-trivial (excluding the identity for the sake of visibility) automorphisms, \mathcal{A} , of the graph are shown as nodes in panel (b). Each automorphism corresponds to a permutation of nodes in (a), leaving the graph invariant. Two automorphisms in panel (b) exhibit an edge if they commute. The largest (red) and second largest (blue) commuting (fully connected) subgroups are highlighted in panel (b). The choice is not unique.

(ii) Second, it is necessary to identify the largest commuting (abelian) subgroup $\mathcal{C} \subseteq \mathcal{A}$ of the automorphism group \mathcal{A} to maximize the number of blocks. However, finding the largest commuting subgroup is a challenging problem in itself. Luckily, we can exploit another tool from graph theory to solve this problem: *clique maximization* [124]. We identify the group of all automorphisms as a second graph. Each automorphism $\sigma, \eta \in \mathcal{A}$ corresponds to a node, and we draw an edge between them if they commute $\sigma\eta = \eta\sigma$. Then, the clique maximization algorithm determines the largest fully connected (abelian) subgroup \mathcal{C} such that all elements commute amongst themselves and with the Hamiltonian. Each automorphism of the subgroup can be identified with a block in the Hamiltonian, reducing the complexity. The block sizes typically vary depending on a set of generators and the elements of \mathcal{C} . The largest clique is not uniquely defined, and it happens (in some rare cases) that smaller subgroups generate a smaller maximal block size. The procedure is illustrated in Figure 2.6.

(iii) Third, it is necessary to determine a *minimal* set of generators $\mathcal{U} = \{u_1, \dots, u_U\} \subseteq \mathcal{C}$ covering the complete commuting subgroup of automorphisms \mathcal{C} . For each element in

Algorithm 2: Determining generators for a commuting subgroup of automorphisms \mathcal{C} .

Data: List of commuting automorphisms \mathcal{C}

 Determine the order $O[\sigma]$ of each automorphism $\sigma \in \mathcal{C}$ such that $O[\sigma] = n_\sigma$ with $\sigma^{n_\sigma} = \mathbb{1}$

 Initialize empty lists of permutations: $\mathcal{U}, \mathcal{D} = []$

 Add the identity to \mathcal{D} : $\mathcal{D}.\text{append}(\mathbb{1})$
while $\max[O] > 0$ **do**

 Find permutation u with maximal order L_u in O // not uniquely defined

 Add u to \mathcal{U} : $\mathcal{U}.\text{append}(u)$

 Create a copy of \mathcal{D} : $\mathcal{D}' = \mathcal{D}$

 for k in $[1, \dots, L - 1]$ **do**

 for η in \mathcal{D}' **do**

 $\pi = \eta u^k$

 Add π to \mathcal{D} : $\mathcal{D}.\text{append}(\pi)$

 Set $O[\pi] = 0$

 end

 end
end
return \mathcal{U}
// set of generators

$\sigma \in \mathcal{C}$, there must be a unique multiindex $n_\sigma = (n_1, \dots, n_U) \in \mathbb{N}^U$ with $|\mathcal{U}| = U$ such that

$$\sigma = \prod_{i=1}^U u_i^{n_i} \quad \text{for } u_i \in \mathcal{U}, \quad (2.20)$$

where each n_i refers to one generator (symmetry). The product of permutations refers to their composition. The ordering is arbitrary since all elements of \mathcal{U} commute. Each generator u_i exhibits a maximal order $L_i \leq N$ such that $u_i^{L_i} = \mathbb{1}$. Therefore, the multiindex (n_1, \dots, n_U) is restricted by $0 \leq n_i < L_i$. Each symmetrized eigenbasis defining the individual blocks of the Hamiltonian corresponds to one multiindex, which defines the phases of permuted states (similar to momentum along different axes). The number of blocks is $|\mathcal{C}| = \prod_i L_i$. Referring to the example in Figure 2.6: the largest subgroup includes nine (the identity was omitted for the sake of clarity) automorphisms, and the minimal set of independent generators are the two C_3 permutations of the outer surfaces.

Finding the set of generators is not as demanding as steps (i) and (ii) and is computationally cheap. The procedure is summarized in Alg. 2.

- (iv) Lastly, we can generate the symmetrized basis associated with the commuting generators derived in (iii). Each permutation $\sigma \in \mathcal{C}$ exhibits a unique multiindex (n_1, \dots, n_U) . This multiindex defines the momenta, which labels an invariant block of the Hamiltonian. Similar to the spin inversion, the basis is obtained by a *minimal* representative subset of the computational basis, $\mathcal{R} \subseteq \mathcal{S}_{n_{\text{up}}}^S$. We directly exploit the total magnetization, but the procedure can be applied analogously without it, as demonstrated in Section 4.3. Applying all permutations $\sigma \in \mathcal{C}$ to \mathcal{R} has to cover $\mathcal{S}_{n_{\text{up}}}^S$. The representative subset is generated

by iterating over $|\Psi\rangle \in \mathcal{S}_{n_{\text{up}}}^S$, which is added to \mathcal{R} if and only if it has the lowest integer representation compared to $\{P_\sigma|\Psi\rangle \mid \sigma \in \mathcal{C}\}$.

Each state in \mathcal{R} represents a *possible* state in the symmetrized basis – its existence depends on the applied momenta and automorphisms. Therefore, the maximal block size can be at most of dimension $|\mathcal{R}|$ which is true for $n_B = (0, \dots, 0)$. The possible basis state for $|r\rangle \in \mathcal{R}$ for a specific multiindex $n_B = (n_1, \dots, n_U)$ has the following form:

$$|r_{n_B}\rangle = \frac{1}{\sqrt{N_{r,n_B}}} \sum_{\sigma \in \mathcal{C}} e^{2\pi i \sum_{i=1}^U n_B(i) n_\sigma(i) / L_i} P_\sigma |r\rangle \quad (2.21)$$

$$= \frac{1}{\sqrt{N_{r,n_B}}} \sum_{\sigma \in \mathcal{C}} \prod_{i=1}^U e^{2\pi i n_B(i) n_\sigma(i) / L_i} P_{u_i}^{n_\sigma(i)} |r\rangle \quad (2.22)$$

Here, N_{r,n_B} is the normalization constant and depends on the specific state and the applied permutations. Notably, the phase factors can be destructive and annihilate a representative state in a particular symmetry sector n_B . Therefore, the block sizes typically vary and can be smaller than $|\mathcal{R}|$. The simplest example is a fully polarized state $|r\rangle = |\uparrow, \dots, \uparrow\rangle$ with is only present in the $n_B = (0, \dots, 0)$. The eigenvalue referring to a generator $u_i \in \mathcal{U}$ is

$$P_{u_i} |r_{n_B}\rangle = e^{2\pi i n_B(i) / L_i} |r_{n_B}\rangle. \quad (2.23)$$

The phase factors and N_{r,n_B} ensure the orthogonality and the normalization of the basis states:

$$\langle r'_{n'_B} | r_{n_B} \rangle = \delta_{rr'} \delta_{n_B n'_B} \quad (2.24)$$

The basis states define the unitary transformation yielding the desired block structure. For a specific sector n_B , the matrix elements are constructed by the symmetrized (and non-vanishing) representative states:

$$H_{r'r}^{n_B} = \langle r'_{n_B} | H | r_{n_B} \rangle \quad (2.25)$$

$$= \frac{1}{\sqrt{N_{r',n_B}} \sqrt{N_{r,n_B}}} \sum_{\sigma, \sigma' \in \mathcal{C}} e^{2\pi i \sum_{i=1}^U n_B(i) (n_\sigma(i) - n_{\sigma'}(i)) / L_i} \langle r' | P_{\sigma'}^T H P_\sigma | r \rangle \quad (2.26)$$

$$= \frac{1}{\sqrt{N_{r',n_B}} \sqrt{N_{r,n_B}}} \sum_{\sigma, \sigma' \in \mathcal{C}} e^{2\pi i \sum_{i=1}^U n_B(i) (n_\sigma(i) - n_{\sigma'}(i)) / L_i} \langle r' | P_{\sigma'}^{-1} P_\sigma H | r \rangle \quad (2.27)$$

$$= \frac{1}{\sqrt{N_{r',n_B}} \sqrt{N_{r,n_B}}} \sum_{\eta \in \mathcal{C}} \varphi_{n_B}^\eta \langle r' | P_\eta H | r \rangle \quad (2.28)$$

We used that the Hamiltonian commutes with the permutations $HP_\sigma = P_\sigma H$, their orthogonality $P_\sigma^T = P_{\sigma^{-1}}$, and the closeness of the subgroup $\sigma'^{-1}\sigma = \eta \in \mathcal{C}$. Therefore, the two sums, $\sigma', \sigma \in \mathcal{C}$, are reduced to a single sum over $\eta \in \mathcal{C}$ by absorbing the phase factors

Algorithm 3: Derivation of the spatially symmetrized Hamiltonian $H = \sum_i h_i$ in a specific sector n_B .

```

Determine  $\varphi_{n_B}^\eta$  for all possible  $\eta \in \mathcal{C}$                                      // cf. Equation 2.29
 $\mathcal{R}_{n_B}, \mathcal{N}_{n_B} = []$                                                          // valid representative states and norms
for  $|r\rangle \in \mathcal{R}$  do
     $N_{r,n_B} = \sum_{\eta \in \mathcal{C}} \varphi_{n_B}^\eta \langle r | \eta | r \rangle$ 
    if  $|N_{r,n_B}| > 0$  then
         $\mathcal{R}_{n_B}.$ append( $|r\rangle$ )
         $\mathcal{N}_{n_B}.$ append( $N_{r,n_B}$ )
    end
 $H^{n_B} = \text{zeros}(|\mathcal{R}_{n_B}|, |\mathcal{R}_{n_B}|)$                                      // dimension is  $|\mathcal{R}_{n_B}|$ 
for  $|r\rangle \in \mathcal{R}_{n_B}$  do
    for  $h_i \in H$  do
        Calculate  $\alpha|S\rangle = h_i|r\rangle$  for  $\alpha \in \mathbb{R}$  and  $|S\rangle \in \mathcal{S}_{n_{\text{up}}}^S$ 
        Determine  $\Lambda = \{\lambda_1, \dots, \lambda_f\} \subseteq \mathcal{C}$  such that  $|r'\rangle = \lambda_i|S\rangle \in \mathcal{R}_{n_B}$ 
        //  $|r'\rangle$  is a valid representative states
         $H_{r'r}^{n_B} += \frac{\alpha}{\sqrt{N_{r',n_B} N_{r,n_B}}} \sum_{\lambda_i \in \Lambda} \varphi_{n_B}^{\lambda_i}$            // cf. Equation 2.28
    end
end

```

in

$$\varphi_{n_B}^\eta = \sum_{\sigma, \sigma' \in \mathcal{C}, \text{ s.t. } \sigma'^{-1}\sigma = \eta} e^{2\pi i \sum_{i=1}^U n_B(i)(n_\sigma(i) - n_{\sigma'}(i))/L_i}. \quad (2.29)$$

Allowing two different sectors n_B and $n_{B'}$ for the combined phase factor Equation 2.29 yields zero, reflecting the orthogonality of the basis states. In general, $H|r\rangle$ produces non-representative states $|q\rangle \notin \mathcal{R}$. There is – at least one – permutation(s) $\lambda_i \in \mathcal{C}$ that maps the state to its representative state: $P_{\lambda_i}|q\rangle$. These permutations are the only contributing terms in Equation 2.28. The whole procedure of deriving the matrix elements is outlined in Alg. 3.

While the above description was considering a spin system, it can be extended to fermions where an up-/down-spin on a specific site refers to the occupation/absence of a fermion. However, dealing with fermionic sign requires special care when applying a permutation $\sigma \in S_N$ to a fermionic state. Let $|0\rangle$ denote the vacuum, a simple product state with n_{up} fermions in a system of N orbitals is given by

$$|\Psi\rangle = c_{k_1}^\dagger \dots c_{k_{n_{\text{up}}}}^\dagger |0\rangle \quad \text{with} \quad 1 \leq k_1 < \dots < k_{n_{\text{up}}} \leq N. \quad (2.30)$$

The operators c_i^\dagger and c_i denote the usual creating and annihilation operators. The procedure from above applies analogously, but the permutation of fermions has to obey the commutation

relation: $\{c_i^\dagger, c_j\} = \delta_{ij}$. The permutation operator associated with σ is

$$P_\sigma = \sum_{k_1 < \dots < k_{n_{\text{up}}}} c_{\sigma(k_1)}^\dagger \dots c_{\sigma(k_{n_{\text{up}}})}^\dagger c_{k_1} \dots c_{k_{n_{\text{up}}}}. \quad (2.31)$$

2.2 Numerical linked cluster expansions

Cluster expansion methods are frequently used in many areas of physics. Their great advantage is the absence of finite-size effects, making them powerful in three dimensions where other established methods are limited. In particular, the numerical linked cluster expansions (NLCE) [125, 126, 127, 128] is a promising alternative to study finite-temperature properties in strongly interacting and frustrated many-body systems. In a spirit similar to a high-temperature expansion, the algorithm systematically builds up the infinite lattice by pre-defined units to determine extensive thermodynamic quantities in the thermodynamic limit. Frequently studied observables are energy, magnetic susceptibility, entropy, heat capacity, magnetization, spin correlations, and more involved ones. The broad applicability of the approach allows its application to arbitrarily complex systems.

The method has already been successfully applied to quantum magnetism on various lattices including the square, kagomé, or pyrochlore [125, 126, 127, 129, 130, 131, 128, 132, 133]. Besides studying thermodynamic properties of these systems, it allows for a better understanding of phase transitions [134, 135, 136] and can be applied to more complicated systems [137, 138, 139, 140]. Further, it has been generalized to non-equilibrium properties [141, 142, 143, 144] and even dissipative systems [145].

The basic idea is the following: the algorithm systematically generates all possible translationally invariant subclusters starting from an elementary building block(s) (BBs) order by order. By comparing their topological structure, equivalent clusters are reduced to topologically invariant cluster with a *multiplicity* counting the number of possible translationally invariant embeddings. Note that there is a crucial difference between translationally and topologically invariant clusters! For example, the two translationally invariant dimers on the square lattice pointing along x and y are reduced to one topologically distinct dimer with a multiplicity of two. All topologically invariant clusters contribute to the thermodynamic observable, converging to the correct result in the thermodynamic limit. Each cluster's contribution is composed of its *weight* and *multiplicity*. The weight refers to the observable of interest, *e.g.* heat capacity at some temperature, and is defined recursively as it includes contributions of smaller subclusters. After the BBs is identified, the algorithm can be summarized in three steps: (i) The expansion starts from the pre-defined unit(s) and successively generates larger connected clusters. (ii) The number of clusters is reduced by evaluating their topological structure. (iii) Each topological invariant cluster has to be solved using full ED such that the observable of interest is determined. Its weighted contribution is obtained by subtracting the weights of smaller subclusters.

The algorithm faces two bottlenecks. First, the number of generated clusters scales *superexponentially*. Second, the computational cost of solving larger clusters scales exponentially with the Hilbert space dimension. However, reducing topologically equivalent graphs and maximizing the benefits of symmetries, as discussed in Section 2.1, significantly reduce the complexity. Therefore, sufficiently high orders become reachable to access non-trivial temperature regimes.

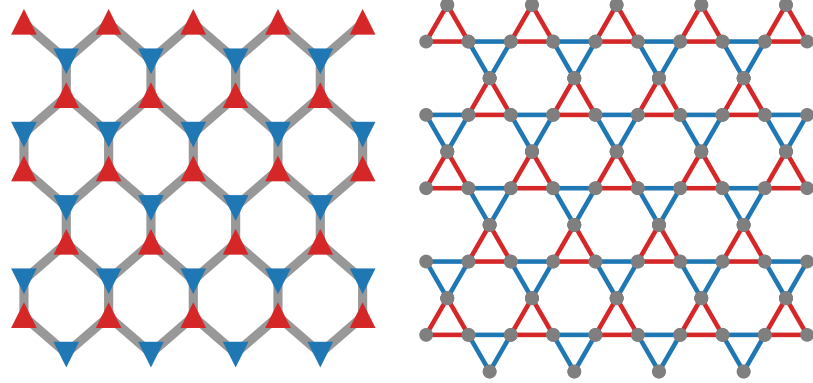


Figure 2.7: Reduced graph (left) for a triangular-based NLCE in the kagomé lattice (right). The up- and down-pointing triangles are identified with the sites in the honeycomb lattice.

The lowest accessible temperature depends on the particular phase of the model and the utilized BBs.

We present a general formulation of the NLCE algorithm for complex lattices allowing arbitrary decompositions based on different expansion units. This section is split into three parts. First, we describe the basic recipe to determine topologically invariant clusters, their multiplicity, and their weight for arbitrary BBs. We further examine the application of resummation algorithms which have proven valuable in many – but not all – models. Second, we present some results for different models, discuss similarities and differences, and address the advantages of different building blocks. Lastly, we summarize the most important results and give a brief outlook for future goals.

2.2.1 Basic recipe

The motivation behind the algorithm is the following: while observables at high temperatures are essentially determined by small units, *e.g.* triangles in the kagomé lattice, due to the short correlation length, lower temperatures require contributions of larger clusters as the correlation length increases. The NLCE algorithm regulates the contribution of larger clusters by smaller clusters yielding a recursive summation order by order. It generates a set of topologically invariant clusters $c \in \mathcal{T}_n$ for each order and multiplicities L_c , counting the number of translationally invariant embeddings of c . The thermodynamic observable of interest is evaluated for all clusters $\langle O_c \rangle_\beta$. Each cluster enters with respect to its multiplicity L_c and a weight $W[\langle O_c \rangle_\beta]$ which is

obtained from the observable:

$$\langle O \rangle_\beta^m = \sum_{n=0}^m \sum_{c \in \mathcal{T}_n} L_c W[\langle O_c \rangle_\beta] \quad \text{with} \quad W[\langle O_c \rangle_\beta] = \langle O_c \rangle_\beta - \sum_{c' \subset c} W[\langle O_{c'} \rangle_\beta] \quad (2.32)$$

The weight is obtained by determining the observable and subtracting contributions of all connected subclusters $c' \subset c$. The recursive definition induces that any extensive quantity, like energy, heat capacity, or entropy, vanishes for disconnected clusters². Therefore, only connected clusters are included in the expansion.

Elementary building blocks The initial – and most important – step is identifying the unit cell and its BBs. A proper choice of the building blocks is crucial as both bottlenecks, the number of topologically invariant clusters, and their sizes should be reached simultaneously. The chosen unit cell for the expansion does not have to correspond to the unit cell of the underlying Bravais lattice but has to cover the entire lattice. It can be composed of multiple (sometimes overlapping) BBs. The number of blocks per unit cell is denoted by $N_C \geq 1$. For example, the unit cell of a triangular-based expansion in the kagomé lattice exhibits two blocks: up- and down-pointing triangles. It is helpful to introduce the *reduced lattice* formed by the BBs of each unit cell. Edges between different blocks arise from different mechanisms, as they can represent a physical bond or a shared physical site between both BBs. The latter applies to the triangle-based expansion in the kagomé lattice where two adjacent triangles share a site. Notably, the expansion is carried out in the reduced lattice! In the case of the kagomé, the reduced lattice corresponds to the honeycomb lattice where its A and B sites are identified as the up- and down-pointing triangles as illustrated in Figure 2.7. The algorithm determines the thermodynamic observable for *one* unit cell. This corresponds to two triangles in the case of the triangular expansion in the kagomé lattice. However, since each node is shared between two instances, the unit cell consists of $6/2 = 3$ physical nodes. In general, nodes can also be shared between more BBs.

Connected clusters Each order in the expansion generates a set of connected and translationally – not topologically – invariant clusters \mathcal{C}_n in the reduced lattice. These clusters are built of n BBs, *e.g.* connected vertices in the honeycomb lattice. Each cluster $c \in \mathcal{C}_n$ represents a *physical* cluster in the full lattice by expanding its reduced nodes, denoted by $\mathcal{E}[c]$. For example, two connected reduced nodes in the honeycomb refer to an hourglass composed of two adjacent triangles in the kagomé lattice. While the expansion is performed on the reduced lattice, the topological structure and the physical observables are examined in the expanded physical lattice.

Topological invariance All connected clusters in \mathcal{C}_n contribute to the thermodynamic observable. However, many clusters are topologically equivalent, exhibiting the same Hamiltonian

²Let a cluster c contain two disconnected parts $c_1, c_2 \subset c$. Any extensive quantity is written as $\langle O_c \rangle_\beta = \langle O_{c_1} \rangle_\beta + \langle O_{c_2} \rangle_\beta$. Then, the recursive definition of the weight yields $W[\langle O_c \rangle_\beta] = 0$.

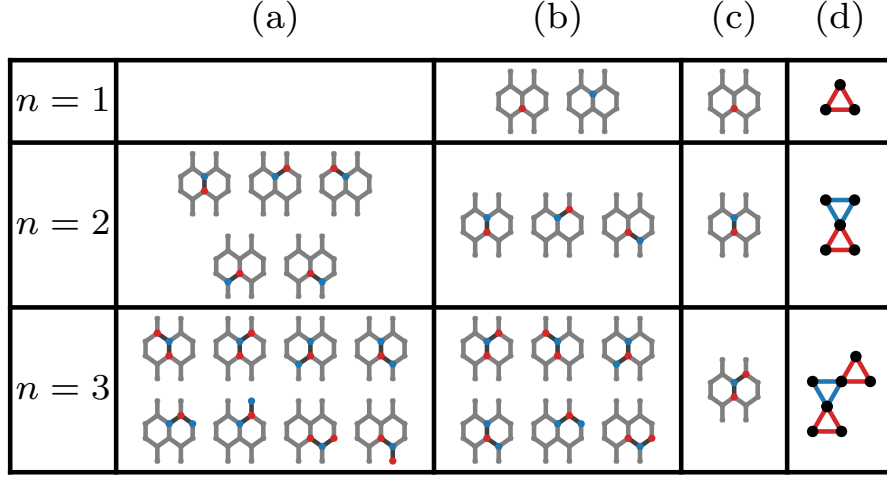


Figure 2.8: Different steps of the NLCE algorithm for a triangular-based expansion in the kagomé lattice. Column (a) shows clusters obtained from expanding translationally invariant clusters \mathcal{C}_{n-1} . Translationally invariant clusters are listed in column (b). Column (c) shows the topological reduction \mathcal{T}_n obtained from column (b), \mathcal{C}_n . The expanded full (physical) lattice $\mathcal{E}[c]$ for $c \in \mathcal{T}_n$ is shown in column (d).

and, therefore, the same physical observable. Two clusters $c, c' \in \mathcal{C}_n$ are equivalent if their expanded graphs $\mathcal{E}[c]$ and $\mathcal{E}[c']$ are topologically invariant. This means an automorphism mapping $\mathcal{E}[c]$ to $\mathcal{E}[c']$ exists, which preserves the internal structure, such as edges and color attributes. In that way, it is possible to reduce the number of connected clusters \mathcal{C}_n to topologically invariant cluster \mathcal{T}_n . Hence, each invariant cluster c exhibits a multiplicity L_c counting the number of equivalent instances in \mathcal{C}_n . Connected and translationally invariant (b), topologically invariant (c), and their expanded clusters (d) are shown in Figure 2.8 for the triangular expansion in the kagomé lattice.

Expansion $n \rightarrow n + 1$ We now describe the precise expansion procedure from order n to $n + 1$. The first order includes all isolated BBs within the unit cell. These are all translationally invariant clusters consisting of a single block and define \mathcal{C}_1 with $|\mathcal{C}_1| = N_C$. In the case of the kagomé lattice, the first order refers to both sites in the unit cell of the honeycomb lattice: the blue and red nodes corresponding to the up- and down-pointing triangles, cf. Figure 2.7. The expansion from the order n to $n + 1$ is organized in the following steps: (i) expanding all clusters in \mathcal{C}_n and removing *translationally* invariant clusters to obtain \mathcal{C}_{n+1} , (ii) reducing \mathcal{C}_{n+1} to obtain topologically equivalent clusters \mathcal{T}_{n+1} and their multiplicity, and (iii) solving the individual clusters and determine their weights.

- (i) The bare expansion is performed in the reduced graph. All translationally invariant clusters

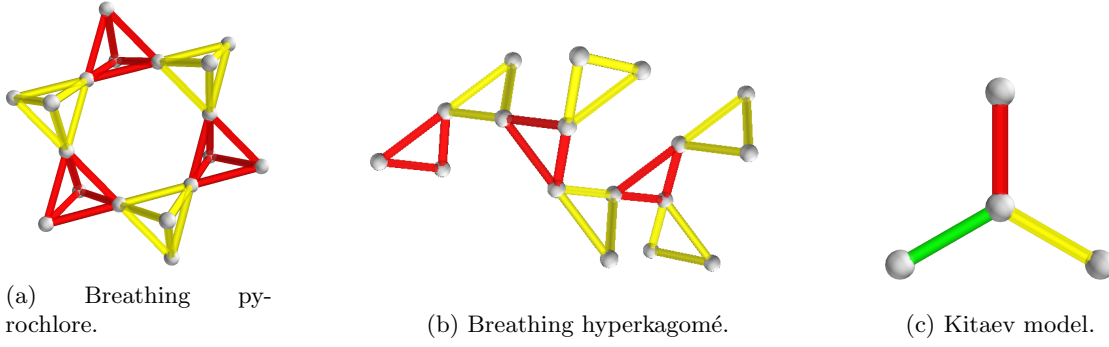


Figure 2.9: Cluster generated from different expansions in different lattices. The color code illustrates different anisotropic bonds.

$c \in \mathcal{C}_n$ of order n are expanded individually. Each cluster c is extended by all unoccupied adjacent nodes to generate new clusters containing $n + 1$ BBs. Translationally – not topologically – equivalent clusters are discarded, and only translationally invariant clusters are collected in \mathcal{C}_{n+1} . The translational symmetries are defined by the Bravais vectors referring to the chosen unit cell, which do not necessarily refer to the Bravais vectors of the underlying lattice. Figure 2.9 illustrates different clusters arising in different expansions.

- (ii) After all clusters in \mathcal{C}_{n+1} are determined, their topological structure is examined. The topological comparison is made on the level of the full lattice, and the reduced nodes have to be expanded $\mathcal{E}[c]$. Identifying the clusters as graphs with nodes, edges, and color attributes allows us to exploit graph tools like *Nauty & Traces* [123]. It is advisable to introduce hashes that include the number of sites, number of edges, and potentially number of color attributes to simplify the topological comparison. Thereby, the set \mathcal{C}_{n+1} is reduced to \mathcal{T}_{n+1} and each topological cluster c exhibits a multiplicity counting the possible embeddings:

$$|\mathcal{C}_{n+1}| = \sum_{c \in \mathcal{T}_{n+1}} L_c \quad (2.33)$$

- (iii) The observable of interest, $\langle O_c \rangle_\beta$, is determined for all clusters in $c \in \mathcal{T}_{n+1}$. Symmetries, as discussed in Section 2.1, reduce the complexity significantly. The weighted contribution to the final expansion is obtained by Equation 2.32. Notably, the embedding of connected subclusters $c' \subset c$ is performed in the reduced graph! The procedure is illustrated in Figure 2.10.

The whole expansion procedure is illustrated for the kagomé in Figure 2.8. Column (a) shows all expanded clusters obtained from \mathcal{C}_{n-1} . The expanded clusters are reduced to translationally invariant clusters \mathcal{C}_n in column (b). Reducing the number of these clusters according to their topological structure yields column (c). The full physical graph of the topologically invariant

$$\begin{aligned}
W[\text{cluster}] &= O[\text{cluster}] - W[\text{cluster}_1] - W[\text{cluster}_2] \\
&\quad - W[\text{cluster}_3] - W[\text{cluster}_4] - W[\text{cluster}_5] \\
&= O[\text{cluster}] - 2W[\text{cluster}_1] - 3W[\text{cluster}_2]
\end{aligned}$$

Figure 2.10: Definition of the NLCE weight for a specific cluster occurring in a triangular-based expansion in the kagomé lattice, *cf.* Equation 2.32. W and O refer to the weight and observable.

clusters is shown in column (d).

It is possible to exploit additional point group symmetries to reduce the computational complexity of the expansion. The symmetries lower the number of translationally invariant clusters to symmetrically invariant clusters before reducing them to topologically invariant clusters. Applying point group symmetries induces additional complexity to the algorithm and must be carefully examined depending on the BBs. However, in practice, using point group symmetries is not necessary as the derivation of the topological clusters and their multiplicity is not the limiting factor.

If some building blocks are sharing sites, it is necessary to include the zeroth order in the expansion for some observables, *e.g.* entropy or energy in a magnetic field. These observables have a non-zero contribution for a single isolated spin, which, therefore, has to be included in the expansion. Thus, the weight of each cluster of size N is obtained by additionally subtracting the contribution of N single spins. For example, the weight of a single triangle is regulated by its three individual spins.

Resummation algorithms Typically, the breakdown of convergence is well-marked when consecutive orders diverge from each other at some temperature. The individual orders separate rapidly. In these cases, series acceleration algorithms are powerful as they boost the convergence to much lower temperatures. Two commonly used resummation algorithms are Euler's transformation and Wynn's algorithm [126, 128]. The following relation defines Euler's transformation:

$$\langle O \rangle_\beta^\infty = \sum_{n=0}^{\infty} (-1)^n u_n = \sum_{n=0}^{\infty} \frac{(-1)^n}{2^{n+1}} [\Delta^n u_0] \quad (2.34)$$

Here, u_n includes the n th NLCE order $u_n = (-1)^n (\langle O \rangle_\beta^n - \langle O \rangle_\beta^{n-1})$ and Δ is the forward difference operator³. The convergence is boosted by including the first k bare NLCE orders and

³The first few orders are:

$$\Delta^0 u_n = u_n, \quad \Delta^1 u_n = u_{n+1} - u_n, \quad \Delta^2 u_n = u_{n+2} - 2u_{n+1} + u_n \quad (2.35)$$

then applying the difference operator:

$$\langle O \rangle_\beta^\infty = \sum_{n=0}^{k-1} (-1)^n u_n + \sum_{n=0}^{\infty} \frac{(-1)^n}{2^{n+1}} [\Delta^n u_k] \quad (2.36)$$

Usually, the diverging behavior is induced by a single “misbehaving” cluster. Applying the resummation algorithm regulates this contribution. As discussed in the following subsection, some models do not exhibit the rapid divergence, and neither approach allows for a reliable convergence boost. Counterexamples are the Kitaev honeycomb model, *cf.* Figure 2.12a, or a hexagon-based expansion in the pyrochlore lattice, *cf.* Section 5.3. Other acceleration series might be applicable in these cases. Detailed information about different resummation algorithms, their implementation, and validity, as well as limitations, are given in Ref. [146, 147, 148].

2.2.2 Results and convergence

The general implementation of the algorithm allows its applications to diverse models and various BBs to study the algorithm’s convergence. The convergence criterion is defined as the agreement between consecutive orders up to some temperature. The lowest accessible temperature depends on the model, its parameters, and the applied BBs. Understanding convergence and the influence of different BBs is essential for future applications.

In a trivial paramagnetic phase at high temperatures, all properties are captured by small clusters if the correlation length is short enough. Hence, the weights of larger clusters are essentially zero since the observable is extensive and the weight is recursively defined. Therefore, including the first (or a few) order(s) is sufficient to capture the high-temperature regime. However, the behavior at lower temperatures with an increasing correlation length is not evident.

Let us start by evaluating the effect of different BBs. Choosing an optimal building block is not trivial, as various aspects must be considered. Most importantly, both bottlenecks, the Hilbert space dimension, and the number of topologically invariant clusters should prohibit further calculations at the same order. Depending on the reduced graph’s connectivity, adequate blocks contain around two to three sites. Furthermore, the BBs should represent essential features of the model, such as frustrated tetrahedra in the pyrochlore lattice, which are extremely powerful at finite temperatures. Figure 2.11 evaluates three expansions on the pyrochlore lattice based on different BBs – single site, tetrahedron, and its (non-overlapping) unit cell. The underlying Bravais lattice is an fcc lattice with four, two, and one BBs, respectively⁴. It compares the heat capacity and magnetic susceptibility per site for the three expansions and reveals the superiority of the tetrahedron expansion, as it is converged down to $T \approx 0.2 J$. While the number of clusters for the single-site expansion scales too rapidly to reach sufficiently large clusters, the unit-cell expansion does not represent the essential physical features – the frustrated tetrahedra.

⁴Similar to the triangular expansion in the kagomé, the reduced lattice of the tetrahedron-based expansion’s is the diamond lattice.

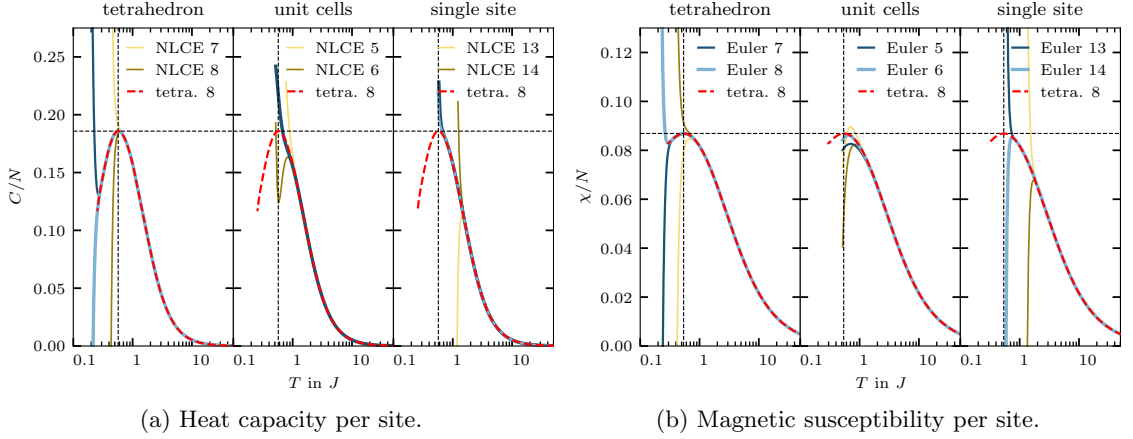


Figure 2.11: Benchmarking different expansions in the pyrochlore lattice. (a) and (b) compare the specific heat and magnetic susceptibility per site for the individual expansions. The 6th order of unit cell expansion only includes 48 of 100 topologically invariant clusters with full exact diagonalization and 8 clusters in combination with canonical typicality.

The general implementation presented in this thesis allows for studying various models. Several frustrated two-dimensional lattices like the kagomé, the ruby, the checkerboard, and the Shastry-Sutherland model were investigated. Figure 2.12a fully resolves the Schottky anomaly in the kagomé Heisenberg antiferromagnet ($J = 1$) located at $T_{\max} = 0.66$ with $C_{\max}/N = 0.19$. Extensive numerical calculations in three dimensions were performed for the pyrochlore, simple fcc, and hyperkagomé lattices. In addition to frustrated magnets, more exotic systems like the Kitaev honeycomb model were studied, *cf.* Figure 2.12b. The expansion is based on the *star* illustrated in Figure 2.9c, where the different bond colors reflect the different couplings of the model. The topological reduction exploits the fact that the colors can rotate by simply applying a global rotation in spin space. Furthermore, all clusters exhibit dangling bonds (i, j) , which induce a large number of conserved quantities as the exterior operator $S_i^z S_j^z$ is diagonal. Exploiting this allows calculating clusters containing up to 28 spins using full ED. It reveals a striking agreement with exact QMC data [149], resolving both the high- and low-temperature peak. However, it does not fully cover the intermediate-temperature range yet. The Kitaev model on the honeycomb is exactly solvable and, therefore, well understood [69]. Crucially, it hosts a spin liquid at low temperatures, which is likely favorable for NLCE calculations as it does not break any symmetry. However, it is remarkable that finite clusters can capture the ground state and low-lying excitations responsible for the low-temperature peak.

Understanding the convergence of the algorithm is not trivial as demonstrated with both examples in Figure 2.12. In the most common case, a single or few clusters start to “misbehave” below some temperature. The reasons for this are diverse, as it can be induced by an increasing correlation length or due to the geometry of these clusters. The latter was frequently observed in the kagomé and pyrochlore lattices when larger clusters with additional hexagonal

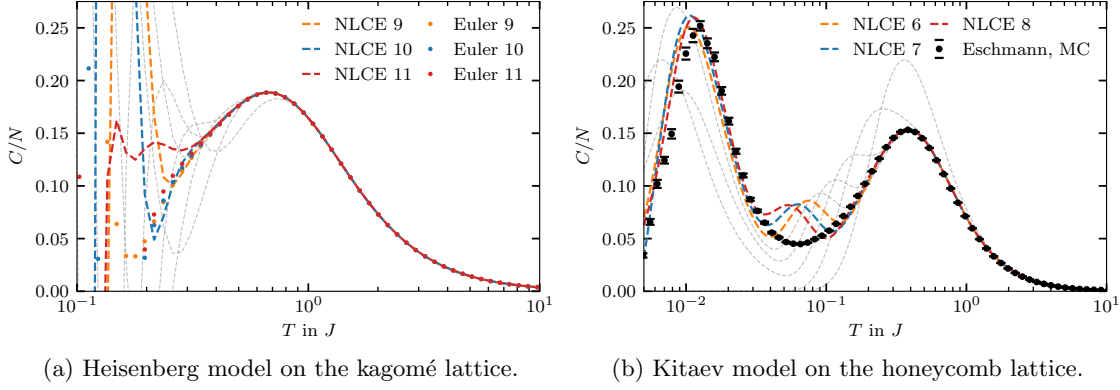


Figure 2.12: (a) Specific heat per site in the antiferromagnet Heisenberg model on the kagomé lattice and (b) the Kitaev model on the honeycomb lattice. The expansion in the kagomé (Kitaev) model is based on the triangular expansion in Figure 2.8 (star expansion in Figure 2.9c). The 11th order in the kagomé contains 86 of 113 topologically invariant clusters. Gray lines represent lower orders. Exact QMC data are available for the Kitaev model for comparison [149].

loops were included. Even if the observable disagrees slightly from smaller clusters scaling it with the multiplicity – which grows exponentially – induces a rapid divergence, signaling the failure of the expansion. Including the next order might regulate the diverging contribution, regaining convergence, or amplify the diverging behavior. Due to the recursive definition of weight, the misbehaving cluster is subtracted from the larger ones; this often induces an alternating behavior. Crucially, we further identified models that do not exhibit the divergent behavior as just described. Interestingly, they capture the high- and low-temperature limit but fail to resolve the intermediate-temperature regime. Examples are the Kitaev model on the honeycomb lattice, *cf.* Figure 2.12b, and a hexagon-based expansion in pyrochlore lattice. These models seem to exhibit a particular simple (for NLCE) ground state. The pyrochlore case is discussed in detail in Section 5.3.

2.2.3 Final remarks

To summarize, NLCE provides a powerful tool to evaluate the thermodynamic properties of complex models in arbitrary dimensions at finite (and zero, *cf.* Section 5.3) temperatures.

Its advantages are

- its broad applicability,
- its independence of dimensionality, and
- its unbiased and controlled nature producing data in the thermodynamic limit.

Maximizing the benefits of symmetries and exploiting current computational resources allow predictions down to non-trivial temperatures. That way, we can push the state-of-the-art calcu-

n	N	$ \mathcal{C}_n $	$ \mathcal{T}_n $
0	1	4	1
1	4	2	1
2	7	4	1
3	10	12	1
4	13	44	2
5	16	182	3
6	18,19	796	6
7	21,22	3612	10
8	24,25	16786	24
9	26,27,28	79426	49

Table 2.1: Number of connected $|\mathcal{C}_n|$ and topologically distinct $|\mathcal{T}_n|$ clusters for the tetrahedron-based expansion.

lation down to much lower temperatures than previously accessible [125, 126, 127, 137, 138, 139, 140, 129, 131, 130, 128, 134, 141, 132, 142, 143, 133, 135, 136, 144, 145].

The most significant progress was achieved in a tetrahedron-based expansion on the pyrochlore, where hexagonal and octagonal loops were included for the first time [130, 131, 132, 135, 133, 136]. The progress was possible due to the automatic detection algorithm for spatial symmetries, which have proven extremely valuable for clusters of tetrahedra as they reveal an enormous number of automorphisms. Clusters containing $N \approx 24$ sites exhibit up to two million automorphisms. Exterior tetrahedra exhibit multiple independent sets of generators rotating two (or even three) spins not attached to any other tetrahedron yielding a massive number of symmetry sectors. Thus, symmetries enable full diagonalization of clusters with up to $N = 25$ spin-1/2 – unprecedented for generic clusters – in the eighth order. The numbers of connected and topologically invariant clusters per order are displayed in table Table 2.1.

Results for the Kitaev model and the hexagon-based expansion on the pyrochlore suggest that NLCE can capture the low-temperature limit while diverging at intermediate temperatures. As we do not observe the convergence in the zero temperature limit for other building blocks in the pyrochlore, the choice of BBs is essential and might reflect a possible symmetry breaking of the ground state. The zero-temperature convergence is conceptually interesting as it suggests that NLCE – a finite-temperature expansion – provides insights into the low/zero-temperature limit. A similar observation was made earlier [139]. Applicable resummation algorithms for the intermediate temperature regime might provide further insights and should be considered in future studies.

As the expansion is extremely sensitive to errors, most results presented above are obtained using full ED. This limits the maximal cluster sizes to approximately 25 spins depending on the symmetries of the clusters. Hence, it is desirable to push the number of sites using approximate methods by the cost of a small error: $W[\langle O_c \rangle_\beta] + \delta W[\langle O_c \rangle_\beta]$. However, combining the errors, even if they are controlled, with the exponentially increasing multiplicities induce diver-

gencies⁵. The divergent behavior occurs when the ratio between the weight and its error is small, $|W[\langle O_c \rangle_\beta]|/|\delta W[\langle O_c \rangle_\beta]| \ll 1$. This usually happens in the high-temperature regime when the weights of large clusters are small. A possible controlled approach to include approximate methods in future studies is to carefully evaluate the ratio between the weight and its error. The contribution of a larger cluster is included if the ratio is above some threshold and otherwise set to zero. Note that the Lanczos algorithm [107] is exact in the zero-temperature limit and allows for including larger clusters at $T = 0$ [139]. Hence, the sparsity of the Hamiltonian can be exploited to reach higher orders.

All in all, NLCE is particularly well suited to study the finite-temperature properties of frustrated magnets in three dimensions as it does not suffer from the dimensionality or the frustrated character. The generic description in the thermodynamic limit, based on a unit cell, allows adopting the code to arbitrarily complex models. It produces reliable and unbiased results in the thermodynamic limit down to non-trivial temperatures previously inaccessible. Chapter 4 discusses the application of NLCE to the pyrochlore lattice – the archetype of frustrated magnetism in the three dimensions. It presents extensive numerical data for Heisenberg antiferromagnet [1] and demonstrates the broad applicability of NLCE by modeling experimental data of $\text{Ce}_2\text{Sn}_2\text{O}_7$ and $\text{Ce}_2\text{Zr}_2\text{O}_7$ [3].

⁵One-dimensional systems are an exception, as the multiplicities remain constant [144].

2.3 Cluster expansion for exponentials

Variational approaches are commonly used in physics to optimize different properties. This section discusses a generic method to evaluate variational wavefunctions obtained from an exponential. Exponential operators are frequently used in quantum mechanics as they describe real- and imaginary-time evolution [110, 150, 111, 151]. Here, the algorithm aims to achieve a suitable “dressing” of valence-bonds crystals to minimize their energy. The idea is motivated by the observed zero-temperature convergence of the hexagon-based NLCE in the pyrochlore lattice and is discussed in [Section 5.3](#).

Starting from some initial state $|\Psi_0\rangle$, the variational wavefunction is described by

$$|\Psi_\lambda\rangle = e^{-S(\lambda)}|\Psi_0\rangle, \quad (2.37)$$

where λ is a set of variational parameters and $S(\lambda)$ is an arbitrary operator. Many numerical methods are restricted to clusters of finite size and do not provide an unbiased estimate in three dimensions. Therefore, we introduce a cluster expansion allowing us to evaluate the wavefunctions reliably in the thermodynamic limit. The procedure is based on the *linked cluster theorem* [112, 113], which makes a systematic expansion possible. Note that the expansion is fundamentally different from NLCE.

The algorithm decomposes the lattice such that each site participates in precisely one group p , which we call “plaquettes”. The decomposition of the lattice separates the Hamiltonian into terms acting on a plaquettes and connecting two plaquettes:

$$H_0 = \sum_p H_p \quad \text{and} \quad V = \sum_e V_e \quad (2.38)$$

The family of valence-bond crystals discussed in [Section 5.3](#) has a particularly simple form suited for the variational approach [Equation 2.37](#). Hence, for the sake of simplicity, we assume that all plaquettes are given by a closed ring of length L_p coupled by a quartet of doubly frustrated bonds. In the pyrochlore lattice, the plaquettes refer to hard (non-overlapping) hexagons coupled with four bonds provided by the tetrahedra. The same decomposition (squares instead of hexagons) applies to the checkerboard lattice, as illustrated in [Figure 2.13](#) (right side). The local Hamiltonians on the plaquettes are simple unfrustrated loops that exhibit a non-degenerate singlet ground state accompanied by a robust finite-size gap of order $1 J$ ($\sim 0.69 J$) for $L_p = 4$ ($L_p = 6$) for the isotropic Heisenberg model. As we are interested in the low-energy limit, the wavefunction is initially prepared in the ground state of H_0 – a simple product state:

$$|\Psi_0\rangle = \bigotimes_p |0\rangle_p. \quad (2.39)$$

While the energy density on the plaquettes is minimized by $|\Psi_0\rangle$, two plaquettes are uncor-

related, and V does not contribute any energy: $\langle \Psi_0 | V | \Psi_0 \rangle = 0$. Hence, we consider a relatively simple variational approach depending only on one parameter α , which induces correlations between the plaquettes. It is equivalent to an imaginary-time evolution of $|\Psi_0\rangle$ with a time step $\alpha \in \mathbb{R}$ performed on the connecting bonds:

$$|\Psi_\alpha\rangle = e^{-\alpha V} |\Psi_0\rangle \quad (2.40)$$

The isolated plaquette ground state is recovered for $\alpha = 0$. Evolving $|\Psi_0\rangle$ in imaginary time yields a trade-off as it lowers the energy density on the inter-plaquette bonds but increases the energy on the plaquettes. The variational energy per site consists of H_0 and V :

$$\frac{E_\alpha}{N} = \frac{1}{L_p} \frac{1}{N_p} \frac{\langle \Psi_\alpha | H_0 + V | \Psi_\alpha \rangle}{\langle \Psi_\alpha | \Psi_\alpha \rangle} = \frac{1}{L_p} \frac{1}{N_p} \frac{\langle \Psi_0 | e^{-\alpha V} (H_0 + V) e^{-\alpha V} | \Psi_0 \rangle}{\langle \Psi_0 | e^{-2\alpha V} | \Psi_0 \rangle} \quad (2.41)$$

N_p is the number of plaquette. Strikingly, it turns out that evolving $|\Psi_0\rangle$ in imaginary time reveals a pronounced minimum exhibiting a competitive ground-state energy for the models discussed in [Section 5.3](#). The remainder of this section focuses solely on the algorithm and does not interpret the physical results.

Similar to NLCE, it is convenient to introduce the notation of the reduced lattice. Thereby, we identify the plaquettes with its nodes and edges between the reduced nodes include the quartet of doubly frustrated bonds. The reduced lattice of the checkerboard lattice corresponds to a simple square lattice as shown on the left side of [Figure 2.13](#). The coordination number of the reduced lattice counts the attached edge operators V_e and equals the plaquette length $c = L_p$.

The initial wavefunction is a spin-singlet and symmetric on each plaquette. Since V acts equally on all plaquettes, the resulting wavefunction $|\Psi_\alpha\rangle$ has a uniform energy density on the plaquettes and a different uniform energy density on the edge terms. Therefore, we can exploit the invariance of the evolved state, and computing the energy *locally* is sufficient as all plaquette and edge terms are equivalent:

$$E_\alpha = \frac{1}{L_p} \left(\langle H_p \rangle_\alpha + \frac{c}{2} \langle V_e \rangle_\alpha \right) \quad (2.42)$$

The coordination number c refers to the number of attached edge operator V_e , $c = 4$ (6) for the square (hexagon), and the expectation value refers to $\langle O \rangle_\alpha = \langle \Psi_\alpha | O | \Psi_\alpha \rangle$. Hence, to compute the variational energy, it is necessary to determine the plaquette $O_{\text{loc}} = H_p$ and edge $O_{\text{loc}} = V_e$ contributions.

2.3.1 Linked cluster theorem

The linked cluster theorem permits a reliable and unbiased estimate of the variational energy in the thermodynamic limit. It evaluates E_α/N in powers of α using a systematic expansion including clusters composed of linked plaquettes. Local operators $\langle O_{\text{loc}} \rangle_\alpha$ are computed system-

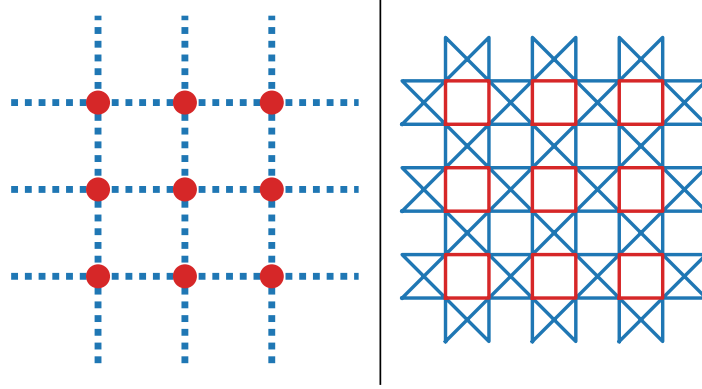


Figure 2.13: Reduced lattice of the checkerboard lattice. Nodes in the reduce lattice (left) are identified with plaquettes of the checkerboard lattice (right). Doubly frustrated bonds are reduced to a single edge connecting two plaquettes.

atically by evaluating connected diagrams attached to these operators. The contributing terms are regulated by connected correlation functions – also known as Ursell functions [152, 153, 154] – with respect to the initial wavefunction $|\Psi_0\rangle$. The contribution of disconnected terms vanishes due to the recursive definition ensuring the extensive scaling of the energy. The first three orders of the Ursell functions are:

$$\mathcal{U}_{|\Psi\rangle}[A] = \langle \Psi | A | \Psi \rangle \quad (2.43)$$

$$\mathcal{U}_{|\Psi\rangle}[A, B] = \langle \Psi | AB | \Psi \rangle - \langle \Psi | A | \Psi \rangle \langle \Psi | B | \Psi \rangle \quad (2.44)$$

$$\begin{aligned} \mathcal{U}_{|\Psi\rangle}[A, B, C] = & \langle \Psi | ABC | \Psi \rangle - \langle \Psi | AB | \Psi \rangle \langle \Psi | C | \Psi \rangle - \langle \Psi | AC | \Psi \rangle \langle \Psi | B | \Psi \rangle \\ & - \langle \Psi | BC | \Psi \rangle \langle \Psi | A | \Psi \rangle + 2 \langle \Psi | A | \Psi \rangle \langle \Psi | B | \Psi \rangle \langle \Psi | C | \Psi \rangle \end{aligned} \quad (2.45)$$

Higher-order Ursell functions are determined recursively or as derivatives from an exponential function [154].

The Taylor series of the exponential functions in $e^{-\alpha V} O_{\text{loc}} e^{-\alpha V}$ generates the contributing terms for the linked cluster theorem. Both exponentials induce two sums running over a and b , where V^a is acting from the left and V^b is acting from the right of the local observable. Powers of V generate multiple *independent* sums running over *all* edges. The Ursell functions annihilate

all disconnected terms such that the sum can be restricted to connected diagrams:

$$\langle O_{\text{loc}} \rangle_\alpha = \frac{\langle \Psi_\alpha | O_{\text{loc}} | \Psi_\alpha \rangle}{\langle \Psi_\alpha | \Psi_\alpha \rangle} \quad (2.46)$$

$$= \sum_{a,b=0}^{\infty} \sum_{\substack{e_1, \dots, e_{a+b} \\ \text{connected to } O_{\text{loc}}}} \frac{(-\alpha)^{a+b}}{a!b!} \mathcal{U}_{|\Psi_0\rangle} [V_{e_1}, \dots, V_{e_a}, O_{\text{loc}}, V_{e_{a+1}}, \dots, V_{e_{a+b}}] \quad (2.47)$$

There are a few things two point out. First, note that the expectation value of the Ursell function is defined with respect to $|\Psi_0\rangle$. Second, edges can be occupied multiple times, *e.g.* $e_i = e_j$, as they originate from independent sums. Third, the order of edges matters. Fourth, a collection of edges is connected if their subgraph, together with the support of the local operator, is connected. Therefore, the expansion differs for both operators in Equation 2.42 as H_p only covers a single plaquette, and V_e covers two plaquettes.

As the expression is quite abstract, we explicitly evaluate the nominator and denominator in Equation 2.46 and compare them to the linked cluster theorem Equation 2.47 in the first power of α . Edge operators V_e connected to O_{loc} are contained in $\mathcal{N}[O_{\text{loc}}]$. For example, four edges are attached to a plaquette in the checkerboard lattice, *cf.* Figure 2.13. Note that disconnected operators factorize, which simplifies the calculation:

$$\langle \Psi | V_e O_{\text{loc}} | \Psi \rangle = \langle \Psi | V_e | \Psi \rangle \langle \Psi | O_{\text{loc}} | \Psi \rangle \quad \text{for } V_e \notin \mathcal{N}[O_{\text{loc}}] \quad (2.48)$$

Following the linked cluster theorem, only connected terms to O_{loc} have to be considered. Expanding Equation 2.47 up to $a + b \leq 1$ yields only three possibilities:

$$\begin{aligned} \langle O_{\text{loc}} \rangle_\alpha &= \mathcal{U}_{|\Psi_0\rangle} [O_{\text{loc}}] - \alpha \sum_{V_e \in \mathcal{N}[O_{\text{loc}}]} \mathcal{U}_{|\Psi_0\rangle} [V_e, O_{\text{loc}}] - \alpha \sum_{e \in \mathcal{N}[O_{\text{loc}}]} \mathcal{U}_{|\Psi_0\rangle} [O_{\text{loc}}, V_e] + \mathcal{O}(\alpha^2) \quad (2.49) \\ &= \langle \Psi_0 | O_{\text{loc}} | \Psi_0 \rangle - 2\alpha \sum_{V_e \in \mathcal{N}[O_{\text{loc}}]} \langle \Psi_0 | V_e O_{\text{loc}} | \Psi_0 \rangle \\ &\quad + 2\alpha \sum_{V_e \in \mathcal{N}[O_{\text{loc}}]} \langle \Psi_0 | V_e | \Psi_0 \rangle \langle \Psi_0 | O_{\text{loc}} | \Psi_0 \rangle + \mathcal{O}(\alpha^2) \end{aligned}$$

Similarly, we can evaluate the nominator and denominator on the full lattice. Thereby, we

use the factorization property of disconnected operators:

$$\langle \Psi_\alpha | O_{\text{loc}} | \Psi_\alpha \rangle = \langle \Psi_0 | (1 - \alpha V + \mathcal{O}(\alpha^2)) O_{\text{loc}} (1 - \alpha V + \mathcal{O}(\alpha^2)) | \Psi_0 \rangle \quad (2.50)$$

$$\begin{aligned} &= \langle \Psi_0 | O_{\text{loc}} | \Psi_0 \rangle - 2\alpha \sum_{V_e} \langle \Psi_0 | V_e O_{\text{loc}} | \Psi_0 \rangle + \mathcal{O}(\alpha^2) \\ &= \langle \Psi_0 | O_{\text{loc}} | \Psi_0 \rangle - 2\alpha \sum_{V_e \in \mathcal{N}[O_{\text{loc}}]} \langle \Psi_0 | V_e O_{\text{loc}} | \Psi_0 \rangle \\ &\quad - 2\alpha \sum_{V_e \notin \mathcal{N}[O_{\text{loc}}]} \langle \Psi_0 | V_e | \Psi_0 \rangle \langle \Psi_0 | O_{\text{loc}} | \Psi_0 \rangle + \mathcal{O}(\alpha^2) \\ \langle \Psi_\alpha | \Psi_\alpha \rangle &= \langle \Psi_0 | 1 - 2\alpha V + \mathcal{O}(\alpha^2) | \Psi_0 \rangle = 1 - 2\alpha \sum_{V_e} \langle \Psi_0 | V_e | \Psi_0 \rangle + \mathcal{O}(\alpha^2) \end{aligned} \quad (2.51)$$

Multiplying the observable computed using the linked cluster theorem [Equation 2.49] with the denominator [Equation 2.51] yields the nominator [Equation 2.50] up to α^2 :

$$\langle O_{\text{loc}} \rangle_\alpha \cdot \langle \Psi_\alpha | \Psi_\alpha \rangle = \langle \Psi_\alpha | O_{\text{loc}} | \Psi_\alpha \rangle + \mathcal{O}(\alpha^2) \quad (2.52)$$

This verifies the linked cluster theorem in the first order. The procedure can be carried out analogously for higher orders. Even though the algorithm is restricted to connected terms, the complexity of identifying all connected graphs scales factorially!

2.3.2 Algorithm

This subsection presents a systematic way to identify all contributing terms such that variational energy can be computed in powers of α : $E_\alpha/N = \sum_{n=0} c_n(-\alpha)^n$. Note that all combination of $a + b = n$ have to be considered in Equation 2.47 to determine a specific coefficient c_n . The complexity of this problem lies in the vast number of terms. Expanding the sum straightforwardly is not feasible for large powers. The procedure for a given a and b in Equation 2.47 can be organized in four steps:

- (i) *Expansion.* We identify sets of edges $\{q_1, \dots, q_k\}$ that are, together with O_{loc} , connected and store them in \mathcal{C}_k for $k = 1, \dots, n$. The order does not matter, making this step computationally cheap. Note that the expansions for H_p and V_e are different.
- (ii) *Operator sequence.* Each term exhibits n edge operators that are placed independently, respecting the connectivity restriction. A particular set of connected edges $\{q_1, \dots, q_k\} \in \mathcal{C}_k$ derived in (i) induces a large number of operator sequences. Each sequence contains n edges (e_1, \dots, e_n) with $e_i \in \{q_1, \dots, q_k\}$. Note that the order is important for the sequence! To ensure connectivity, each edge has to be occupied at least once. The set of all edge sequences is denoted by \mathcal{S} .
- (iii) *Ursell function.* Each sequence $(e_1, \dots, e_n) \in \mathcal{S}$ represents an individual term in the equation. Combining the corresponding edge operators with the local operator, inserted at the

	$S = 1/2$		$S = 1$	
	E_{α_0}/N	(α_0)	E_{α_0}/N	(α_0)
Checkerboard	-0.51344	(0.30529)	-1.53393	(0.19406)
Bethe ($L_p = 4$)	-0.51344	(0.30513)	-1.53414	(0.19702)
Pyrochlore	-0.48947	(0.39321)	-1.48969	(0.24199)
Ruby	-0.48947	(0.39349)	-1.48984	(0.24307)
Bethe ($L_p = 6$)	-0.48955	(0.39606)	-1.48978	(0.24264)
Bethe ($L_p = 8$)	-0.48274	(0.43243)	-1.49355	(0.44012)

Table 2.2: Lowest variational energy E_{α_0}/N and the optimal parameter α_0 for all models considered and different spin lengths ($J = 1$).

$(a + 1)$ th position, generates an operator string containing $n + 1$ component. The resulting operator string is evaluated using $(n + 1)$ th Ursell function, $\mathcal{U}_{|\Psi_0\rangle} [V_{e_1}, \dots, V_{e_a}, O_{\text{loc}}, V_{e_{a+1}}, \dots, V_{e_{a+b}}]$, which produces many factorized terms as in Equation 2.43 to Equation 2.45.

- (iv) *Evaluation*. Lastly, the individual factorized operator terms are computed with respect to $|\Psi_0\rangle$. Each computation involves at least one (two) and at most $n + 1$ ($n + 2$) plaquettes for $O_{\text{loc}} = H_p$ ($O_{\text{loc}} = V_e$). The sparsity of spin operators can be exploited. Note that many factorized terms might be simplified further as they are not necessarily connected anymore.

While the expansion allows a controlled and unbiased way to compute the variational energy in the thermodynamic limit reaching sufficiently large orders is challenging. All individual steps presented above scale either *exponentially* or even *factorially* with n . Even though the expansion does not rely on full diagonalization (as NLCE), the vast number of terms is too demanding. Luckily, the particular ground state of investigated models – even plaquette length with the doubly frustrated bonds – simplifies the problem significantly. The expectation value of any edge operator V_e between two plaquettes vanishes when one is in its ground state $|0\rangle$:

$$(\langle 0| \otimes \langle \psi|) V_e (|0\rangle \otimes |\psi\rangle) = 0, \quad \forall |\psi\rangle. \quad (2.53)$$

Therefore, all operator strings are zero unless each plaquette is touched by at least *two* V_e . This is true if all edge operators occur twice or if they are periodically arranged – a periodic loop of plaquettes. Thus, sequences generated in (ii) only contribute if each node is touched by two edges. This significantly reduces the number of possible terms and makes computation up to order seven feasible.

2.3.3 Results

We carried out the expansion for various lattices – consistent with the constraints – and spin lengths. The models are composed of a plaquette with even length coupled via a quartet of doubly frustrated bonds. While the plaquette energy (E_{strong}) increases with $\alpha > 0$, the energy of the

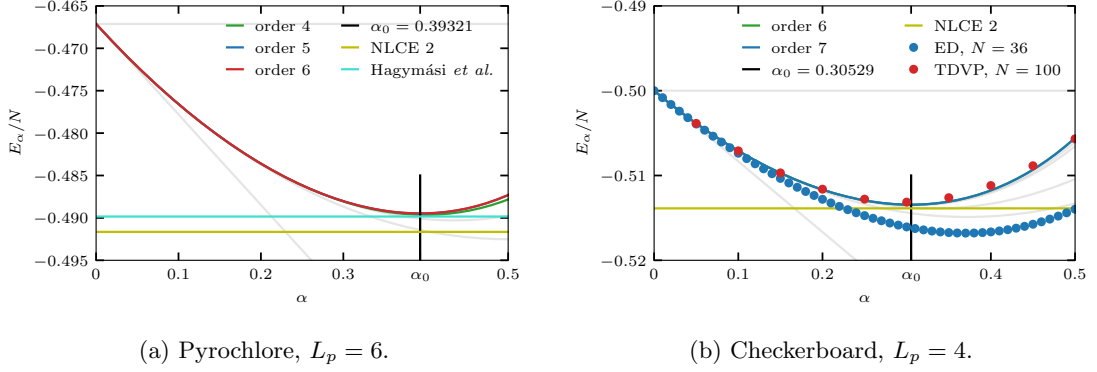


Figure 2.14: Variational energy E_α/N in the Heisenberg $S = 1/2$ model on the (a) pyrochlore and (b) checkerboard lattices. The plaquettes refer to a hard-hexagon (hard-square) decomposition in the pyrochlore (checkerboard). Both decompositions are shown in Figure 5.6. Gray lines indicate the convergence by displaying lower orders of expansion. In the pyrochlore, the sixth-order contribution of $\langle V_e \rangle_\alpha$ omitted the largest clusters containing six and seven hexagons for computational reasons; however, we do not expect any significant influence around the minimum. Both estimates are compared to second order NLCE at $T = 0$, cf. Section 5.3. The pyrochlore data is further compared to an estimate of the ground-state energy found in Section 5.1 [2]. The two-dimensional checkerboard lattice allows additional ED and TDVP calculations. ED ($N = 36$) is performed using the finite-temperature Lanczos method [111] revealing pronounced finite-size effects. In contrast, TDVP ($N = 100$) using a bond dimension $\chi = 2000$ agrees perfectly with the expansion [155, 105].

inter-plaquette bonds (E_{weak}) decrease, yielding a pronounced minimum at $\alpha_0 \in [0.2, 0.4]$. Next to the checkerboard composed of squares, the ansatz is applied to a fixed hard-hexagon tiling in the pyrochlore and the ruby lattice with additional frustrated couplings. The lattices are shown in Section 5.3. The expansion is carried out up to order six (seven) for the pyrochlore (checkerboard) and is fully converged around the minimum. Figure 2.14 reveals the good convergence and the pronounced minimum found for a hexagon (square) decomposition in the pyrochlore (checkerboard) lattice. Table 2.2 lists the lowest variational energy and optimal imaginary time α_0 . The individual coefficients for $\langle H_p \rangle_\alpha$ and $\langle V_e \rangle_\alpha$ are shown in Table 2.3.

As a consistency check, we implemented the imaginary-time evolution on the checkerboard lattice using the time-dependent variational principle (TDVP) with the ITensor package [155, 105] on a cluster with $N = 100$ sites with periodic boundary conditions yielding an excellent agreement. Finite-temperature Lanczos [111] on a cluster with $N = 36$ sites demonstrates a qualitative agreement for small α but suffers from finite-size effects, cf. Figure 2.14b.

In addition to the Bravais lattice, we considered generalized “Bethe” lattices where the reduced lattices correspond to the Bethe lattice with the coordination number $L_p = 4, 6, 8$ – a regular tree of degree L_p . A plaquette with circumference L_p replaces each vertex of the Bethe lattice, and each edge contains the quartet of doubly frustrated bonds. Hence, the resulting lattice does not contain periodic loops apart from the plaquettes. Despite the absence of the

periodic loops (of plaquettes), we observe the same physics indicating its robustness.

Strikingly, the doubly frustrated bonds induce very weakly coupled plaquettes such that the precise geometry and dimensionality of the problem have little impact. This can be observed in [Table 2.2](#) and [Table 2.3](#), where coefficients for a fixed plaquette length are nearly identical regardless of the underlying lattice. Differences occurring at higher order n , induced from the different topology of the lattices, are suppressed by α_0^n . Crucially, the plaquette ground state is even robust if closed loops (of plaquettes) are present. However, we expect the breakdown of the valence-bond crystal for larger plaquette lengths for two reasons. First, the energy per site for larger circumferences is reduced, and second, more bonds are attached to the plaquette, making them more important.

The approach produces a robust dressing yielding competitive ground-state energies for all models considered. Most importantly, the approach does not suffer from finite-size effects and is fully converged, providing an upper bound on the ground-state energy. Also, it can be extended to other models and arbitrarily decoupled motifs, such as various dimer coverings frequently proposed for frustrated magnets. Additionally, multiple variational parameters can be introduced by acting on different bonds. Besides the ability to dress ground states, the ansatz might be a suitable description for dressed plaquette excitations – when the kinetic energy of excitations is suppressed. The results and the consequences of the expansion are discussed in detail [Section 5.3](#).

coefficients of $E_{\text{strong}} = \langle H_p \rangle_\alpha / L_p$

Model \ Order	0	1	2	3	4	5	6	7
Checkerboard, $S = 1/2$	-0.50000	0.00000	0.16667	-0.08333	0.18461	-0.11343	0.10520	-0.05644
Bethe ($L_p = 4$), $S = 1/2$	-0.50000	0.00000	0.16667	-0.08333	0.18461	-0.11343	0.10376	-0.05440
Checkerboard, $S = 1$	-1.50000	0.00000	1.00000	-0.50000	3.02500	-2.34290	8.45032	–
Bethe ($L_p = 4$), $S = 1$	-1.50000	0.00000	1.00000	-0.50000	3.02500	-2.34290	8.41575	–
Pyrochlore, $S = 1/2$	-0.46713	0.00000	0.17618	-0.08809	0.14804	-0.08124	0.03410	–
Ruby, $S = 1/2$	-0.46713	0.00000	0.17618	-0.08809	0.14561	-0.08292	0.01199	–
Bethe ($L_p = 6$), $S = 1/2$	-0.46713	0.00000	0.17618	-0.08809	0.14699	-0.07885	0.02905	–
Pyrochlore, $S = 1$	-1.43624	0.00000	1.07960	-0.53980	2.71700	–	–	–
Ruby, $S = 1$	-1.43624	0.00000	1.07960	-0.53980	2.69478	–	–	–
Bethe ($L_p = 6$), $S = 1$	-1.43624	0.00000	1.07960	-0.53980	2.69158	–	–	–
Bethe ($L_p = 8$), $S = 1/2$	-0.45639	0.00000	0.17867	-0.08933	0.13663	–	–	–
Bethe ($L_p = 8$), $S = 1$	-1.41712	0.00000	1.10135	-0.55067	–	–	–	–

coefficients of $E_{\text{weak}} = \langle V_e \rangle_\alpha / 4$

Model \ Order	0	1	2	3	4	5	6	7
Checkerboard, $S = 1/2$	0.00000	0.04167	-0.02083	0.05324	-0.03819	0.04884	-0.03658	0.03050
Bethe ($L_p = 4$), $S = 1/2$	0.00000	0.04167	-0.02083	0.05324	-0.03819	0.04853	-0.03609	0.02622
Checkerboard, $S = 1$	0.00000	0.16667	-0.08333	0.51111	-0.44753	1.68815	-1.87512*	–
Bethe ($L_p = 4$), $S = 1$	0.00000	0.16667	-0.08333	0.51111	-0.44753	1.68321	-1.86689	–
Pyrochlore, $S = 1/2$	0.00000	0.05334	-0.02667	0.05507	-0.03644	0.03260	-0.01600*	–
Ruby, $S = 1/2$	0.00000	0.05334	-0.02667	0.05461	-0.03767	0.02707	-0.01267	–
Bethe ($L_p = 6$), $S = 1/2$	0.00000	0.05334	-0.02667	0.05507	-0.03656	0.03265	-0.01683	–
Pyrochlore, $S = 1$	0.00000	0.21189	-0.10594	0.54542	-0.47087*	–	–	–
Ruby, $S = 1$	0.00000	0.21189	-0.10594	0.54611	-0.47811*	–	–	–
Bethe ($L_p = 6$), $S = 1$	0.00000	0.21189	-0.10594	0.54541	-0.47054	–	–	–
Bethe ($L_p = 8$), $S = 1/2$	0.00000	0.05747	-0.02874	0.05479	-0.03510	–	–	–
Bethe ($L_p = 8$), $S = 1$	0.00000	0.22650	-0.11325	0.54815	–	–	–	–

Table 2.3: Coefficients describing the energy contribution of the two different bonds derived using the linked cluster theorem in powers of α for different lattices and spin lengths ($J = 1$). Each site is associated with one strong and two weak bonds yielding a final energy of $E_\alpha/N = \sum_k E_{\text{strong}}(k)(-\alpha)^k + 2 \sum_k E_{\text{weak}}(k)(-\alpha)^k$. Some calculations, marked with an asterisk, omitted the contributions of the largest clusters for E_{weak} – (model; order; number of plaquettes): (checkerboard, $S = 1$; 6, 6 & 7), (pyrochlore, $S = 1/2$; 6; 6 & 7), (pyrochlore, $S = 1$; 4; 4 & 5), (ruby, $S = 1/2$; 6; 6 & 7), (ruby, $S = 1$; 4; 4 & 5).

Part II

THE ARCHETYPE OF FRUSTRATED MAGNETISM

Chapter 3

THE PYROCHLORE HEISENBERG ANTIFERROMAGNET ...

If possible, antiferromagnets favor an anti-alignment of spins: the Néel state. A lattice is geometrically frustrated if it fails to host a simple Néel order and, therefore, fails to minimize all exchange interactions simultaneously [26, 27, 23, 156, 157, 25]. In the classical limit, many geometrically frustrated magnets have an extensive manifold of degenerate ground states and will remain disordered but strongly correlated, even at zero temperature. While quantum fluctuations are expected to lift the degeneracy, they often do so only weakly, leaving many competing low-energy states. Moreover, the states formed in the presence of quantum fluctuations are often of exotic nature, including both unconventionally ordered states and disordered quantum spin liquids (QSLs). Therefore, geometrically frustrated magnets provide a fertile ground to realize intriguing novel phases, making it a promising target to study. Despite the fascinating properties of frustrated magnets and decades of intense research, many questions remain unanswered due to a lack of controlled and unbiased methods [158].

Among all frustrated materials, the pyrochlore antiferromagnet is probably the most celebrated example in three dimensions. This archetype is a promising candidate to realize QSL or other exotic magnetic states in nature [21, 159]. It consists of a network of corner-sharing geometrically frustrated tetrahedra as illustrated in Figure 3.1. In the classical Heisenberg model on the pyrochlore lattice, pioneering work was performed by Jacques Villian [23], yielding a classical spin liquid [25] with an emergent gauge field exhibiting a Coulomb phase [160, 161, 162]. Equally exciting are the Ising spins [163, 164, 165, 166]. Famously, Philip W. Anderson [27] noticed - based on Linus C. Pauling's estimate for water ice [167] - its exponentially large degeneracy and, hence, extensive residual entropy. Allowing quantum tunneling between the degenerate states leads to the formation of quantum spin ice and its emergent low-energy gauge theory [168, 169]. Despite the tremendous efforts aiming at a deeper understanding of these exotic phenomena, it withstands analytical and numerical attempts in the quantum realm, making it a long-standing problem of quantum magnetism. The nature of the ground state and even finite-temperature properties of the pyrochlore Heisenberg antiferromagnet are mostly unknown in the quantum

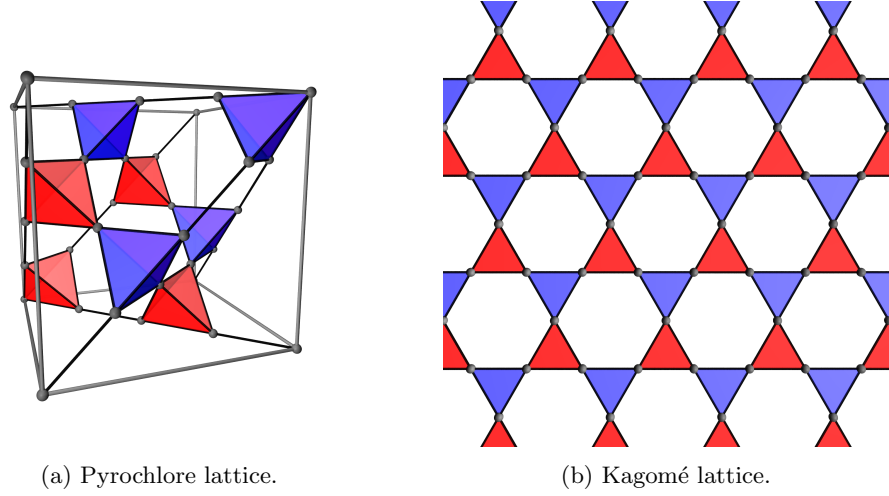


Figure 3.1: Pyrochlore (Kagomé) lattice consisting of corner-sharing tetrahedra (triangles). The underlying crystal structure is a face-centered cubic lattice described by the lattice vectors $\mathbf{a}_1 = (1, 1, 0)^T$, $\mathbf{a}_2 = (1, 0, 1)^T$, $\mathbf{a}_3 = (0, 1, 1)^T$ for the pyrochlore and a triangular lattice described by the lattice vectors $\mathbf{a}_1 = (1, 0)^T$, $\mathbf{a}_2 = (0.5, \sqrt{3}/2)^T$ for the kagomé lattice. The basis vector of the tetrahedral (triangular) unit cell are given $\mathbf{b}_0 = \mathbf{0}$ and $\mathbf{b}_i = \frac{1}{2}\mathbf{a}_i$.

case. Hence, due to its complexity and lack of applicable methods, many questions about pyrochlore and its two-dimensional cousin, the kagomé, remain unanswered. Both lattices are shown in Figure 3.1.

This chapter introduces essential aspects of frustration by referring to the pyrochlore antiferromagnet. It starts with a brief overview of spin liquids and presents some ideas on where to find them. The second section introduces quantum spin ice as it provides important insights into the physics of pyrochlore magnetism. Experimental candidates to realize spin liquids on the pyrochlore lattice include the dipolar-octupolar pyrochlores $\text{R}_2\text{M}_2\text{O}_7$ (*e.g.* $\text{R}=\text{Ce}, \text{Nd}, \text{Sm}$; $\text{M}=\text{Zr}, \text{Sn}, \text{Hf}$) [21, 22, 170]. The third section presents some background on these materials, and Section 4.3 discusses experiments on $\text{Ce}_2\text{Sn}_2\text{O}_7$ and $\text{Ce}_2\text{Zr}_2\text{O}_7$ [3].

3.1 Spin liquids

There are disordered phases beyond a trivial paramagnet: *spin liquids* [171, 172, 173, 174]. While a transition into a magnetically ordered phase is accompanied by an order parameter, a liquid phase does not exhibit any conventional order [175, 173] even at low temperature.

This raises the question of how one could characterize such a state? Phase transitions are driven by temperature and indicated by a qualitative change of the equilibrium state. As a system seeks to minimize its free energy, the competition between energy and entropy is controlled by temperature. At infinite temperatures, the system simply maximizes the entropy without regard to energy. This produces a uniform distribution of states and results into a featureless paramagnetic state. The paramagnetic state usually extends into a high but finite-temperature regime and slowly builds up correlations as energetically lower states are favored. Lowering the temperature further introduces stronger correlations, yielding multiple possible scenarios.

Most materials exhibit a finite-temperature transition into an ordered state characterized by an order parameter that spontaneously breaks the symmetries of the Hamiltonian. This scenario is realized in simple ferromagnetic materials such as magnetite and antiferromagnets, which are not *geometrically frustrated*. Note that some antiferromagnets order despite their frustration, *e.g.* on the triangular lattice. Transitions into an ordered state are typically accompanied by peaks in the specific heat, cusps in the susceptibility, and the development of Bragg peaks in neutron scattering.

The other possibility is conceptually more interesting. Some systems do not show signs of (conventional) order down to low or even zero temperature. In generic models, the energetic part in the free energy dominates at low temperatures making the state strongly correlated yet remaining disordered. Historically, these states are classified as liquids due to their absence of order. However, a naive negative definition¹ – *A strongly correlated, but disordered state* – only focusing on the absence of order would include somehow trivial models like the Shasty-Sutherland model [177] or a Heisenberg model on the ruby lattice, *cf.* Section 5.3 [6]. However, the sometimes exotic phenomena and properties of QSLs exceed the naive negative definition and go far beyond. Besides the absence of order, a common feature is the presence of elementary *non-local* and *fractionalized* excitations that local operators cannot generate. The associated quasiparticles can show some form of long-range interaction, such as an effective Coulomb interaction [165]. A modern QSL definition is based on an effective low-energy gauge theory emerging from local constraints [178]. However, formulating a clear positive definition of QSLs or even classical spin liquids has posed a challenge for theorists over the past decades. Different types of spin liquids are classified by their low-energy excitations, the entanglement structure, as well as the emergent gauge field in the low energy limit: $U(1)$ [168, 179, 180, 181], \mathbb{Z}_2 [70, 69, 182], *chiral* [183, 184], *nematic* [185, 135], and many more [171, 186, 187, 188].

¹“*You do not define a thing in terms what it is not!*” from Eugene John Mele [176] who referred to the statement that “*An insulator is not a conductor*” even though it is intuitive and simple.

Many insights we have today are obtained from exactly solvable but fine-tuned models [189], which allow a deep understanding of their internal structure and, more importantly, their excitations. Two of the most famous models, introduced by Alexei Kitaev, are the toric code model [70] and the Kitaev model on the honeycomb lattice [69]. Both are \mathbb{Z}_2 QSL exhibiting exotic physical properties like anyonic and fermionic quasi-particles, topological entanglement, complex fusion rules, and topological order. While a full introduction into the rapidly developing field of spin liquids is beyond the scope of this work, many detailed reviews are available in the literature: [190, 191, 192, 173, 193, 158, 194, 178, 33]

Generally, low coordination number, small spin S , and competing interactions amplify quantum fluctuation, such that spontaneous symmetry breaking can be suppressed, even down to zero temperature. Despite the enormous number of QSL candidate materials, the endeavor to realize a QSL in nature is notoriously difficult and faces several obstacles. First, materials suffer from different types of disorder, that makes it hard to distinguish the supposed signatures of a QSL. Crucially, the actual experiment already starts with crystal growth which is highly delicate and strongly depends on the applied synthesis technique. The quality of the sample² might induce fundamentally different phases. Second, the exchange energy scale of many quantum materials is often small, and, therefore, experiments require extremely low temperatures. Finally, the theoretical hallmarks of QSLs, such as fractionalized excitations and emergent gauge fields, are notoriously hard to detect in experiments as their signals are disturbed by other sources. Identifying ordered states of matter is much simpler as they exhibit pronounced features like Bragg peaks or thermodynamic anomalies. Therefore, combining the effects of disorder, the relevant temperature scale, and the complex theoretical description makes a definite experimental verification challenging [178]. Many experiments claim to realize a QSL at low temperatures due to the absence of order; however, providing evidence is tricky.

²As Wolfgang E. Pauli said "*Festkörperphysik ist eine Schmutzphysik*" [195].

3.2 Quantum spin ice

Frustrated materials are prime candidates to host such exotic states [158, 178]. Strikingly, the pyrochlore allows a perturbative treatment around its classical Ising limit, revealing a QSL when additional quantum fluctuations enter the stage. This section summarizes the fascinating phenomena emerging from the QSL description, known as *quantum spin ice* (QSI). The theory of QSI emerges from *classical spin ice* (CSI) [163, 196, 164], which exhibits an extensive ground-state manifold [167, 27]. Quantum fluctuations on top of the spin ice manifold yield a compact $U(1)$ lattice gauge theory in the low-energy limit. The gauge theory is a lattice analog of quantum electrodynamics and gives rise to deconfined magnetic and electric charges and gapless photonic excitations. We follow Ref. [168, 33, 197, 82] for the rest of the section.

The nearest-neighbor Ising model on the pyrochlore is simply given (up to a constant c) by the square of the cluster spin L_t^z , which is defined for each tetrahedron t :

$$H_{\text{CSI}} = J \sum_{\langle i,j \rangle} S_i^z \cdot S_j^z = J \sum_t (L_t^z)^2 + c \quad \text{with} \quad L_t^z = S_{t_1}^z + S_{t_2}^z + S_{t_3}^z + S_{t_4}^z \quad (3.1)$$

where t_i denote the individual site participating in the tetrahedron t . The cluster spin L_t^z has to vanish to minimize the energy. A simple counting argument for classical spins reveals a macroscopic ground-state degeneracy [23, 25].

Classical spin ice What is the connection between magnetic spins and (water) ice? The classical antiferromagnetic Ising ground states share the same physical properties as water ice which fulfills the famous “ice rule”. When water freezes, it arranges according to the *two-near-two-far* rule, yielding a non-vanishing residual entropy as first estimated by Linus C. Pauling [167, 198]. The oxygen atoms form a diamond lattice, and hydrogen atoms are placed on the links between adjacent oxygen atoms. At low temperatures, the lattice arranges such that two hydrogen atoms are near to one oxygen, and two are far [199, 167, 200, 201, 170].

The low-energy (water) ice states are equivalent to low-energy states of Ising spins in the pyrochlore. The tetrahedra of the pyrochlore form a diamond lattice, and the spins represent the links between two tetrahedra. In spin ice, magnetic moments exhibit an easy axis \mathbf{z}_i pointing *in* or *out* of a tetrahedron with a magnetic moment proportional to $S_i^z \mathbf{z}_i$. Ferromagnetic interactions between two neighboring spins induce an effective antiferromagnetic Ising model due to the spatial orientation of the respective easy axis: $\mathbf{S}_i \cdot \mathbf{S}_j = S_i^z S_j^z \mathbf{z}_i \cdot \mathbf{z}_j = -\frac{1}{3} S_i^z S_j^z$. Summing up the total spin of the tetrahedron and demanding it to be zero yields an equivalent rule: two spins have to point (locally) up, and two spins point (locally) down. By pointing up and down, the Ising spins are identified as the hydrogen atoms located near or far from an oxygen atom. Therefore, the low-energy states of spin ice follow an equivalent rule: *two-in-two-out*.

The extensive spin ice manifold yields a finite residual entropy. Based on Pauling’s estimate for water ice [167], Anderson introduced a first approximation of the residual entropy in CSI,

which reflects the number of possible ground-state configurations.

$$\frac{S_{T=0}}{N} = \log \sqrt{\frac{3}{2}} \quad (3.2)$$

This rather crude approximation assumes uncorrelated tetrahedra, but it gives a reasonable estimate of the residual entropy up to a few percentages in water ice [202] and CSI [203, 131]. The enormous number of ground-state configurations is already observed for a single tetrahedron, where six out of sixteen configurations minimize the energy.

One prominent characteristic feature of spin ice, a direct consequence of the emergent gauge theory, is the presence of pinch-points [168, 160, 204, 205, 206]. Pinch points are singularities in the Fourier transform of the spin correlator and are induced by the divergenceless field. Importantly, they can and are observed in experiments. For example, spin diffuse scattering measurements on $\text{Ho}_2\text{Ti}_2\text{O}_7$ display pronounced pinch-points reflecting a classical Coulomb phase at low temperature [207, 3].

Besides the extensive manifold and its consequences, another fascinating phenomenon is the presence of fractionalized excitations in the form of magnetic monopoles [208, 165]. Violating the ice rule by flipping a single spin induces two defects such that the neighboring tetrahedra exhibit a cluster spin of $L_t = \pm 1$, respectively. These defects are deconfined; they can be separated from one another to an infinite distance without an additional energy cost. The tetrahedra can be viewed as sources and sinks of a magnet field as both are connected via strings of flipped spins. Many rare-earth pyrochlores exhibit essential long-range dipole-dipole interactions [209, 210, 211, 212, 165, 170, 33] inducing an effective Coulomb interaction between these monopoles [165, 166].

Quantum spin ice Quantum effects permit transitions between different ice configurations without any thermal activation. Additional weak transverse (non-Ising) terms lift the spin ice degeneracy and introduce a variety of exotic phenomena: gapless *photonic* excitation, gapped *electric* gauge charge and gapped *magnetic* gauge charges [168, 33]. The simplest approach to QSI includes additional weak transverse coupling J_{xy} :

$$H_{\text{QSI}} = H_{\text{CSI}} + H_{xy} = J_z \sum_{t \in \mathcal{T}} (L_t^z)^2 + \frac{J_{xy}}{2} \sum_{\langle i, j \rangle} (S_i^+ S_j^- + \text{h.c.}) \quad (3.3)$$

In the limit of strong anisotropy, $J_z \gg |J_{xy}|$, quantum fluctuations are perturbatively included and break the spin ice's classical degeneracy. Quantum effects could induce order into the system by choosing a specific ice configuration or generate a massive superposition of various ice states. The effective Hamiltonian is derived within the framework of degenerate perturbation theory [213]. The first non-trivial off-diagonal contribution preserving the ice rule is the *ring ex-*

change term³. Therefore, the effective Hamiltonian (up to a constant) in third-order perturbation theory can be written as:

$$H_{\square} = \underbrace{\frac{3J_{xy}^3}{2J_z^2}}_{=g} \sum_{\square} \left(S_{\square_0}^+ S_{\square_1}^- S_{\square_2}^+ S_{\square_3}^- S_{\square_4}^+ S_{\square_5}^- + \text{h.c.} \right) \quad (3.4)$$

The sum runs over all hexagons in the pyrochlore lattice, and \square_i refers to the i th site of the hexagon. The compact lattice $U(1)$ gauge theory is obtained by softening the spin-1/2 restriction using *twisted rotors*:

$$S_j^z \rightarrow E_j \text{ and } S_j^{\pm} \rightarrow e^{\pm i A_j} \quad (3.5)$$

We impose the canonical commutation relation between both variables A_k and E_j : $[A_k, E_j] = \delta_{kj} i$

Then, $e^{\pm i A_j}$ acts as the usual raising and lowering operators by the cost of enlarging the physical spin-1/2 Hilbert space. An additional term controlled by U is introduced artificially to restrict the enlarged (non-physical) space:

$$H_{\text{QSI}} = g \sum_{\square} \cos(\text{curl}(A)_{\square}) + U \sum_i \left(E_i^2 - \frac{1}{4} \right) \quad (3.6)$$

The effective ring exchange term in Equation 3.4 causes $\text{curl}(A)_{\square} = A_{\square_0} - A_{\square_1} + A_{\square_2} - A_{\square_3} + A_{\square_4} - A_{\square_5}$ and describes the magnetic flux going through a hexagon. The derived Hamiltonian is a compact (A_i is defined up to 2π) and “lattice version” of quantum electrodynamics. Although it looks somewhat artificial, it is a valid description of QSI Hamiltonian – in the limit of $U \rightarrow \infty$ and $J_z \gg |J_{xy}|$. However, it has been shown that low-energy physics extends to a finite value of U , which allows for relaxing the constraint $U \rightarrow \infty$ [214, 168, 215, 216, 217].

The system enters different phases depending on the ratio between g and U . If E_i were integer variables, then there would be two different phases, depending on the ratio: confined phases for $U/g \gg 1$ and a deconfined Coulomb phase for $U/g \ll 1$. However, since E_i is a half-integer, the E_i^2 term is minimized by either $E_i = \pm 1/2$ and is therefore frustrated. This enables the deconfined phase to exist up to finite values of U [217]. In the deconfined phase, fluctuations of A are small, and one can expand the cosine to yield the standard quadratic Hamiltonian of electrodynamics (on a lattice):

$$H_{\text{EM}} = g' \sum_{\square} \text{curl}(A)_{\square}^2 + U \sum_i E_i^2 \quad (3.7)$$

³While the first order contribution vanishes trivially as it violates the ice rule, the second order enters as a constant energy shift by including *forth and back* hopping on a single bond. Besides a diagonal term caused by hoppings on a triangular surface in the third order, hexagonal loops induce the first non-vanishing off-diagonal terms.

The gapless excitations of this model are similar to photons in the case of electrodynamics in the vacuum. These “pyrochlore-photons” exhibit a linear dispersion at small momentum allowing the extraction of the fine structure constant [108]. They are also responsible for the T^3 -scaling of the heat capacity at low temperatures. In addition to photonic excitation, the gauge theory supports electric and magnetic charges. While the electric charges have a characteristic energy scale of J_z , the magnetic charges⁴ and photons exhibit an energy scale of $|J_{xy}| \ll J_z$. The ground-state wavefunction in the Coulomb phase exhibits a massive superposition in any local basis [168, 169, 134, 194, 197, 218].

If quantum fluctuations are small, $|J_{xy}| \ll J_z$, it is expected that the low-energy limit is described by $U(1)$ gauge theory with distinct fluxes: 0-flux in the ferromagnet ($J_{xy} < 0$) and π -flux in the antiferromagnet ($J_{xy} > 0$) case. The coupling constant g in Equation 3.6 changes sign for both cases; hence, the energy is minimized by $\cos(\text{curl}(A)_\square) = +1$ [0-flux] and $\cos(\text{curl}(A)_\square) = -1$ [π -flux], respectively.

However, the arguments above are perturbative, and their validity beyond a small perturbation is questionable. Luckily, ferromagnet transverse couplings, $J_{xy} < 0$, allow sign-free QMC simulations. Indeed, it reveals that the Coulomb QSL regime extends into a finite regime, $|J_{xy}|/J_z \lesssim 0.1$, before making way for a XY -ordered ferromagnet [215, 76, 77]. In contrast, frustrated transverse couplings, $J_{xy} > 0$, induce the infamous sign problem, which prohibits QMC approaches. Combining cluster mean-field theory, variational arguments, and exact diagonalization allows the estimation of possible phases for the fully frustrated model [219, 220]. However, due to its complexity and lack of controlled methods, the pyrochlore antiferromagnet withstands a definite understanding, as indicated by the vast number of proposals. Therefore, this thesis tries to shed light on whether the disordered spin liquid regime [221, 222, 223, 224, 185, 135] extends to non-perturbative parameters or gives way to an ordered state [225, 226, 227, 228, 229, 230, 231, 232, 233, 234, 95]. Chapter 5 presents extensive numerical [2, 4] and recent analytical [6] arguments supporting a spontaneous symmetry breaking at the isotropic Heisenberg point $J_{xy} = J_z$.

⁴Note that the electric charges emerging in QSI refer to the magnetic monopoles of CSI.

3.3 Materials

The pyrochlore is the most promising candidate to realize a three-dimensional QSL in nature. It exhibits a well-established and well-understood low-energy theory supporting gapped and gapless excitations around the Ising limit. A prominent class of materials revealing QSI physics are the rare-earth pyrochlore magnets. The family comprises a trivalent 4f rare-earth ion R and a non-magnetic tetravalent transition metal ion M : $R_2M_2O_7$. This section briefly presents the essential mechanisms responsible for the microscopic Hamiltonian description. More details and further literature can be found in Ref. [21, 22, 170].

Famously, the dipolar exchange interaction in $Dy_2Ti_2O_7$ [235] and $Ho_2Ti_2O_7$ [163, 207, 236] yields a CSI limit [237] exhibiting the residual Pauling entropy at low temperatures⁵ [238, 235]. If one replaces the rare-earth component R with other materials, quantum fluctuations enter the stage and induce a wealth of exotic phenomena with competing exchange interactions [217, 239]. Prominent chemical elements for the trivalent ion are $R \in \{\text{Pr, Tb, Er, Yb, Ce, Nd}\}$ and for the tetravalent ion are $M \in \{\text{Hf, Pt, Sn, Ti, Zr, Sn}\}$. It yields a series of fascinating phenomena, including exotically ordered, classical and quantum spin ice, spin glass freezing, and order-by-disorder effects [21].

Although the CSI Hamiltonian [Equation 3.1] on the pyrochlore lattice looks somewhat artificial, there are materials (approximately) realizing this model. Their existence in nature is motivated by fundamental microscopic mechanisms acting at well-separated energy scales. The magnetism arises from unpaired well-localized 4f electrons in the rare-earth ions. The effective microscopic model is based on a hierarchy of energy scales in the material. Most importantly, single-ion physics dominates over two-ion exchanges. The following applies to the rare-earth ions:

$$\text{Coulomb interaction} > \text{spin-orbit coupling} > \text{electric crystal field}$$

First, despite the heavy ion, the atomic orbitals are categorized according to four quantum numbers: n , l , m_l and m_s . Equivalent to states of the hydrogen atom, the principle number n refers to the shell, l to the angular momentum, m_l is the magnetic quantum number, and m_s is the spin of the electron. Second, spin-orbit couplings allow Hund's rules to determine the lowest energy configurations and to define a total angular momentum J composed of the angular momentum and the electron spin [18]. Kramers (non-Kramers) ion exhibit an odd (even) number of 4f electrons yielding a half-integer (integer) total angular momentum J . Third, the crystal field, generated by the surrounding oxygen atoms, lifts the $2J + 1$ degeneracy induced by Hund's rules. This yields a low-energy doublet which is effectively described by pseudospin operators with $S = 1/2$. For Ce^{3+} , a Kramers ion, the doublet exhibits a total angular momentum of $J = 5/2$ and magnetization of $m_j = \pm 3/2$. Generally, the surrounding crystal field determines

⁵A residual entropy at zero temperature violates the third law of thermodynamics. In water ice, further cooling induces lattice distortion, realizing Pauling's entropy [167]. In the pyrochlore case, the system falls out of equilibrium or magnetic order induced by interactions beyond the nearest-neighbor become important at lower temperatures.

the size of the effective moment, its anisotropy, and allowed exchange terms.

The low-energy doublet exhibits a relatively large gap (~ 100 K). In particular, it is much larger than exchange interactions between neighboring ions allowing an effective pseudospin-1/2 description at sufficiently low temperatures. Depending on the symmetry properties of the doublet, the pseudospin-1/2 operator can transform in different ways under the symmetries. This constrains different nearest-neighbor exchange interactions, of which the dipolar-octupolar Hamiltonian is one case [240, 241, 242, 22]:

$$H_{\text{DO}} = \sum_{\langle i,j \rangle} [J_x S_i^x S_j^x + J_y S_i^y S_j^y + J_z S_i^z S_j^z] - g_z \mu_B \sum_i \mathbf{h} \cdot \mathbf{z}_i (S_i^z \cos \theta + S_i^x \sin \theta) \quad (3.8)$$

The spin operators refer to the local frames of the pseudospins [243, 244]. Two transform as a dipole (x and z), and one transforms as an octupole (y) under lattice and time-reversal symmetry. Note that an external magnetic field acts differently on each site of the tetrahedron as the local \mathbf{z}_i -axis differs. In particular, the Hamiltonian applies to Cerium-based (Ce^{3+}) pyrochlore oxides, Kramers ions with a single 4f electron, which is discussed in Section 4.3. The g -factor g_z can be calculated from the crystal electric field wavefunctions or fitted from experiments [245, 246, 247]. μ_B is the Bohr magneton.

Besides the rare-earth pyrochlores, other materials exhibit a pyrochlore structure like ZnCr_2O_4 , $\text{NaCaNi}_2\text{F}_7$, or spinel compounds [248, 249]. ZnCr_2O_4 and $\text{NaCaNi}_2\text{F}_7$ realize an isotropic Heisenberg antiferromagnet with spin-3/2 and spin-1, respectively. While the $S = 3/2$ compound shows a finite-temperature ordering transition [250, 230, 251], the $S = 1$ compound does not [252, 253, 254]. Besides isotropic antiferromagnets, some materials, like $\text{CuInCr}_4\text{S}_8$ [255], exhibit a breathing anisotropy where the interaction strength on one type of tetrahedra is dominant.

While experiments turned out to be challenging, much progress was made during the past years. Even though we still lack an (isotropic) pyrochlore $S = 1/2$ Heisenberg material (studied in Section 4.2 and Chapter 5), promising QSL candidates are available today. Section 4.3 provides a details analysis of experiments on $\text{Ce}_2\text{Sn}_2\text{O}_7$ and $\text{Ce}_2\text{Zr}_2\text{O}_7$ [3], demonstrating the diversity and complexity in frustrated magnets.

Chapter 4

... AT FINITE TEMPERATURE

Ferromagnetic transverse couplings enable sign-problem free QMC simulations providing deep insights into the thermodynamic properties in the pyrochlore model and revealing the wealth of magnetic phases associated with frustration in three dimensions [76, 77]. However, due to the lack of controlled methods, the fully frustrated Heisenberg model with antiferromagnetic transverse couplings remains inaccessible and continues to pose a challenging problem – even at finite temperatures. This chapter aims at a better understanding of the thermodynamics in the pyrochlore antiferromagnet using state-of-the-art numerics. In particular, the combination of NLCE with graph- and group-theoretic approaches to maximize the benefits of symmetries provides reliable and unbiased results in the thermodynamic limit without any parameter restriction.

The first section presents a brief introduction into thermodynamics in quantum systems and the important observables accessible in both numerical simulations and experiments. The second section focuses on the isotropic Heisenberg model. Pushing NLCE up to the eighth order in a tetrahedron-based demonstrates its capabilities by reaching non-trivial temperatures up to $T_{\text{conv}} = 0.25 J$ [1]. The broad applicability of the algorithm allows for its application beyond the $SU(2)$ -symmetric model. Section three presents a systematic analysis of experimental data obtained for the dipolar-octupolar pyrochlores $\text{Ce}_2\text{Sn}_2\text{O}_7$ and $\text{Ce}_2\text{Zr}_2\text{O}_7$ [3]. Extensive NLCE calculations provide constraints on the microscopic exchange parameters of both materials. Despite a comparable chemical structure, both materials display significant differences. As the applied methodology is similar for both materials, they are discussed side by side.

4.1 Thermodynamics in spin systems

This section provides a brief overview of thermodynamics in spin systems and introduces frequently evaluated observables. An ab initio full microscopic description of an interacting system is hopeless, even within the framework of classical mechanics. Instead, thermodynamics describes the equilibrium state with a few macroscopic variables like volume V , pressure p , entropy S , temperature T , chemical potential μ , or particle number N . The concept of thermodynamics is one of the oldest and most well-established theories in physics and is reviewed in great detail in many textbooks [79, 256]. The equilibrium state of a system is defined as the extrema of thermodynamic potentials. The most commonly used potentials are internal energy, enthalpy, grand canonical potential, or free energy.

A quantum spin systems exhibit an exponentially large but discrete energy spectrum: $E_1 \leq \dots \leq E_D$. The full state of a system with N spins is expressed in the form of a density matrix $\rho \in \mathbb{C}^{2^N \times 2^N}$ for $S = 1/2$. The Gibbs canonical density matrix ρ_β defines the equilibrium quantum state for the inverse temperature¹ $\beta = 1/k_B T$:

$$\rho_\beta = e^{-\beta H} = \sum_{i=1}^D e^{-\beta E_i} |\Psi_i\rangle \langle \Psi_i| \quad (4.1)$$

E_i is the spectrum of H and $|\Psi_i\rangle$ is the referring eigenstate. The partition sum Z and the thermal expectation value $\langle O \rangle_\beta$ of an operator O are defined by the trace over the density matrix ρ_β :

$$Z = \text{Tr}(\rho_\beta) = \sum_{i=1}^D e^{-\beta E_i} \quad (4.2)$$

$$\langle O \rangle_\beta = \text{Tr}(O \rho_\beta) / Z = \sum_{i=1}^D e^{-\beta E_i} \langle \Psi_i | O | \Psi_i \rangle / Z \quad (4.3)$$

Referring to [Section 2.1](#), the partition sum and expectation value can be computed in any basis despite a possible block structure of the Hamiltonian. Evaluating the partition sum analytically for interacting models is extremely challenging and only succeeds in special cases like the Ising model [257, 258]. The partition sum defines the free energy of the model

$$F = -\frac{1}{\beta} \log Z = \langle H \rangle_\beta - \frac{1}{\beta} S, \quad (4.4)$$

which is minimized by the equilibrium state. $\langle H \rangle_\beta$ is the internal energy at β , and S is the entropy. The energy-entropy competition of macroscopically different states to minimize the free energy is responsible for phase transitions.

¹ $k_B \approx 8.3 \text{ JK}^{-1} \text{ mol}^{-1}$ is the Boltzmann constant and relates energy of the system to its temperature. If not stated differently, we will set $k_B = 1$ throughout this thesis.

Heat capacity Being experimentally accessible down to low temperatures and well-defined in numerical simulations, the heat capacity becomes an important quantity when we want to understand the physics within real materials. It defines the amount of heat necessary to raise the temperature by a predefined value of the sample. The simplest way to extract the heat capacity in numerical simulations is to determine the variance of the energy, as frequently done in QMC simulations. It only depends on the spectrum of the Hamiltonian:

$$C = \frac{\partial \langle H \rangle_\beta}{\partial T} = \beta^2 (\langle H^2 \rangle_\beta - \langle H \rangle_\beta^2) = \beta^2 \left(\frac{\sum_i E_i^2 e^{-\beta E_i}}{\sum_i e^{-\beta E_i}} - \left[\frac{\sum_i E_i e^{-\beta E_i}}{\sum_i e^{-\beta E_i}} \right]^2 \right) \quad (4.5)$$

At infinite temperate, the equilibrium state minimizes the free energy by maximizing the entropy. All energy levels are evenly populated, neglecting the energetic contribution. As the temperature is lowered, the spectral weight of low energy states increases, yielding a release in entropy. This entropy release induces a broad peak in the heat capacity known as the Schottky anomaly.

The heat capacity identifies a phase transition from a paramagnetic phase into an ordered phase in temperature by a sharp peak due to the discontinuity in some thermodynamic potentials. The low-temperature limit depends on the microscopic details of the system. While the heat capacity decreases exponentially with gap size for $T \rightarrow 0$ for gapped systems, gapless modes induce a power law decay. Hence, precise measurements at low temperatures provide insight into the microscopic excitations of the system. Important for this thesis, the photonic excitation in the pyrochlore induces a T^3 -decay for $T \rightarrow 0$ [168].

Entropy The thermodynamic entropy is closely related to the heat capacity and measures the “amount” of populated states at a specific temperature. It can be directly extracted from the partition sum

$$S = \log(Z) + \beta \langle H \rangle_\beta = \sum_i e^{-\beta E_i} + \beta \sum_i E_i e^{-\beta E_i}, \quad (4.6)$$

or from the heat capacity

$$S(T_2) - S(T_1) = \int_{T_1}^{T_2} dT \frac{C}{T}, \quad (4.7)$$

where one integration constant, $S(T_1)$ or $S(T_2)$, has to be fixed. At $T = \infty$ ($\beta = 0$), the entropy is equal to the logarithm of possible states, which is $\log(D) = \log((2S+1)^N) = N \log(2S+1)$ in the case of N spin- S . In the other limit, $T = 0$ ($\beta = \infty$), the residual entropy has to vanish according to the third law of thermodynamics – for generic systems. CSI is a famous counter examples exhibiting a finite residual entropy $S(0) \approx \log\left(\sqrt{\frac{3}{2}}\right)$ [167]. Similarly, Ising spins the on triangular lattice exhibit a finite residual entropy [26].

Total magnetization A finite total magnetization $\langle M \rangle_\beta$ identifies a ferromagnetically ordered state. Ferromagnetic materials can spontaneously break symmetries and realize order. A prominent example is the two-dimensional Ising model exhibiting a spontaneous magnetization below a critical temperature such that it breaks the discrete spin symmetry [258, 190]. While the total magnetization can be defined along an arbitrary polarization axis \mathbf{e} with $|\mathbf{e}| = 1$

$$\langle \mathbf{m} \rangle_\beta = \sum_{j=1}^N \langle \mathbf{e} \cdot \mathbf{S}_j \rangle_\beta = \sum_{j=1}^N \frac{\sum_i \langle \Psi_i | \mathbf{e} \cdot \mathbf{S}_j | \Psi_i \rangle e^{-\beta E_i}}{\sum_i e^{-\beta E_i}}, \quad (4.8)$$

we usually refer to the magnetization along the z -axis, $\mathbf{e} = \begin{pmatrix} 0 & 0 & 1 \end{pmatrix}$.

Susceptibility Similar to the heat capacity, the magnetic susceptibility is easily accessible in experiments and provides direct access to the magnetic correlations of the system. It measures the response of the material to an external magnetic field. The susceptibility is defined by the derivative of the total magnetization with respect to the external field strength h or as the variance of the total magnetization, which is possible in principle. For simplicity, we consider the magnetization along the z -axis which is aligned with the external field:

$$\chi = \frac{\langle m_z \rangle_\beta}{\partial h} = \beta (\langle m_z^2 \rangle_\beta - \langle m_z \rangle_\beta^2) = \beta \left(\frac{\sum_i \langle \Psi_i | m_z^2 | \Psi_i \rangle e^{-\beta E_i}}{\sum_i e^{-\beta E_i}} - \left[\frac{\sum_i \langle \Psi_i | m_z | \Psi_i \rangle e^{-\beta E_i}}{\sum_i e^{-\beta E_i}} \right]^2 \right) \quad (4.9)$$

However, effective spin models, strong crystal fields, or anisotropies induce a more complicated response to the external field. This is the case for dipolar-octupolar pyrochlores, cf. Equation 3.8.

Spin correlation The spin correlation, and its Fourier transform, are frequently discussed throughout the thesis. An important quantifier for different phases of matter is the scaling of the correlation length with distance

$$\langle \mathbf{S}_n \cdot \mathbf{S}_m \rangle_\beta = \frac{\sum_i \langle \Psi_i | \mathbf{S}_n \cdot \mathbf{S}_m | \Psi_i \rangle e^{-E_i \beta}}{\sum_i e^{-E_i \beta}} = \begin{cases} \text{constant} & \text{long-range order} \\ \propto |\mathbf{r}_n - \mathbf{r}_m|^{-\gamma} & \text{algebraic decay} \\ \propto e^{-\gamma |\mathbf{r}_n - \mathbf{r}_m|} & \text{exponential decay} \end{cases} \quad (4.10)$$

At high temperatures in a paramagnetic regime, all spins are essentially uncorrelated expressed by an exponentially decaying correlation function. Lowering the temperature enhances correlations yielding an algebraic decay or long-range order. This occurs in both classical and quantum systems alike.

The spin structure factor $\langle S(\mathbf{Q}) \rangle_\beta$, where \mathbf{Q} is a reciprocal lattice vector, is the Fourier

transform of the spin correlator and can be measured in neutron experiments [259, 260]:

$$\langle S(\mathbf{Q}) \rangle_\beta = \sum_{n,m=1}^N e^{-i\mathbf{Q} \cdot (\mathbf{r}_n - \mathbf{r}_m)} \langle \mathbf{S}_n \cdot \mathbf{S}_m \rangle_\beta \quad (4.11)$$

It encodes the correlations in reciprocal space and identifies characteristic fingerprints of various phases. While a disordered paramagnet is mainly featureless, ordered states develop pronounced Bragg peaks induced by long-range order. But frustrated magnets, like CSI, also have distinct features like bowties and pinch-points, as discussed in the following sections.

4.2 Thermodynamics of the pyrochlore Heisenberg antiferromagnet

Pyrochlore $S = \frac{1}{2}$ Heisenberg antiferromagnet at finite temperature

Phys. Rev. B **102**, 054408 (2020)

R. Schäfer, I. Hagymási, R. Moessner, and D. J. Luitz

Despite intense research, the lack of methods due to its frustration and three-dimensionality leaves many open questions concerning zero and finite temperature of the quantum pyrochlore $S = 1/2$ Heisenberg antiferromagnet. Indeed, not only its ground state is under debate, *cf.* [Chapter 5](#), we also lack an understanding of its thermodynamic properties [[130](#), [131](#), [134](#), [132](#), [133](#), [135](#), [261](#), [254](#)]. This section focuses on the thermodynamics of the isotropic Heisenberg model using a combination of advanced numerical techniques: NLCE, finite-temperature DMRG, and quantum typicality. As it does not suffer from dimensionality, frustration, and entanglement growth, the NLCE algorithm [[125](#), [126](#), [127](#), [128](#)] provides unbiased insight into this otherwise barely accessible model. The extensive use of symmetries presented in [Section 2.1](#) and the generalized framework of NLCE presented in [Section 2.2](#) allows us to push state-of-the-art numerics and to include clusters with non-trivial hexagonal and octagonal loops in a tetrahedron-based expansion for the first time [[130](#), [131](#), [134](#), [132](#), [133](#), [135](#)]. Boosting the convergence using the Euler resummation algorithm makes temperatures around $T_{\text{conv}} = 0.25 J$ accessible, thereby fully resolving the Schottky anomaly with a pronounced maximum in the specific heat at $T_{\text{max}} = 0.57 J$. Strikingly, even though the data is fully converged beyond the peak, only half of the residual entropy per spin, $0.47 k_B \log(2)$, is released within the limit of the convergence. Assuming a complete release of entropy as expected for generic models like this, the residual entropy provides the option for additional low-energy features, *e.g.* a second peak or a shoulder in the heat capacity. As we still lack a $S = 1/2$ Heisenberg pyrochlore candidate material, our data is compared to experiments on the (approximate) $S = 1$ Heisenberg material, $\text{NaCaNi}_2\text{F}_7$ [[254](#)], and the classical spin ice material $\text{Dy}_2\text{Ti}_2\text{O}_7$ [[235](#)].

4.2.1 Model and Methods

We investigate the isotropic Heisenberg model on the pyrochlore lattice with an additional local field:

$$H = J \sum_{\langle i,j \rangle} \mathbf{S}_i \cdot \mathbf{S}_j + h \sum_i S_i^z \quad (4.12)$$

The field strength h is in units of J and orientated in the $[001]$ direction. Most results presented are obtained by the NLCE algorithm as it provides unbiased insights into the thermodynamic limit. The efficient usage of symmetries in [Section 2.1](#) combined with the generalized framework

introduced in Section 2.2 allows us to carry out the tetrahedron-based expansion up to the eighth order. Many non-trivial exchange processes, such as the ring-exchange term in QSI, only occur by including hexagonal and octagonal loops and are crucial in frustrated systems. Their contributions, included in clusters of size six, seven, and eight, are significant even at high temperatures. Hence, expansions up to order five and lower [130, 131, 134, 132, 133, 135] fail to capture the three-dimensionality of the model and are essentially equivalent to a Husimi cactus of tetrahedra.

The bottleneck of the algorithm is the full diagonalization. Using graph and group-theoretic approaches, we can fully diagonalize the arising clusters containing up to 25 spins within the pyrochlore lattice, unprecedented for generic clusters of a similar size. A tetrahedron-based expansion is particularly well suited for the use of spatial symmetries as individual clusters contain (sometimes macroscopically) many automorphisms. Most tetrahedra of a specific cluster exhibit two or even three exterior sites. These sites can independently be permuted, yielding a huge number of possible symmetries. This makes it possible to include larger clusters to reach non-trivial temperatures. The NLCE algorithm and the efficient use of symmetries is described in detail in Chapter 2.

In addition to the extensive use of spatial symmetries, we exploit the total magnetization and spin inversion symmetry. Notably, the total magnetization sorts all eigenstates according to their magnetization. Therefore, an additional external field, $h > 0$, simply manifests itself as a shift of the eigenvalues within each magnetization sector m_z : $E_i \rightarrow E_i + hm_z$. Hence, different field strengths can be easily computed without the need to diagonalize each cluster for each value of h .

Complementary to NLCE, we present results from canonical typicality calculations on a finite cluster consisting of $2 \times 2 \times 2$ unit cells (32 sites) and a larger system (48 sites) with periodic boundary conditions using a finite-temperature tensor network method. In contrast to NLCE, quantum typicality uses matrix exponentials and can be computed using Krylov space methods [110, 150], making larger systems traceable as they exploit the sparsity of the Hamiltonian. Canonical typicality [262, 263] approximates an observable by an ensemble of typical thermal wavefunctions at an inverse temperature β , $|\beta_i\rangle = e^{-\beta/2H}|\Psi_i\rangle$.

$$\langle O \rangle_\beta = \frac{\text{Tr}(e^{-\beta H} O)}{Z} = \sum_i \frac{\langle \beta_i | O | \beta_i \rangle}{\langle \beta_i | \beta_i \rangle} + \mathcal{O}(e^{-N}) \quad (4.13)$$

Sampling over different states $|\Psi_i\rangle$ reduces the statistical error [264, 265, 111, 151]. The initial states are randomly initialized and correspond to infinite-temperature states. Furthermore, we demonstrate that tensor-network methods are capable of reaching non-trivial temperatures and providing accurate results for thermodynamic quantities [99, 100, 266]. The two most prominent approaches for imaginary-time evolution are the time-evolving block decimation (TEBD) [97, 98] and time-dependent variational principle (TDVP) [267, 268, 269], which is utilized in this work. Performing Krylov space methods with MPS fails at an early stage as the MPS can not capture

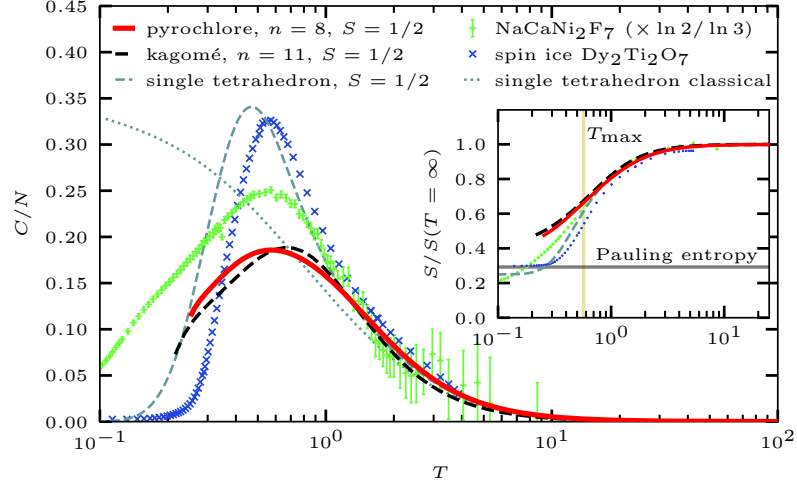


Figure 4.1: Heat capacity per site in the isotropic pyrochlore Heisenberg $S = 1/2$ antiferromagnet ($J = 1$). The red curve shows the converged data obtained by the tetrahedron-based Euler transform up to the eighth order (this work). The data is compared to a single tetrahedron for the quantum (dashed) and classical (dotted) calculation, as well as experimental data for an (approximate) Heisenberg spin-1 material NaCaNi₂F₇ [254] (green) and the classical spin ice component Dy₂Ti₂O₇ [235] (blue). The temperature axis was adjusted such that the peak of the experimental data matches the peak obtained by NLCE. The data of the single classical tetrahedron was shifted to match the high-temperature tail. To compensate the different spin length, the NaCaNi₂F₇ data was scaled by $\ln(2)/\ln(3)$. Additionally, the plot shows unpublished NLCE data of the kagomé Heisenberg antiferromagnet up to the eleventh order (86 of 113 topologically invariant clusters were included), *cf.* Figure 2.12a. Similarly, the inset shows the entropy per site as a function of temperature, where the black line represents Pauling’s estimate for the residual entropy of CSI. The yellow vertical line indicates the position of the maximum.

the entanglement efficiently [270]. By its construction, MPS approaches are one-dimensional. Therefore, long-range interactions are induced from the one-dimensional “snake path” placed in the three-dimensional system inducing long-range entanglement. In order to capture the growing entanglement at non-trivial temperatures, up to $\chi_{\max} = 10\,000$ $SU(2)$ -symmetric states are used. The energy is extrapolated to an infinite bond dimension which then defines the heat capacity as its derivative.

4.2.2 Results

Various thermodynamic observables are examined using NLCE down to the limit of convergence, $T_{\text{conv}} \approx 0.25 J$. We start by discussing the heat capacity and entropy. Notably, the heat capacity is well defined and accessible in experiments down to low temperatures and encodes low-energy excitations. The entropy, closely related to the specific heat, describes the spectral weight. Further, we consider the magnetic susceptibility and magnetization process as a function of the

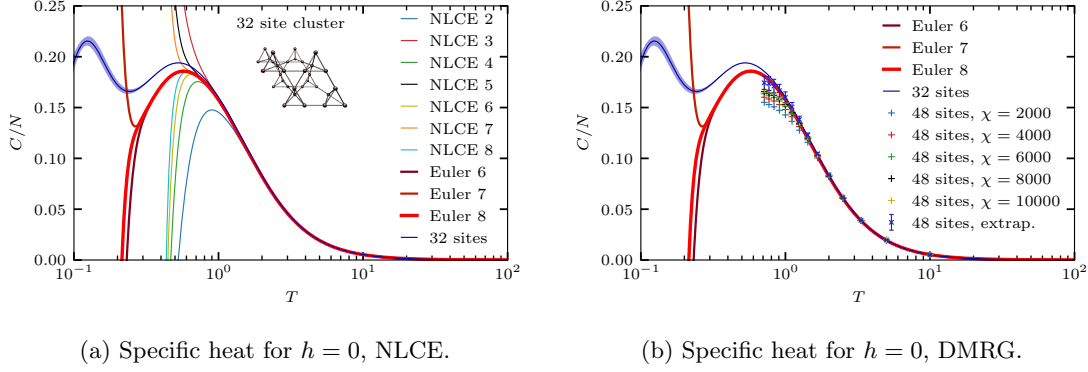


Figure 4.2: Heat capacity of quantum pyrochlore Heisenberg $S = 1/2$ antiferromagnet ($J = 1$) calculated with NLCE, quantum typicality, and finite-temperature DMRG. The blue curve refers to quantum typicality data obtained from the cluster shown in (a) with $2 \times 2 \times 2$ unit cells, $N = 32$. DMRG was performed on a cluster with $N = 48$ sites with periodic boundary conditions.

field strength, $h > 0$. Lastly, we address the static spin structure factor and discuss prominent features like bowties and pinch-points already observed at high temperatures. By comparing the applied numerical techniques, we demonstrate the capability of MPS approaches down to non-trivial temperatures and identify finite-size effects in the 32-sites cluster.

Heat capacity The heat capacity measures the amount of internal energy needed to change the temperature by a predefined amount. It is extracted as the derivative with respect to the temperature or as the variance of the internal energy. Being easily accessible in experiments makes it an important quantity as it identifies possible phase transitions by a sharp peak as well as low-energy excitations. This paragraph solely discusses results obtained for pyrochlore Heisenberg $S = 1/2$, and a comparison to other models, *cf.* Figure 4.1, is made in the conclusion.

The convergence of individual NLCE orders and their Euler transform up to the eighth order are illustrated in Figure 4.2a. It reveals the characteristic alternating behavior and the boost in convergence from $T \approx 0.7 J$ to $T_{\text{conv}} \approx 0.25 J$ using the Euler resummation algorithm. These results provide an unbiased benchmark in the thermodynamic limit and unambiguously resolve the maximum at $T_{\text{max}} \approx 0.57 J$. The inset displays the cubic finite-size cluster with $N = 32$ examined using quantum typicality, the blue curve. While the high-temperature tail is well captured, decaying with $1/T^2$, strong finite-size effects already enter the stage around the Schottky anomaly yielding visible discrepancies. This suggests important correlations beyond the range of the finite cluster containing only $2 \times 2 \times 2$ unit cells. Despite the finite-size effects, the 32-sites cluster (and even smaller) is frequently studied at finite and even zero temperature [271, 261, 272, 95, 273]. The NLCE data further indicates a substantial decay of the heat capacity beyond its maximum, contradicting the pronounced second peak in the specific heat around $T \approx 0.15 J$ of the finite-size cluster. Therefore, we conclude that this peak is unstable in the thermodynamic limit.

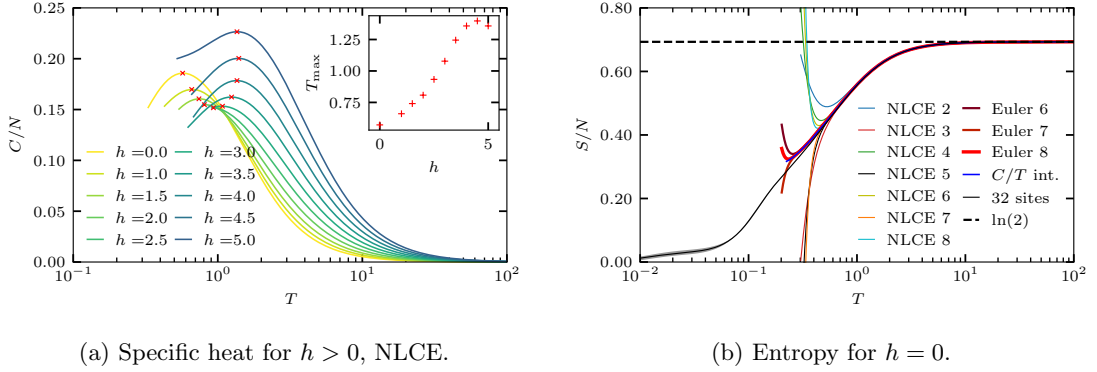


Figure 4.3: (a) Heat capacity of the quantum $S = 1/2$ pyrochlore Heisenberg antiferromagnet ($J = 1$) in an external field $h > 0$. Inset shows the maximum of the Schottky anomaly as a function of the field strength h . (b) Entropy per site for $h = 0$. The blue curve was obtained by integrating the specific heat data.

Figure 4.2b demonstrates the convergence of finite-temperature MPS in three dimensions up to $T \gtrsim 0.6J$ for a cluster with 48 sites and periodic boundary conditions. MPS approaches beyond one dimension are notoriously tricky due to the growth of entanglement. The three-dimensional pyrochlore is not an exception, as the convergence strongly depends on the bond dimension χ when the system enters a non-trivial quantum phase below $T < 2J$. Enlarging the bond dimension improves the results such that the extrapolated data reflect the thermodynamic limit. DMRG, similar to quantum typicality, is also restricted to a cluster of finite size, which will likely suffer from finite-size effects beyond the maximum.

The NLCE algorithm allows us to easily include an external field in [001] direction as defined in Equation 4.12. We systemically investigate the specific heat in the presence of a magnetic field in Figure 4.3a and observe a shift in temperature of the specific heat maximum, as shown in the inset. In the limit of strong fields, the model is described by a simple uncorrelated paramagnet exhibiting the overall upward shift of the maximal heat capacity. However, intermediate fields induce a complex response as indicated by a non-monotonic shift of the maximum height. The complex behavior is further expressed by the inability of the algorithm to reach similar temperatures as in the case of zero or strong fields.

Entropy The entropy, Figure 4.3b, is closely related to the specific heat as it can be obtained by simply integrating the specific heat

$$S(T_2) - S(T_1) = \int_{T_1}^{T_2} dT \frac{C}{T} \quad (4.14)$$

with $S(\infty) = N \log(2)$. Therefore, the entropy can be either integrated or directly computed for the individual clusters in NLCE. Determining the entropy using NLCE requires including

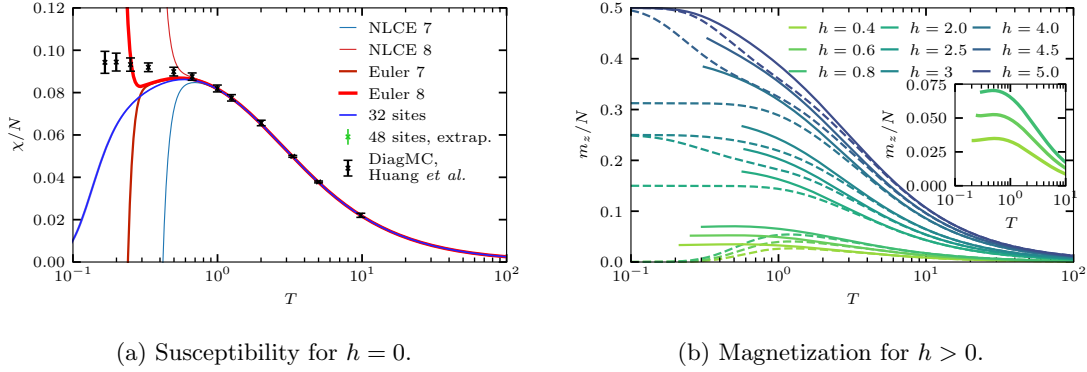


Figure 4.4: Magnetic observables as a function of temperature computed for the quantum pyrochlore Heisenberg $S = 1/2$ antiferromagnet ($J = 1$). (a) Magnetic susceptibility per site computed with different methods and compared to diagrammatic Monte Carlo data [224]. (b) Magnetization process per site as a function of field strength for the eighth order NLCE (solid lines) and a single tetrahedron (dashed lines).

the zeroth order, as described in Section 2.2. Even though the data is converged far below the first peak, only roughly half of the entropy is released, $S/N \approx 0.47 \ln(2)$. A large residual entropy is characteristic of frustrated magnets as it reflects the macroscopically large low-energy manifold and its competing states. The inset in Figure 4.1 compares the spectral weight to other frustrated models and reveals that the pyrochlore $S = 1/2$ exhibits the largest among all models. Particularly, it is greater than the entropy of proposed RVB states, leaving it as an option in the low-temperature limit [225, 228, 231, 232]. While some classical models, like spin ice in Section 3.2, or fine-tuned quantum models [274, 275, 276] exhibit a finite residual entropy down to zero temperature, this is not expected for generic cases such as the investigated model. The third law of thermodynamics demands the release of all spectral weight at zero temperature. For example, this is observed for CSI materials such as $\text{Dy}_2\text{Ti}_2\text{O}_7$ or the entropy of water ice, *cf.* Section 3.2.

Magnetic susceptibility The magnetic susceptibility is the derivative of the total magnetization with respect to the field strength. Since all eigenvalues are associated with the total magnetization, the susceptibility can be easily computed as the variance of the magnetization. Note that the total magnetization is zero for all temperatures $h = 0$. Therefore, evaluating the susceptibility in the zero field case simply reduces to

$$\chi = \beta \langle m_z^2 \rangle_\beta = \beta \frac{\sum_i \langle \Psi_i | m_z^2 | \Psi_i \rangle e^{-\beta E_i}}{\sum_i e^{-\beta E_i}}. \quad (4.15)$$

Similar to the magnetization of an eigenstate, the square of the total magnetization is obtained by $\langle \Psi_i | m_z^2 | \Psi_i \rangle = |m_z|^2$. The susceptibility exhibits a similar convergence as the other observables, $T_{\text{conv}} \approx 0.25 J$. The data, shown in Figure 4.4a, reveals a maximum around $T \approx 0.54 J$. We

compared our results to a diagrammatic MC simulation [224]. All methods – NLCE, DMRG, typicality, and diagrammatic MC – agree in the high-temperature regime $T \gtrsim 1J$. Within the region of convergence, the finite-size effects of the 32-sites cluster seem less influential than for the specific heat. However, the MC data indicates a slight increase or a plateau beyond the NLCE maximum, contradicting the NLCE results revealing a decay. Note that the deviation occurs parallel with an increase in the errors; hence, the validity of the MC data is questionable for $T < 1J$.

Magnetization While the zero field case does not exhibit any magnetization at finite and zero temperature, an external field induces a finite magnetization. The magnetization process as a function of temperature for different field strengths is shown in Figure 4.4b. It shows the converged results in the eighth order (solid lines) and compares them to a single tetrahedron (dashed lines). The ground state of a single tetrahedron exhibits only discrete magnetization values $m_z/N = 0, \pm 1/4, \pm 1/2$. However, accidental degeneracies yield intermediate values for $h = 2$ and $h = 4$. In the high-temperature limit, the NLCE data and the single tetrahedron follow Curie’s law. While the agreement is remarkably good up to $T \gtrsim 1J$, finite-size effects enter the stage at lower temperatures.

Both, the NLCE data and the single tetrahedron indicate a maximum in the magnetization curve at finite temperature for small field strengths, *cf.* inset in Figure 4.4b. This phenomenon is not surprising as the ground state remains non-magnetic for small fields and entropic arguments yield zero magnetization in the high-temperature limit. However, the energy-entropy competition induces a finite magnetization regime at intermediate temperatures, as magnetic states exhibit a significant spectral weight. Extensive DMRG calculations indicate a stable half-magnetization plateau at zero temperature for $2.16J \leq h \leq 2.48J$, *cf.* Section 5.2. This suggests that the NLCE data of the respective field strengths converges to $m_z/N = 1/4$ in the zero-temperature limit. The saturation field, where we expect a fully polarized state, is $h_{\text{sat}} = 4J$.

Static spin structure factor We further computed the spin structure factor at finite temperature using DMRG. It is the Fourier transform of the spin correlator:

$$S(\mathbf{Q}) = \frac{4}{3N} \sum_{\langle i,j \rangle} \langle \mathbf{S}_i \cdot \mathbf{S}_j \rangle_{\beta} \cos[\mathbf{Q} \cdot (\mathbf{R}_i - \mathbf{R}_j)] \quad (4.16)$$

Figure 4.5a shows the spin structure factor for the cluster with 48 sites. The columns correspond to different temperatures ranging from $T = 10J$ to $T = 0.77J$, the limitation of the method. The upper rows display the (H, H, L) plane, $Q_x = Q_y$, and the lower rows display $(H, L, 0)$, $Q_z = 0$, plane.

The model does not exhibit any sign of Bragg peaks. Remarkably, the characteristic features of the frustrated magnets emerge at a relatively high temperatures above the Schottky anomaly. Bowties [225, 221, 228, 254, 261], a consequence of a total spin zero on all tetrahedra, emerge

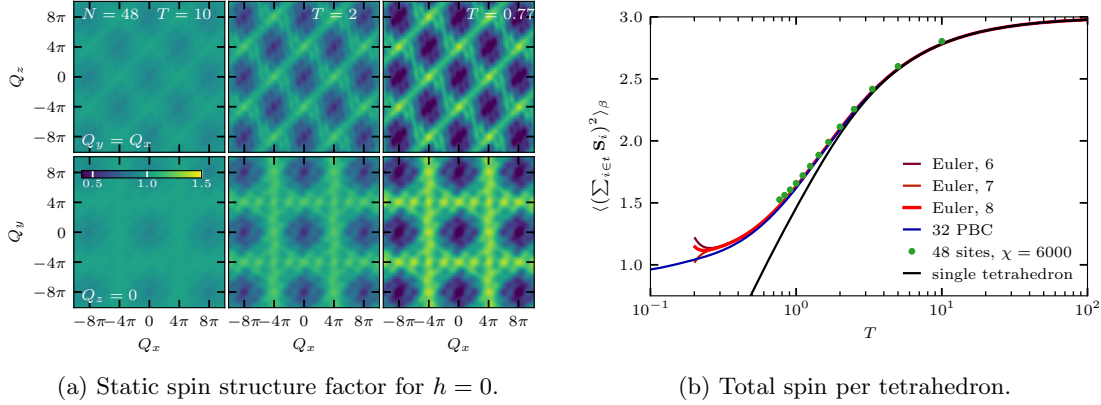


Figure 4.5: (a) Static spin structure factor of a finite cluster ($N = 48$) at finite temperature using DMRG and (b) the total spin per tetrahedron as a function of temperature derived by different methods. The total spin is encoded in the internal energy $\langle H \rangle_\beta$ via Equation 4.17.

around $T \approx 2J$. While CSI yields infinitely sharp pinch-points, this is not possible in the quantum realm, as two tetrahedra sharing a spin can not host two singlets simultaneously [160, 277]. The inability of a quantum system to form a non-vanishing total spin yields fluctuations inducing a finite width of pinch-points, as observed in Figure 4.5a. The pinch-points are located at $(\pm 2\pi, \pm 2\pi, \pm 2\pi)$ and $(0, 0, \pm 4\pi)$. A detailed analysis of their width is not possible within the limit of our resolution since the correlation length quickly exceeds the linear system size.

Furthermore, the total spin of a tetrahedron can be accessed via the internal energy of the system ($J = 1$):

$$\langle H \rangle_\beta = \left\langle \sum_{t \in \mathcal{T}} \frac{1}{2} \left(\sum_{i \in t} \mathbf{S}_i \right)^2 - \frac{3}{2} \right\rangle_\beta \Rightarrow \left\langle \left(\sum_{i \in t} \mathbf{S}_i \right)^2 \right\rangle_\beta = 4 \frac{\langle H \rangle_\beta}{N} + 3 \quad (4.17)$$

Pinch-points get infinitely sharp if $\sum_{i \in t} \mathbf{S}_i = 0$. Hence, the total spin can be used as a quantifier for their widths [277]. We can use the NLCE result of the energy in the eighth order to determine the total spin of a single tetrahedron in the thermodynamic limit at finite temperatures, cf. Figure 4.5b. A naive extrapolation to zero temperature yields $\sum_{i \in t} \mathbf{S}_i \approx 1$, confirming the inability to host singlets simultaneously on all tetrahedra. This is consistent with the predicted ground-state energy from Section 5.1 and Section 5.3.

4.2.3 Conclusion

This project provides new insights in two ways: methodological and physical. First, we demonstrated the application of finite-temperature DMRG to non-trivial temperatures and pushed current state-of-the-art numerics by reaching the eighth order within a tetrahedron-based expansion. The general NLCE approach allows to compare different expansions – single site, unit cell,

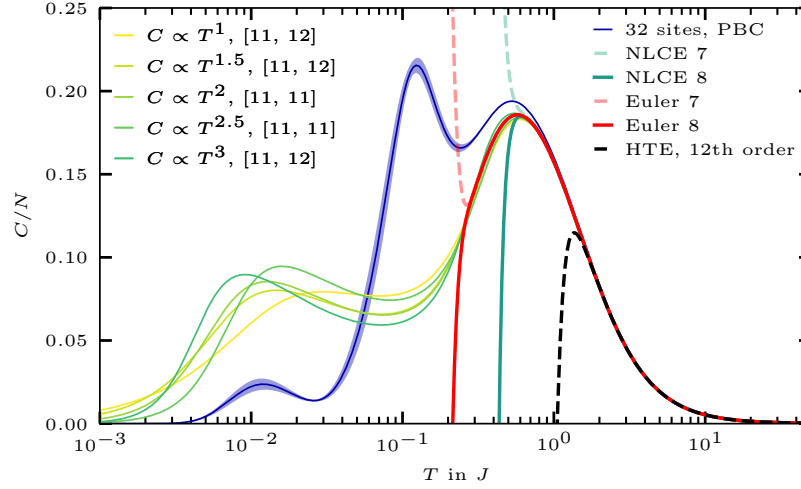


Figure 4.6: Interpolated specific heat data using with the entropy method [272]. Using the NLCE data as a high-temperature input and an estimate of the ground-state energy from chapter Chapter 5, $E_0 = -0.49 J$, allows an interpolation of the entire temperature range. Different curves model different scaling behaviors of the heat capacity $C \propto T^\alpha$ for $T \rightarrow 0$ and $[\cdot, \cdot]$ refers to the Padé approximants. The high-temperature expansion data is from Ref. [278, 279, 272]. The data was kindly provided by Johannes Richter and Taras Hutak using our inputs.

and tetrahedron [cf. Figure 2.11] – up to previously inaccessible orders, which is possible due to the automatic detection algorithm presented in Section 2.1. Notably, we included hexagonal and octagonal loops for the first time. Second, we generated unbiased insights into thermodynamic properties of quantum pyrochlore $S = 1/2$ Heisenberg antiferromagnet, which is not available to this extent. Especially observables like the specific heat and magnet susceptibility are important quantities as they encode excitations and correlations and are easily accessible up to high precision in experiments.

We compare the specific heat data to other frustrated models and experiments in Figure 4.1. It includes the unpublished NLCE data for kagomé Heisenberg antiferromagnet, a single tetrahedron treated classically as well as quantum mechanically, experimental data for the spin ice material $\text{Dy}_2\text{Ti}_2\text{O}_7$ [235], and the spin-1 Heisenberg compound $\text{NaCaNi}_2\text{F}_7$ [252, 253, 254]. The spin-1 data is rescaled by $\ln(2)/\ln(3)$ to compensate for the larger entropy induced by a larger spin length. A global energy scale induces a rescaling of the temperature axis. Therefore, to allow for objective comparison, we shifted the experimental data such that the maxima agree with the numerical simulation. The data from the single classical tetrahedron was shifted to agree with the high-temperature tail of the NLCE data. While all models agree in the high-temperature regime, they exhibit qualitative differences as the height and form of the peak differ. This is, however, not surprising as we are dealing with similar but, in the end, different models.

The inset of Figure 4.1 evaluates the released entropy of the different models. All models,

except the kagomé, show a significant downshift in the spectral weight compared to the NLCE calculation of $S = 1/2$ Heisenberg antiferromagnet. The most rapid release of the spectral weight is observed by the spin ice compound exhibiting the Pauling entropy $S = \frac{1}{2} \log \frac{3}{2}$ at low temperatures. Also, due to the large singlet gap, a single tetrahedron shows a rapid decrease in entropy. $\text{NaCaNi}_2\text{F}_7$ exhibits a broader peak in the specific heat than the previous two models and initially shows a similar release of entropy as the NLCE calculation. However, the release increases around the peak, yielding a downshift in spectral weight at lower temperatures. There is a striking resemblance between the spectral entropy of the pyrochlore and the kagomé $S = 1/2$ Heisenberg antiferromagnet. The kagomé's entropy is larger than predicted by high-order series expansion, which yields $0.475 \ln(2)$ already at $T \approx 0.3 J$. The NLCE calculation predicts a similar value around $T \approx 0.2 J$. Despite the larger order in the two-dimensional case, both NLCE calculations on the kagomé and the pyrochlore break down around a similar spectral weight and temperature. While the Heisenberg models on both lattices have a similar spectral weight, the situation is different for the Ising case. The residual entropy of the Ising magnet on the kagomé lattice, 0.50183 [280], is much larger than in the case of the pyrochlore, 0.20273 [27], suggesting a higher degree of frustration.

While our data provide a detailed insights into the model's high-temperature regime, it cannot resolve the low-energy subspace. Obtaining an understanding of the intermediate or low-temperature realm is challenging. However, interpolation methods based on some knowledge of the high-temperature behavior and the ground state (and its excitation) allow value insights [281, 282, 283, 272]. Combining the entropy interpolation scheme utilized in Ref. [272] with the high-temperature data from NLCE and a precise determination of the ground-state energy from chapter Chapter 5 provides estimates for the entire temperature regime. The result is shown in Figure 4.6. The interpolation is based on thermodynamic constraints: $\int_0^\infty C(T) dT = -E_0$ and $\int_0^\infty C(T)/T dT = S(T = \infty)$. The algorithm approximates the entropy as a function of the energy, $[E_0, 0]$, using Padé approximants, where $E_0 = -0.49 J$ is an estimate for the ground-state energy. The ground-state energy is obtained from extensive DMRG calculation, cf. Section 5.1 [2], and variationally from a hard-hexagon crystal, cf. Section 5.3 [6]. The low-temperature limit is approximated using some reasonable guesses for the excitations in the model. For example, a cubic scaling of the heat capacity, as expected from the pyrochlore-photons [168, 284, 194], for $T \rightarrow 0$ induces $S(E) \propto (E - E_0)^{3/4}$. The experimental data from $\text{NaCaNi}_2\text{F}_7$ suggests a $T^{2.2}$ -scaling [254]. Figure 4.6 shows different scenarios. The different curves suggest the existence of a small second peak or a shoulder around $T \approx 10^{-2} J$ in the heat capacity. The predicted temperature is surprisingly low, even for frustrated magnets, and comparable to the peak of QSI [76, 77].

To conclude, this work demonstrates the successful application of NLCE and DMRG at finite temperatures. It lays the foundation for further research on pyrochlores at finite temperatures, carried out in the following section. All in all, we can say that the pyrochlore $S = 1/2$ Heisenberg antiferromagnet is at least as frustrated as other models and provides an exciting playground for

the exotic physics associated with frustrated magnetism – even at finite temperatures.

Dr. Imre Hagymási performed the finite-temperature DMRG calculation. Based on the NLCE input, Prof. Johannes Richter and Dr. Taras Hutak interpolated the specific heat using the entropy method.

4.3 The dipolar-octupolar $\text{Ce}_2\text{Zr}_2\text{O}_7$ and $\text{Ce}_2\text{Sn}_2\text{O}_7$

Case for a $U(1)_\pi$ Quantum Spin Liquid Ground State in the Dipole-Octupole Pyrochlore $\text{Ce}_2\text{Zr}_2\text{O}_7$

[Phys. Rev. X 12, 021015 \(2022\)](#)

E. M. Smith, O. Benton, D. R. Yahne, B. Placke, R. Schäfer, J. Gaudet, J. Dudemaine, A. Fitterman, J. Beare, A. R. Wildes, S. Bhattacharya, T. DeLazzer, C. R. C. Buhariwalla, N. P. Butch, R. Movshovich, J. D. Garrett, C. A. Marjerrison, J. P. Clancy, E. Kermarrec, G. M. Luke, A. D. Bianchi, K. A. Ross, and B. D. Gaulin

Dipolar spin ice regime proximate to an all-in-all-out Néel ground state in the dipolar-octupolar pyrochlore $\text{Ce}_2\text{Sn}_2\text{O}_7$

[10.48550/ARXIV.2211.15140 \(2022\)](#)

D. R. Yahne, B. Placke, R. Schäfer, O. Benton, M. Powell, J. W. Kolis, C. Pasco, A. F. May, E. M. Smith, R. Moessner, B. D. Gaulin, M. D. Frontzek, S. A. Calder, and K. A. Ross

After demonstrating the capabilities of NLCE, its application to more generic models beyond the Heisenberg point is the next step. We consider models relevant for the description of a particular class of materials, called dipolar-octupolar pyrochlores. They are composed of a trivalent rare-earth ion, Cerium in our case, and a non-magnetic tetravalent transition metal. Well-separated energy scales induce an effective pseudospin-1/2 description on the pyrochlore lattices as discussed in [Section 3.3](#). Dipolar-octupolar pyrochlores are well known for realizing exotic and conventional magnetic phases such as spin liquids, dipolar spin ice, and different ordered states [\[219, 220\]](#).

This section summarizes and analyzes recent experiments on Cerium-based pyrochlores, $\text{Ce}_2\text{Sn}_2\text{O}_7$ and $\text{Ce}_2\text{Zr}_2\text{O}_7$ [\[3\]](#), including low-temperature polarized neutron diffraction data, measurements of the heat capacity, as well as magnetic susceptibility. $\text{Ce}_2\text{Zr}_2\text{O}_7$ [\[245, 246, 285, 273\]](#) and its sister compound $\text{Ce}_2\text{Sn}_2\text{O}_7$ [\[286, 287, 247\]](#) have been actively studied during the past three years and reveal the wealth of unconventional phenomena associated with pyrochlores. Determining microscopic Hamiltonians in materials is notoriously a challenging task. The gold standard to estimate and constrain possible exchange parameters is fitting spin wave spectra, which have proven valuable for certain pyrochlore oxides [\[242, 288, 289, 290, 291, 292\]](#). If spin wave data are absent, other methods are required to obtain a glance into the microscopic model. NLCE is a powerful and reliable alternative to fit thermodynamic observables to constrain the microscopic exchange parameters in the material, allowing us to locate them in the phase diagram. Complementary to NLCE, classical and quantum MC, as well as semi-classical molecular dynamics calculations were performed. A similar procedure for $\text{Ce}_2\text{Zr}_2\text{O}_7$ was applied in Ref. [\[273\]](#).

Despite their similar chemical structure, we find striking differences during our analysis and come to fundamentally different conclusions regarding their quantum mechanical nature. Our

results place $\text{Ce}_2\text{Zr}_2\text{O}_7$ in a region on the phase diagram that is expected to host an exotic $U(1)_\pi$ QSL. In contrast, $\text{Ce}_2\text{Sn}_2\text{O}_7$ is placed in an ordered phase but in close proximity to a $U(1)_0$ QSL.

4.3.1 Model and Methods

Pyrochlore oxides have become an active research area in the past decade due to the exotic phenomena that are emerging from frustrated magnetism. The Cerium atoms form a network of corner-sharing tetrahedra, the pyrochlore lattice. The effective model describing the dipolar-octupolar pyrochlores is well established [21, 217, 243, 244, 239, 22, 170]. Single-ion physics dominates over exchange processes. A hierarchy of energy scales – Coulomb interaction over spin-orbit coupling over the crystal electric field – induces a ground-state doublet effectively described by a “pseudospin-1/2”. The x and z components of the effective doublet transform as a dipole and the y component as an octupole under lattice and time-reversal symmetry. The doublet is protected by a relatively large gap of order $\sim 100K$, much larger than the interaction scale between neighboring ions. Hence, exchange processes can be effectively described by (pseudo-) spin-1/2 operators at sufficiently low temperatures. For the dipolar-octupolar doublet, the nearest-neighbor exchange model allowed by symmetry is a XYZ -Hamiltonian:

$$H_{\text{DO}} = \sum_{\langle i,j \rangle} [J_x S_i^x S_j^x + J_y S_i^y S_j^y + J_z S_i^z S_j^z] - g_z \mu_B \sum_i \mathbf{h} \cdot \mathbf{z}_i (S_i^z \cos \theta + S_i^x \sin \theta) \quad (4.18)$$

Here, the x , y , and z operators refer to the pseudospins in their local frame [243, 244, 245, 246, 247]. Note that the field acts differently on each site of the tetrahedron according to its local \mathbf{z}_i -axis.

Computations for a XYZ -Hamiltonian are more demanding than for the previous XXX -Hamiltonian from Section 4.2. As the generic XYZ -Hamiltonian does not conserve the total magnetization (nor the spin inversion), only spatial symmetries – still powerful – are accessible. Hence, NLCE is limited to the seventh order, still including hexagonal contributions.

The model provides a fruitful playground for the exotic phenomena observed in frustrated magnets. Indeed, the model supports two $U(1)$ QSL exhibiting a 0- and π -flux through the hexagonal plaquettes known from QSI, *cf.* Section 3.2. There is a phase transition between the two QSLs. Additionally, in the limit of strong ferromagnetic transverse couplings, the model hosts an ordered XY -ferromagnet, also known as the all-in-all-out state in the dipolar-octupolar pyrochlore. Note that only half the phase diagram, mainly dominated by the XY -ferromagnet, is known, as it allows sign-free QMC calculation. The multipolar moments allow for further classification [293, 294, 295, 296]. A $U(1)$ QSL with a dominate coupling $|J_y| > |J_x|, |J_z|$ has an octupolar character and a dipolar character if $|J_x| > |J_y|$ or $|J_z| > |J_y|$. The same distinction applies to the AIAO state, which is octupolar for $J_y < J_x, J_z$ and dipolar for $J_x < J_y$ or $J_z < J_y$. In total, this yields six possible ground states, which are potentially realized by the dipolar-octupolar pyrochlores [219, 220]: an ordered all-in-all-out (AIAO) state, 0- and π -flux $U(1)$ QSL – each coming with a dipolar and octupolar character. It should be noted that recent studies

found evidence for \mathbb{Z}_2 QSL [77] as well as exotically ordered states beyond the perturbative QSI regime [2, 6] (more in Chapter 5).

We carry out the NLCE calculation up to sixth order, including non-trivial hexagonal loops, and determine the heat capacity for all (independent) parameter combinations J_x , J_y and J_z in Equation 4.18 for $|\mathbf{h}| = 0$. There are redundant parameter combinations when dealing with the specific heat. First, a global unitary $SU(2)$ rotation in spin space permutes the roles of x , y , and z but leaves the eigenvalues invariant. Hence, the heat capacity does not exhibit any directional information as it is purely derived from the eigenvalues. Indeed, the zero-field case allows a reduced set of parameters J_a , J_b , and J_c , which defines permutations of J_x , J_y , and J_z and follows the constraints:

$$|J_a| \geq |J_b|, |J_c| \quad \text{and} \quad J_b \geq J_c \quad (4.19)$$

Second, a global energy scale α , $J_i \rightarrow J'_i = \alpha J_i$, induces a rescaling of the temperature:

$$C(T) = \frac{1}{k_B^2 T^2} \left(\frac{\sum_i E_i^2 e^{-\frac{E_i}{k_B T}}}{\sum_i e^{-\frac{E_i}{k_B T}}} - \left[\frac{\sum_i E_i e^{-\frac{E_i}{k_B T}}}{\sum_i e^{-\frac{E_i}{k_B T}}} \right]^2 \right) \quad (4.20)$$

$$\rightarrow C'(T) = \frac{1}{k_B^2 T^2} \left(\frac{\sum_i \alpha^2 E_i^2 e^{-\frac{\alpha E_i}{k_B T}}}{\sum_i e^{-\frac{\alpha E_i}{k_B T}}} - \left[\frac{\sum_i \alpha E_i e^{-\frac{\alpha E_i}{k_B T}}}{\sum_i e^{-\frac{\alpha E_i}{k_B T}}} \right]^2 \right) = C(T/\alpha) \quad (4.21)$$

Hence, the three-dimensional parameter space spanned by (J_a, J_b, J_c) is reduced to two by setting $J_a = 1$ in numerical simulations and optimizing the global scale by $C(T) \rightarrow C(T/\alpha)$. It is, therefore, convenient to rewrite the Hamiltonian ($\mathbf{h} = \mathbf{0}$) in terms of $J_\pm = -\frac{1}{4}(J_b + J_c)/J_a$, and $J_{\pm\pm} = \frac{1}{4}(J_b - J_c)/J_a$:

$$H_{\text{DO}} = J_a \sum_{\langle i,j \rangle} S_i^a S_j^a - J_\pm (S_i^+ S_j^- + S_i^- S_j^+) + J_{\pm\pm} (S_i^+ S_j^+ + S_i^- S_j^-) \quad (4.22)$$

All independent parameter sets for the specific heat are obtained by $-1 \leq J_b \leq 1$ and $-1 \leq J_c \leq J_b$. This yields a triangular-shaped phase diagram, as illustrated in Figure 4.7 [220, 77, 219]. Determining the reduced parameters, J_\pm and $J_{\pm\pm}$, places the compounds in the ordered, 0-, or π -flux QSL phase. However, it does not identify the dominant magnetic moment and therefore does not reveal the dipolar or octupolar character. Hence, observables sensitive to the form of the magnetic moment, like the magnetic susceptibility, are required.

Experiments begin with the process of crystal growth. The measurement outcome is very sensitive to the sample quality and, therefore, the utilized synthesis technique. The synthesis of high-quality crystals is highly challenging and an important branch of science. A prominent issue occurring during synthesizing rare-earth pyrochlores is oxidation which reduces (in our case) the amount of magnetic Ce^{3+} by non-magnetic Ce^{4+} : $\text{Ce}_{2-2\delta}^{3+}\text{Ce}_{2\delta}^{4+}\text{B}_2\text{O}_{7-\delta}$. X-ray diffrac-

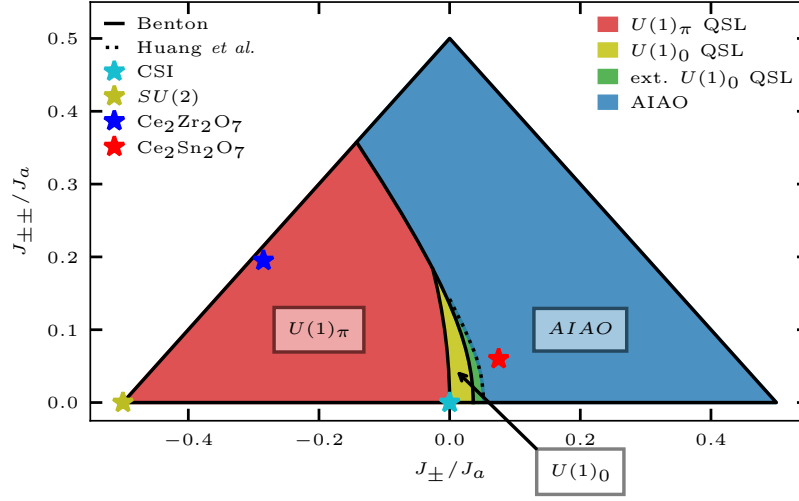


Figure 4.7: Expected phases for the XYZ -Hamiltonian on the pyrochlore lattice for J_{\pm} and $J_{\pm\pm}$ defined in Equation 4.22. The phase boundaries are determined by Benton (cluster mean-field theory) [220] and Huang *et al.* (QMC) [77]. CSI and $SU(2)$ refers to classical spin ice (Ising magnet) and the isotropic Heisenberg model, respectively. Both Cerium compounds refer to the optimal parameter set obtained from heat capacity measurements, *cf.* Figure 4.10.

tion allows an estimate for the oxidation level [297]. The estimate of the oxidation rate for $\text{Ce}_2\text{Zr}_2\text{O}_7$ is $\delta \approx 0.05$ for the single crystal and $\delta \approx 0.14$ for the powder sample [245]. Without protection, the oxidation process of the solid-state grown sample of $\text{Ce}_2\text{Zr}_2\text{O}_7$ is a matter of a few hours [245]. $\text{Ce}_2\text{Sn}_2\text{O}_7$ was synthesized hydrothermally, requiring significantly lower temperatures [298]. Therefore, oxidation in the tin compound is lower, which is confirmed by X-ray refinement. However, note that a non-magnetic impurity in $\text{Ce}_2\text{Sn}_2\text{O}_7$ makes up $\sim 3\%$ of the sample mass, inducing a systematic error in our analysis.

4.3.2 Results

Results for both materials are discussed side by side. The experimental data consists of polarized neutron diffraction, measurements of the heat capacity, and magnetic susceptibility at finite temperatures. We start by briefly discussing the neutron data before we examine the thermodynamic observables to obtain estimates for the microscopic exchange parameters. The procedure is based on large-scale NLCE calculations and maximizes the benefits of symmetries as in the previous Section 4.2.

Polarized neutron diffraction Neutron experiments are extremely complex but allow deep insights into the microscopic processes happening within the material. While data for $\text{Ce}_2\text{Zr}_2\text{O}_7$ was taken on a single crystal, measurements for $\text{Ce}_2\text{Sn}_2\text{O}_7$ were performed on a powder sample. More detailed experimental information and additional data of $\text{Ho}_2\text{Ti}_2\text{O}_7$ can be found in Ref. [3].

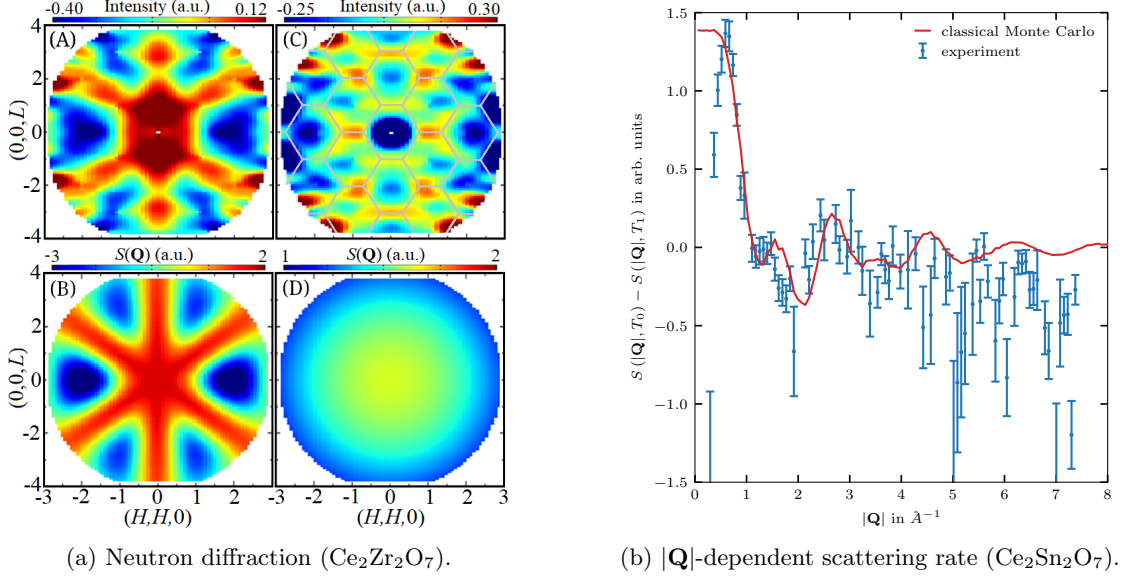


Figure 4.8: (a) $\text{Ce}_2\text{Zr}_2\text{O}_7$ diffuse scattering profiles in the (H, H, L) plane for the SF channel in subpanels (A) and (B) and NSF channel in subpanels (C) and (D). Subpanels (A) and (C) show the temperature-subtracted data obtained from $T_0 = 45$ mK and $T_1 = 10$ K. The face-centered cubic Brillouin zone is highlighted in gray in subpanel (C). The experimental data are compared to NLCE calculations, $(J_x, J_y, J_z) = (0.064, 0.063, 0.011)$ meV, with temperature subtraction, $T_0 = 0.5$ K and $T_1 = 10$ K, in the lower subpanels. E. Smith performed measurements, and O. Benton performed the NLCE calculation of the structure factor up to the order three [3]. (b) $|\mathbf{Q}|$ -dependent scattering rate for a hydrothermally synthesized powder sample of $\text{Ce}_2\text{Sn}_2\text{O}_7$ compared to classical MC simulation of the best parameter set: $(J_a, J_b, J_c) = (0.045, -0.001, -0.012)$ meV. The measurements were done at $T_0 = 0.3$ K and the background subtraction at $T_1 = 10$ K. D. Yahne performed measurements, and B. Placke performed the MC calculation.

Diffraction experiments for a single crystal $\text{Ce}_2\text{Zr}_2\text{O}_7$ were obtained using the D7 diffractometer [260] at the Institute Laue-Langevin. It independently determines spin-flip (SF) and non-spin-flip (NSF) scattering. Figure 4.8a shows the temperature subtracted data, 0.045 K and 10 K, of both channels and compares it to NLCE simulations up to the order three. The material exhibits quasi-pinch-points scattering in the SF channel around $(0, 0, 2)$, subpanel (A), which is, however, not as developed as in CSI materials like $\text{Ho}_2\text{Ti}_2\text{O}_7$. Quasi-pinch-point expected for $(1, 1, 1)$ and equivalent directions are washed out. Subpanel (B) provides equivalent data obtained from NLCE up to order three for the best data set; see below. Despite the temperature difference between NLCE (0.5 K) and the experiment (0.045 K), it allows for a sophisticated comparison. The SF scattering, subpanels (A) and (B), reveal strong similarities as the enhanced

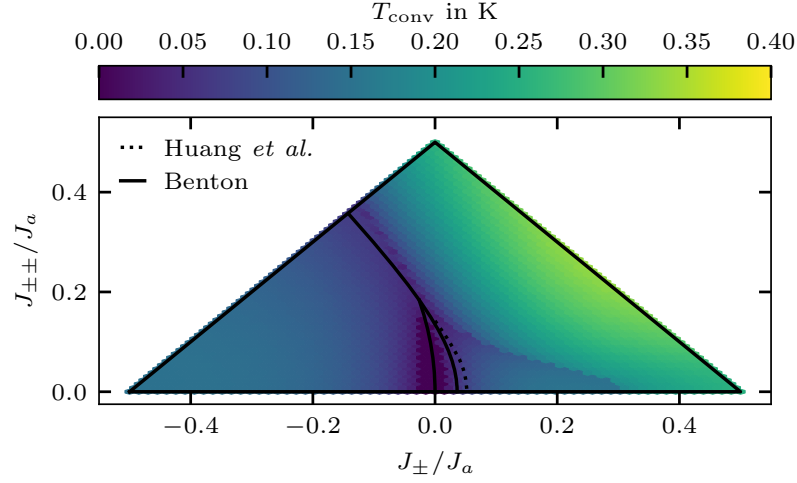


Figure 4.9: The lowest converged temperature in Kelvin of the sixth order NLCE data of the specific heat. The overall energy shift was set to match the high-temperature tail of $\text{Ce}_2\text{Sn}_2\text{O}_7$. The convergence T_{conv} is defined by $|C_{\text{NLCE},6} - C_{\text{NLCE},5}| > 0.1R$, where R is the gas constant.

intensity in $(1, 1, 1)$ and equivalent directions. However, sharper features like quasi pinch-points located at $(0, 0, 2)$ are absent in the numerics. The NSF scattering of $\text{Ce}_2\text{Zr}_2\text{O}_7$ shows similar features as $\text{Ho}_2\text{Ti}_2\text{O}_7$ as the zone-boundary scattering located at the face-centered cubic Brillouin zone, which is attributed to next-nearest neighbor and long-range dipolar interactions [207]. The face-centered cubic Brillouin zone is highlighted in gray in subpanel (C). The NLCE calculated NSF scattering is featureless, subpanel (D), and does not reproduce the zone-boundary scattering observed in $\text{Ce}_2\text{Zr}_2\text{O}_7$ or $\text{Ho}_2\text{Ti}_2\text{O}_7$ [207].

Experiments on $\text{Ce}_2\text{Sn}_2\text{O}_7$ were performed using WAND² with a hydrothermally grown powder sample. Diffusive scattering beyond 2 \AA^{-1} is absent and the data exhibit a peak around 0.5 \AA^{-1} , as shown in Figure 4.8b. Similar to $\text{Ce}_2\text{Zr}_2\text{O}_7$, the \mathbf{Q} -dependency of the hydrothermally grown sample of $\text{Ce}_2\text{Sn}_2\text{O}_7$ is reminiscent of dipolar spin ice, as found in $\text{Ho}_2\text{Ti}_2\text{O}_7$.

Note that the NLCE structure factor calculation and the classical MC simulation were not derived as a part of this thesis, *cf.* caption of Figure 4.8. This paragraph was included for completeness.

Heat capacity Both measurements of the specific heat agree with previous experiments on $\text{Ce}_2\text{Zr}_2\text{O}_7$ [246] and $\text{Ce}_2\text{Sn}_2\text{O}_7$ [247]. The heat capacity contains all excitations in the system, including phononic and magnetic ones. However, the magnetic contribution is naturally well separated at sufficiently low temperatures. Measurements confirm this for $\text{La}_2\text{Zr}_2\text{O}_7$, an isostructural non-magnetic compound, showing that phononic contributions can be neglected below 10K. Hence, the magnetic contribution from Ce^{3+} raising below $\sim 3 \text{ K}$ is well isolated. Both Cerium pyrochlores do not show any sign of an ordering transition. $\text{Ce}_2\text{Zr}_2\text{O}_7$ exhibits

an extremely broad plateau of the heat capacity compared to other pyrochlore models, *cf.* Figure 4.1, which decreases rapidly after $T \approx 0.08$ K. In contrast, $\text{Ce}_2\text{Sn}_2\text{O}_7$ shows a much steeper increase and exhibits a slimmer but higher specific heat peak.

The lowest converged temperature defined by the difference between the sixth and fifth order NLCE is shown in Figure 4.9. Notably, the sixth order includes the hexagonal loop for the first time. The difference between orders five and six arises mainly due to the inclusion of the hexagonal configuration, which is particularly strong in the ordered regime. NLCE fully resolves the Schottky anomaly associated with CSI constraint yielding a good convergence in the Ising limit. Strikingly, the convergence is generically better around the expected phase transitions; however, note that the transition is not resolved as it occurs below the lowest converged temperature.

The great advantage of NLCE is the determination of unbiased data in the thermodynamic limit without any restriction on the exchange parameters making the whole phase space accessible. We define the *goodness-of-fit* $\chi^2[C]$ for each (independent) set of exchange parameters by comparing the NLCE results with the experimental data. For each set of parameters, J_\pm and $J_{\pm\pm}$, we determine:

$$C_{\text{NLCE}}(T) = C_{\text{NLCE},6}(T) \quad (4.23)$$

$$\delta_{\text{NLCE}}(T) = \max_{T_i > T} |C_{\text{NLCE},6}(T_i) - C_{\text{NLCE},5}(T_i)|. \quad (4.24)$$

However, defining the goodness-of-fit consistently is tricky as it depends on the specific exchange parameters which affect the convergence of NLCE. First, we use the high-temperature tail of the measured heat capacity defined on $[T_0^{\text{high}}, T_1^{\text{high}}]$ to fit the exchange scale α . Second, all data points within $[T_0^{\text{low}}, T_1^{\text{low}}]$ define the goodness-of-fit. The experimental data consists of three parts, $C_{\text{exp}}(T) \pm \delta_{\text{unsys}}(T) + \varepsilon_C \delta_{\text{sys}}(T)$: C_{exp} is the actual data, and δ_{unsys} is the associated error. An uncertainty of the mass of $\text{Ce}_2\text{Sn}_2\text{O}_7$ induces a systematic error, which is included via $\varepsilon_C \in [-1, 1]$. The systematic error for $\text{Ce}_2\text{Zr}_2\text{O}_7$ is zero. Then, the goodness-of-fit is defined by

$$\chi[C]^2 = \sum_{T_0^{\text{low}} \leq T_i \leq T_1^{\text{low}}} \frac{(C_{\text{NLCE}}(T_i) - C_{\text{exp}}(T_i) - \varepsilon_C \delta_{\text{sys}}(T_i))^2}{\delta_{\text{NLCE}}(T_i)^2 + \delta_{\text{unsys}}(T_i)^2}. \quad (4.25)$$

The parameter $\varepsilon_C \in [-1, 1]$ is chosen for each set individually to minimize the goodness.

A total of 2279 independent parameter sets, J_\pm/J_a and $J_{\pm\pm}/J_a$, equally distributed over the phase space, *cf.* Figure 4.7, were used. The overall energy scale, J_a , was determined by matching the high-temperature tail of the data $[T_0^{\text{high}}, T_1^{\text{high}}] = [1.9 \text{ K}, 4 \text{ K}]$. The goodness-of-fit is evaluated for $[T_0^{\text{low}}, T_1^{\text{low}}] = [0.1 \text{ K}, 1.9 \text{ K}]$ and shown in a logarithmic scale for both materials in Figure 4.10. Dark blue regions indicate a good approximation. The optimal parameter sets are marked Figure 4.10 and explicitly plotted next to the experimental data in Figure 4.11 to allow for a direct comparison.

$\text{Ce}_2\text{Zr}_2\text{O}_7$ reveals two distinct regions of good approximation in either the $U(1)_\pi$ QSL or the ordered phase. The optimal parameters in the QSL phase are $(J_a, J_b, J_c) = (0.064, 0.062, 0.01) \text{ meV}$,

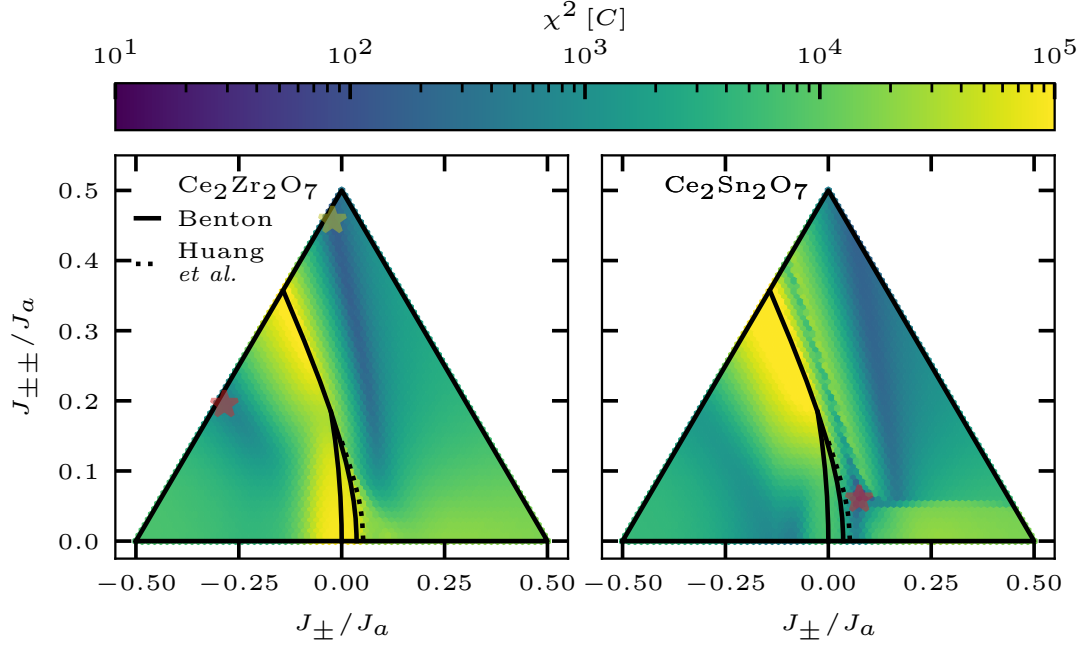


Figure 4.10: Goodness-of-fit of the heat capacity as defined in Equation 4.25. The overall energy scale was adjusted on [1.9 K, 4 K] and the goodness was estimated on [0.1 K, 1.9 K] using sixth-order NLCE calculation. Note that the Euler transform was not applied here as it misbehaves in the ordered region yielding unphysical data. The exchange parameters of the respective minima are given in the main text. The phase boundaries are determined by Benton [220] and Huang *et al.* [77].

and the ordered phase are $(J_a, J_b, J_c) = (0.054, 0.052, -0.05)$ meV. Notably, both estimates are close to an XXZ -Hamiltonian. Both minima exhibit an equally good approximation according to the goodness-of-fit defined in Equation 4.25. However, a direct comparison in Figure 4.11 provides strong evidence for the QSL scenario. Both parameter sets fully reproduce the high-temperature limit for $T > 1$ K. The specific heat for the parameters in the ordered phase for $\text{Ce}_2\text{Zr}_2\text{O}_7$ is shown in yellow and performs poorly compared to the experimental data. It nevertheless generates a small $\chi^2[C]$ since the error obtained from NLCE increases as soon as the curve deviates, yielding a lower weight for these data points. The approximation obtained from the QSL point is superior as it agrees much better with the experimental data. However, using the Euler resummation indicates a rapid decay shortly after the maximum is reached, contradicting the broad plateau observed experimentally. We attribute these differences between the experiment and the simulated nearest-neighbor Hamiltonian to additional weak further neighbor interactions as suggested by the zone-boundary scattering observed in the neutron data. The same calculations were additionally performed by assuming 5% vacancies without significant changes.

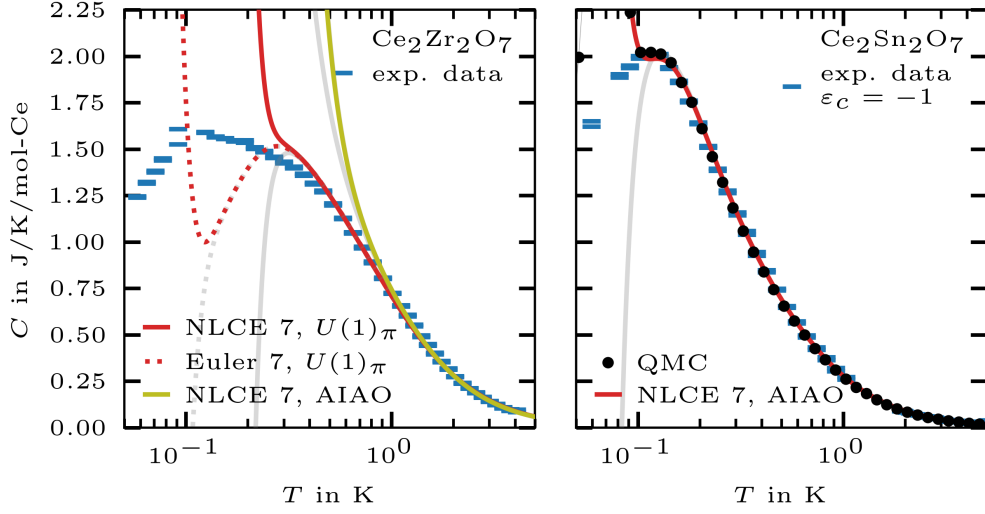


Figure 4.11: Comparison between the experiments on a single crystal for $\text{Ce}_2\text{Zr}_2\text{O}_7$ and $\text{Ce}_2\text{Sn}_2\text{O}_7$ and proposed exchange parameters of the heat capacity using seventh order NLCE. The systematic error in the specific heat for $\text{Ce}_2\text{Sn}_2\text{O}_7$ was included yielding an overall downshift $\varepsilon_C = -1$: $C_{\text{exp}} \rightarrow C_{\text{exp}} + \varepsilon_C \delta_{\text{sys}}$. The optimal exchange parameters for $\text{Ce}_2\text{Zr}_2\text{O}_7$ in the QSL $U(1)_\pi$ phase are $(J_a, J_b, J_c) = (0.064, 0.062, 0.01)$ meV (red, left) and in the AIAO phase are $(J_a, J_b, J_c) = (0.054, 0.052, -0.05)$ meV (yellow, left). Parameters predicted for $\text{Ce}_2\text{Sn}_2\text{O}_7$ are $(J_a, J_b, J_c) = (0.045, -0.001, -0.012)$ meV (red, right) located in the ordered regime. The gray lines indicate the convergence by displaying the sixth (fifths) order NLCE calculation for the red (yellow) curves. Note that the proposed AIAO parameters for $\text{Ce}_2\text{Sn}_2\text{O}_7$ lay within a sign-problem free regime, which allows comparison with QMC simulations performed by Benedikt Placke.

In contrast, $\text{Ce}_2\text{Sn}_2\text{O}_7$ reveals an isolated minimum located in the AIAO phase in close proximity to a $U(1)_0$ QSL. The optimal exchange constants are $(J_a, J_b, J_c) = (0.045, -0.001, -0.012)$ meV. The curve for $\text{Ce}_2\text{Sn}_2\text{O}_7$ is shifted to lower temperatures indicating smaller exchange parameters. The approximation for $\text{Ce}_2\text{Sn}_2\text{O}_7$ fully recovers the peak of the specific heat, which is also the limit of convergence. Note that the systematic error from the uncertainty of the sample mass introduces an additional fitting parameter, $\varepsilon_C = -1$ for the best dataset. The proposed parameter set is located in the sign-problem free AIAO phase, which enables QMC simulations to provide further insights into the low-temperature limit. Crucially, an ordered ground state induces a phase transition accompanied by a sharp peak in the heat capacity. However, neither $\text{Ce}_2\text{Zr}_2\text{O}_7$ nor $\text{Ce}_2\text{Sn}_2\text{O}_7$ indicates any sign of a possible ordering transition within the limits of the experiments. Extensive QMC simulations, performed by Benedikt Placke, around the optimal parameter determined by NLCE reveal a strong sensitivity to the critical temperature due to the proximity to the QSL phase. This suggests the existence of a phase transition below temperatures probed by experiment.

Magnetic susceptibility The heat capacity of both materials allows us to obtain elaborate constraints on exchange parameters determining a $U(1)_0$ QSL, $U(1)_\pi$ QSL, and an ordered AIAO ground states. However, it is insensitive to the form of magnetic moments formed microscopically. By applying a finite external field, the temperature-dependent magnetic susceptibility is sensitive to the magnetic moments and provides further insights into the pseudospin components. Hence, the same procedure as for the specific heat can be applied analogously to the magnetic susceptibility to resolve multipole order

Determining the magnetization and susceptibility is much more evolved for the pseudospin Hamiltonian compared to [Section 4.2](#) since eigenvalues do not refer to a fixed magnetization sector.

Since the local magnetic dipole associated with each pseudospin is parallel to the easy axis \mathbf{z}_i , *cf.* [Equation 4.18](#), the response to the magnetic field is not uniform throughout the lattice. Choosing a specific field direction makes the four sublattices non-equivalent. In particular, the magnetic field is orientated in $[1,1,1]$ -direction, yielding $\mathbf{h} \cdot \mathbf{z}_i = |\mathbf{h}|$ for one site and $\mathbf{h} \cdot \mathbf{z}_i = -\frac{1}{3}|\mathbf{h}|$ for the remaining three sites in the tetrahedron. This makes it necessary to incorporate color indices to the vertices for each arising cluster in the expansion. The number of topologically invariant clusters increases and the number of automorphisms for each cluster decreases, making computation more demanding. The directional dependency in spin space induces three independent permutations (abc) , (bac) and (bca) that have to be considered in the presence of an external field:

$$(J_x, J_y, J_z) = \{(J_a, J_b, J_c), (J_b, J_a, J_c), (J_b, J_c, J_a)\} \quad (4.26)$$

The magnetic moment exhibits an additional free parameter, the mixing angle θ . Different values of $\theta \in [0, \pi/2)$ have to be computed for each permutation. This covers all non-symmetry equivalent scenarios. The overall energy scale α is already fixed by the high-temperature tail of the heat capacity.

While the susceptibility was previously defined as the variance of the magnetization, *cf.* [Section 4.2](#), we determine it here by the derivative of the magnetization with respect to the external field strength. This is simpler to implement and further reflects the experimental procedure for measuring magnetic susceptibility. The total magnetization is defined by

$$m_{\text{DO}} = g_z \mu_B \sum_i \mathbf{e} \cdot \mathbf{z}_i (S_i^z \cos \theta + S_i^x \sin \theta). \quad (4.27)$$

The vector \mathbf{e} is normalized and aligned with the field in $[1, 1, 1]$ -direction. In the limit of small fields like $|\mathbf{h}| = 0.01 T$ in our case, the derivative of the magnetization is approximated by

$$\chi = c \frac{m_{\text{DO}}}{|\mathbf{h}|} \quad (4.28)$$

with $c = 9.65 \text{ emuT}^2/\text{mol-Ce/meV}$. The susceptibility was measured at higher temperatures

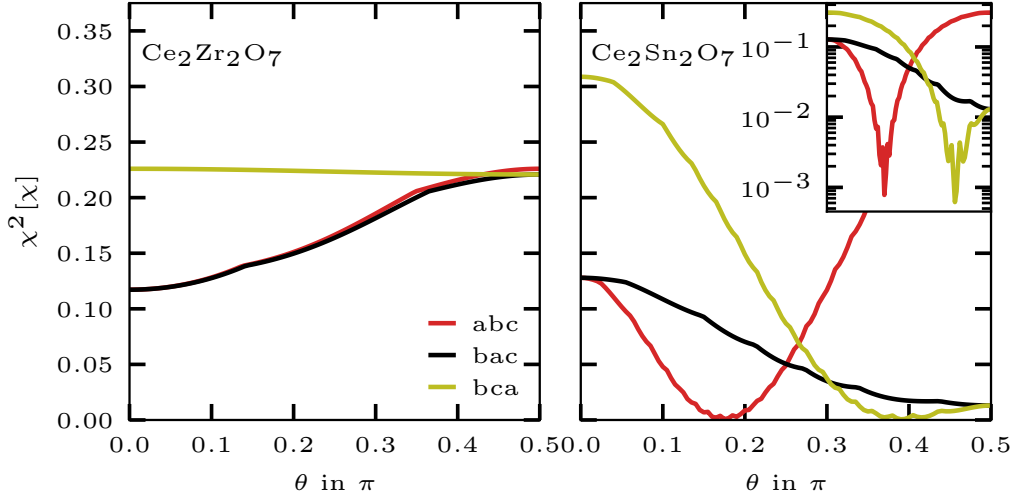


Figure 4.12: Goodness-of-fit $\chi^2[\chi]$ for the optimal parameters for $\text{Ce}_2\text{Zr}_2\text{O}_7$: $(J_a, J_b, J_c) = (0.064, 0.062, 0.01)$ meV, and $\text{Ce}_2\text{Sn}_2\text{O}_7$: $(J_a, J_b, J_c) = (0.045, -0.001, -0.012)$ meV.

~ 0.4 K than the heat capacity, and an expansion up to fourth order is sufficient as it is fully converged for the relevant temperatures. Hence, we define the NLCE data and its error by:

$$\chi_{\text{NLCE}} = (\chi_{\text{NLCE},4} + \chi_{\text{NLCE},3})/2 \quad (4.29)$$

$$\delta_{\text{NLCE}} = (\chi_{\text{NLCE},4} - \chi_{\text{NLCE},3})/2 \quad (4.30)$$

The experimental data, $\chi_{\text{exp}}(T) \pm \delta_{\text{unsys}}(T)$, do not exhibit any systematic error for $\text{Ce}_2\text{Zr}_2\text{O}_7$ nor $\text{Ce}_2\text{Sn}_2\text{O}_7$. Since the specific heat already fixes the overall energy scale, we consider the full temperature range to compute the goodness-of-fit

$$\chi^2[\chi] = \sum_{T_i} \frac{(\varepsilon_\chi \chi_{\text{NLCE}}(T_i) - \chi_{\text{exp}}(T_i))^2}{\varepsilon_\chi^2 \delta_{\text{NLCE}}(T_i)^2 + \delta_{\text{unsys}}(T_i)^2}. \quad (4.31)$$

Note that χ is used for both the susceptibility and goodness-of-fit. We introduce an additional scaling factor, $\varepsilon_\chi \in [0.5, 1.5]$, which is interpreted as an effective g -factor induced by single-ion physics or vacancies in the sample². The effective g -factor is obtained by $g'_z \rightarrow \sqrt{\varepsilon_\chi} g_z$ since $\chi_{\text{NLCE}} \propto g_z^2$. Similar to ε_C , ε_χ is chosen to minimize the goodness-of-fit.

For each permutation of $\{J_a, J_b, J_c\}$ defined in Equation 4.26 and different mixing angles $\theta \in [0, \pi/2)$, we determine the magnetic susceptibility according to Equation 4.28. Then we optimize $\varepsilon_\chi \in [0.5, 1.5]$ by minimizing $\chi^2[\chi]$. Using the optimized value, we obtain the goodness-

²Note that it is possible to systematically include the vacancies within NLCE by averaging over all disorder configurations for each cluster in the expansion [299, 3]. Simply scaling the NLCE results is a zeroth order approximation but valid for small disorder strengths, as expected in this case.

Compound	(J_x, J_y, J_z) in meV	θ	ε_χ
Ce ₂ Zr ₂ O ₇	(0.064, 0.062, 0.010)	0π	0.85
Ce ₂ Zr ₂ O ₇	(0.062, 0.064, 0.010)	0π	0.85
Ce ₂ Sn ₂ O ₇	(0.045, -0.001, -0.012)	0.18π	0.72
Ce ₂ Sn ₂ O ₇	(-0.001, -0.012, 0.045)	0.39π	0.72

Table 4.1: Optimal exchange parameters obtained from best-fit NLCE calculation from the specific heat and magnetic susceptibility.

of-fit according to Equation 4.31. Figure 4.12 shows the goodness for the optimal exchange parameter set (J_a, J_b, J_c) found for Ce₂Zr₂O₇ and Ce₂Sn₂O₇ based on the specific heat as a function of on the mixing angle θ . The optimal exchange parameters revealing the multipolar character are explicitly listed in Table 4.1. For Ce₂Zr₂O₇, two permutations $[(abc)$ and $(bca)]$ display a similar behavior since the optimal parameter set is close to a XXZ -Hamiltonian. One permutation has a dominant x component (dipolar) and the other one has a dominant y component (octupolar). Hence, Ce₂Zr₂O₇ is placed close to the boundary between a dipolar and octupolar $U(1)_\pi$ QSL with a mixing angle of $\theta \approx 0$. The corresponding scaling factor $\varepsilon_\chi = 0.85$ is consistent with the expected vacancies of 14% in the powder sample [245]. On the other side, the optimal parameters of Ce₂Sn₂O₇ exhibit two sharp minima for a finite value of θ $[(abc)$ and $(bca)]$. Both suggest a dipolar character since the y component is not dominant. The sharpness is illustrated by the logarithmic inset. Since we do not assume any vacancies for Ce₂Sn₂O₇, the scaling factor ε_χ describing the effective g -factor is associated with single-ion physics: $g_z^2 \propto \varepsilon_\chi$ yields $g'_z \approx 2.18$. The experimental measurements of the magnetic susceptibility and the optimal parameter sets are shown in Figure 4.13.

4.3.3 Conclusion

We find drastic differences during our analysis between both Cerium-based compounds, despite their similar chemical structure. Indeed, the only difference is the non-magnetic transition metal. Our analysis is based on novel neutron diffraction data at low temperatures, heat capacity, and magnetic susceptibility measurements. The optimal parameters obtained by combining the NLCE results from the heat capacity and the magnetic susceptibility are listed in Table 4.1.

This places Ce₂Zr₂O₇ in a dipolar $U(1)_\pi$ QSL phase but very close to the boundary to an octupolar character. In contrast, our analysis suggests an ordered dipolar AIAO ground state for Ce₂Sn₂O₇ in close proximity to a $U(1)_0$ QSL. Neutron diffraction data for both materials reveal strong similarities to the dipolar spin ice Ho₂Ti₂O₇.

The estimated microscopic parameters for Ce₂Zr₂O₇ reside close to a XXZ model. The measured heat capacity down to 0.058 K does not indicate a thermodynamic anomaly, and neutron data do not indicate any magnetic Bragg peaks. Both findings support the QSL scenario. The best-fit NLCE provides a good agreement for high and intermediate temperatures up to $T > 0.4$ K but fails to resolve the broad plateau as extrapolating to lower temperatures us-

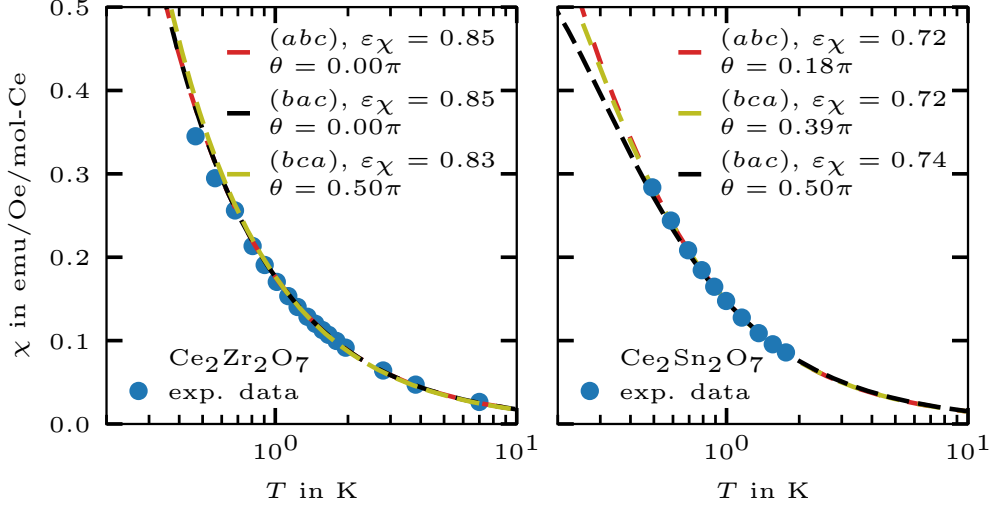


Figure 4.13: Magnetic susceptibility measurements for $\text{Ce}_2\text{Zr}_2\text{O}_7$ and $\text{Ce}_2\text{Sn}_2\text{O}_7$ on a powder sample and NLCE calculation up to order four for the optimal parameter sets and their permutations - $\text{Ce}_2\text{Zr}_2\text{O}_7$: (0.064, 0.062, 0.01) meV, and $\text{Ce}_2\text{Sn}_2\text{O}_7$: (0.045, -0.001, -0.012) meV.

ing Euler's transform suggests a narrow peak. Furthermore, we find qualitative agreement in the neutron diffraction data between the NLCE simulation and experiments in the SF channel. However, NLCE does not reproduce the data in the NSF channel. The observed zone boundary scattering in the NSF data is reminiscent of $\text{Ho}_2\text{Ti}_2\text{O}_7$, which is attributed to further neighbor interactions [207]. Both discrepancies, the NSF channel and the broad plateau, suggest additional weak couplings beyond the simulated nearest-neighbor XYZ -Hamiltonian.

In contrast, $\text{Ce}_2\text{Sn}_2\text{O}_7$ is placed in a dipolar AIAO-state similar to $\text{Nd}_2\text{Zr}_2\text{O}_7$ [300, 301], which is classically ordered. The proposed ferromagnetic transverse couplings enable QMC simulations to obtain insights into the low-temperature regime and resolve the expected phase transition. The proximity to a $U(1)_0$ QSL induces a strong sensitivity of the transition temperature. Although we do not have experimental evidence for a phase transition, we expect a thermodynamic anomaly below the experimentally accessible temperatures due to the constraints made by NLCE. Notably, the precise location ordered phase of the estimated parameters is classically unstable but stabilized by quantum effects. Therefore, $\text{Ce}_2\text{Sn}_2\text{O}_7$ experiences a quantum order-by-disorder mechanism as quantum fluctuations drive the classically disordered spin-ice phase into an ordered state. The strong similarities of \mathbf{Q} -dependency between $\text{Ce}_2\text{Sn}_2\text{O}_7$ and $\text{Ho}_2\text{Ti}_2\text{O}_7$ suggest a dipolar spin-ice regime above the AIAO-ordered state predicted by NLCE.

While the estimate for the Zr-compound is in agreement with other experiments [273] the hydrothermally grown Sn-sample is in stark contrast to the octupolar scattering observed previously for a solid-state synthesised sample [247]. The solid-state synthesised $\text{Ce}_2\text{Sn}_2\text{O}_7$ suggests an $U(1)_\pi$ QSL state in the octupole sector contradicting our findings. The reported diffuse

scattering at large momentum ($|\mathbf{Q}| > 5 \text{ \AA}^{-1}$) is attributed to an octupolar character [287]. In contrast, the hydrothermally grown sample only shows scattering at small momentum peaked around $|\mathbf{Q}| \approx 0.5 \text{ \AA}^{-1}$ and diffusive scattering beyond 2 \AA^{-1} is absent, *cf.* Figure 4.8b. It is more reminiscent of dipolar spin-ice observed for $\text{Ho}_2\text{Ti}_2\text{O}_7$. The incompatible conclusions raise questions about the role of disorder and the influence of the synthesis technique: *hydrothermal* versus *solid-state* synthesis.

Disorder in pyrochlore magnets places undoubtedly a significant role as it strongly affects the ground-state selection. This is well known for $\text{Yb}_2\text{Ti}_2\text{O}_7$ [302, 303, 304, 305, 306, 307]. These effects are also expected in Cerium as it has two stable oxidation states: Ce^{3+} (magnetic) and Ce^{4+} (non-magnetic). However, detailed analysis using neutron structure refinement atomic pair distribution function (PDF) measurement does not detect any sign of oxidation or other disorder in the hydrothermally grown samples. Resolving these contradictions calls for further studies aiming at the effect of synthesis techniques and the role of disorder in Cerium-based pyrochlores.

Our analysis reveals similarities but also stark differences for both compounds suggesting a strong influence of the transition metal: tin versus zirconium. Both materials are placed close to phase boundaries which is not uncommon for pyrochlores oxides [132, 308, 309, 310, 311, 312, 292]. This opens up the possibility of stabilizing various phases by disorder or pressure. The small value of $\theta \approx 0\pi$ for $\text{Ce}_2\text{Zr}_2\text{O}_7$ explains the (almost) complete absence of single-magnon spin wave branches in elastic neutron scattering measurements at zero field and a suppressed response to an external field. In contrast, the finite value for $\text{Ce}_2\text{Sn}_2\text{O}_7$ implies a single-magnon response in the zero and finite field case [313] and has to be investigated in future studies. The consequences of disorder and the impact of next-nearest-neighbor interactions, as observed for $\text{Ho}_2\text{Ti}_2\text{O}_7$ [207], have to be investigated further to arrive at a definite understanding of Cerium-based pyrochlore magnets. Also, the experiments and the numerical methods were performed at finite temperatures raising the question of how reliable the ground state can be predicted. To the extent that further interaction, disorder and finite-temperature effects do not affect the ground-state selection, our analysis provides substantial constraints for possible exchange parameters. Despite the uncertainties, it can be safely stated that the wealth of exotic phenomena associated with dipolar-octupolar pyrochlores [217, 239] is present for Cerium-based compounds.

Both projects demonstrate the applicability of NLCE and call for its broader use in the quantitative modeling of quantum magnets. While the ground state is known for ferromagnetic transverse couplings, its nature for antiferromagnetic transverse couplings, like predicted for $\text{Ce}_2\text{Zr}_2\text{O}_7$, is largely explored using uncontrolled methods, *cf.* Figure 4.7, making reliable predictions impossible. Approaches aiming at the zero temperature limit of the fully frustrated pyrochlore Heisenberg antiferromagnet are presented in the following chapter.

Note that the optimal parameters for $\text{Ce}_2\text{Zr}_2\text{O}_7$ slightly differ from the publication [3] due to additional computations. Benedikt Placke conducted the MC simulations, and Dr. Owen Benton computed the structure factor. Experiments were led by Evan Smith and Dr. Danielle Yahne.

Chapter 5

... AND ZERO TEMPERATURE

The ground state of the quantum pyrochlore Heisenberg antiferromagnet is even less accessible than its thermodynamics. Despite tremendous efforts during the past decades, remarkably little definite is known about the fully frustrated regime beyond the perturbative description of QSI. The absence of controlled and unbiased methods yields a *zoo* of possible ground-state candidates, including various QSLs [221, 222, 168, 223, 242, 169, 224, 185, 135] as well as several sometimes quiet exotically ordered states [225, 314, 226, 227, 228, 229, 231, 232, 233, 183, 315, 185, 135, 234, 2, 95, 4, 6].

This chapter focuses on the most frustrated and least accessible point in the phase space: the isotropic Heisenberg model. Approaching the model from the finite temperature in [Section 4.2](#) reveals a large residual entropy far below the Schottky anomaly within the limit of convergence, making the exotic phenomena associated with frustration in three dimensions possible.

Motivated by the great success on the kagomé lattice [316, 317, 318, 319, 320], the first section presents extensive and controlled DMRG calculations that provide a reliable estimate of the ground-state energy for the first time. Strikingly, the calculation detects a robust spontaneous inversion symmetry breaking expressed by an energy difference on the tetrahedral sublattice, which is stable across finite clusters up to 128 sites – unprecedented in three dimensions [2]. The second section is in a spirit similar to the first section as the applied methodology is analogous but considers the magnetization process in an external magnetic field. Again, DMRG detects a stable 1/2-magnetization plateau breaking the rotational symmetry of the model [4]. The last section is conceptually the most interesting as it introduces a family of valence-bond crystals – exponentially numerous in linear system size – taking the form of hard-hexagon coverings. Besides a competitive ground-state energy, which is valid in the thermodynamic limit, the hard-hexagon crystals suggest a change in perspective on frustrated quantum magnets [6]. The discoveries presented in this chapter suggest a transition into a symmetry-broken state at low temperatures, thereby contradicting the prominent spin-liquid assumption.

5.1 Possible inversion symmetry breaking

Possible Inversion Symmetry Breaking in the $S = 1/2$ Pyrochlore Heisenberg Magnet

[Phys. Rev. Lett. 126, 117204 \(2021\)](#)

I. Hagymási, R. Schäfer, R. Moessner, and D. J. Luitz

Despite the great success of DMRG in the two-dimensional kagomé Heisenberg antiferromagnet [316, 317, 318, 319, 320], we still lack comparable advances in three dimensions. While highly optimized ED methods are limited to roughly 48 sites [107] corresponding to $2 \times 2 \times 3$ unit cells in the three-dimensional pyrochlore, we demonstrate that extensive DMRG calculations are capable of providing reliable insights into clusters with up to 128 sites with full periodic boundary conditions. In agreement with earlier perturbative treatments [225], our results reveal a spontaneous inversion symmetry breaking contradicting the spin liquids assumption at zero temperature. The observed energy density difference on the tetrahedral sublattice reflects the inability of two corner-sharing tetrahedra to host singlet states simultaneously. A careful finite-size scaling allows for a precise estimate of the ground-state energy: $E_0/N = -0.490(6) J$. This is supported by a complementary extrapolation of the NLCE data from Section 4.2 to zero temperature, which rules out several estimates from the literature [226, 183, 315, 261].

5.1.1 Model and Methods

As illustrated in the previous chapters, frustrated three-dimensional models provide a fertile ground for exotic physics but are hardly accessible to numerical methods. We are interested in the zero-temperature properties of the isotropic antiferromagnetic Heisenberg model on the pyrochlore lattice as studied in Section 4.2

$$H = J \sum_{ij} \mathbf{S}_i \cdot \mathbf{S}_j. \quad (5.1)$$

The sign-problem and the limitation of ED require the use of approximate methods like DMRG, which has become the method of choice to study strongly correlated systems in one dimension [83, 84, 321, 86, 87]. Extensive research made the application to two-dimensional systems such as the kagomé lattice possible and revealed the great capabilities of this method [316, 317, 318, 319, 94, 320]. By extending the originally one-dimensional technique to the three-dimensional pyrochlore, we demonstrate the recent advances in computational physics by studying clusters up to 128 sites with periodic boundary conditions. We obtain reliable results for clusters with $N = 32, 48, 64, 108, 128$ sites (defined in Table 5.1) far beyond the reach of ED, which only considered 36 sites in the pyrochlore [322]. The clusters exhibit either full cubic or an increased or reduced set of point group symmetries compared to the full pyrochlore lattice. As in two dimensions, the system is linearized by a one-dimensional “snake” path introducing long-range

cluster	\mathbf{v}_1	\mathbf{v}_2	\mathbf{v}_3	length
32	$2\mathbf{a}_1$	$2\mathbf{a}_2$	$2\mathbf{a}_3$	4
48a	$(\frac{3}{2}, \frac{1}{2}, 0)^T$	$(0, 1, 1)^T$	$(0, 1, -1)^T$	4
48b	$(\frac{3}{2}, \frac{1}{2}, 0)^T$	$(0, \frac{1}{2}, \frac{3}{2})^T$	$(0, 1, -1)^T$	4
48c	$(\frac{3}{2}, 1, \frac{1}{2})^T$	$(0, 1, -1)^T$	$(1, -1, 0)^T$	4
48d	$(1, 1, 1)^T$	$(1, 0, -1)^T$	$(1, -1, 0)^T$	4
64	$(1, 1, 1)^T$	$(1, 1, -1)^T$	$(-1, 1, 1)^T$	6
108	$3\mathbf{a}_1$	$3\mathbf{a}_2$	$3\mathbf{a}_3$	6
128	$(2, 0, 0)^T$	$(0, 2, 0)^T$	$(0, 0, 2)^T$	8

Table 5.1: Vectors \mathbf{v}_1 , \mathbf{v}_2 , and \mathbf{v}_3 framing the eight clusters considered in Section 5.1 and Section 5.2. The last column describes the minimal length of non-physical resonance loops induced by periodic boundaries. The clusters of sizes 32 and 108 respect all lattice symmetries. The lattice vectors are defined in the caption of Figure 3.1.

interactions. The growing entanglement, induced by this one-dimensional topology, is captured by an increasing bond dimension χ . The calculation exploits the $SU(2)$ -invariance and contains up to $\chi_{\max} = 20\,000$ $SU(2)$ -symmetric states [323, 324, 325, 326] roughly equivalent to 80 000 $U(1)$ states. The convergence is improved by minimizing the bandwidth of the connectivity matrix [85, 327, 1]. If possible¹, the final energy is obtained by extrapolating the two-site variance for each cluster [328]. Besides precisely determining the ground-state energy, we further calculate the spin structure factor and excitations.

5.1.2 Results

Enlarging the variational manifold by systemically increasing the bond dimension allows for a controlled estimate of the ground-state energy. Hence, pushing the DMRG simulation to a high bond dimension makes a controlled calculation on the pyrochlore in three dimensions possible. The final ground-state energy in the thermodynamic limit is obtained by extrapolating the two-site variance for a specific cluster and extrapolating the cluster sizes. The extrapolated ground-state energies and excitations (if accessible) for all eight clusters are listed in Table 5.2. Their extrapolation to the thermodynamic limit is shown Figure 5.1a. The ground-state energy strongly depends on the cluster size and its geometry indicated by a monotonic growth, which is attributed to pronounced finite-size effects. Even by pushing state-of-the-art numerics to $N > 100$ sites, the linear dimension only scales by $N^{1/3}$, inducing competing non-physical resonance loops through the periodic boundaries. In the bulk, the low-energy physics is determined by hexagonal loops. However, only the largest cluster considered here, $N = 128$, does not incorporate competing non-physical loops of size six from periodic boundaries, cf. Table 5.1. Hence, smaller clusters exhibit lower energies due to these resonance loops, which were particularly influential for clusters of size $N \lesssim 48$. The finite-size scaling $1/N$ suggests a quadratic fit to obtain the thermodynamic

¹Two-site DMRG was used for $\chi \leq 2000$ and one-site DMRG for larger bond dimensions. For $N = 108$, we fall back to two-site DMRG for larger χ , and the extrapolation is based on the truncation error.

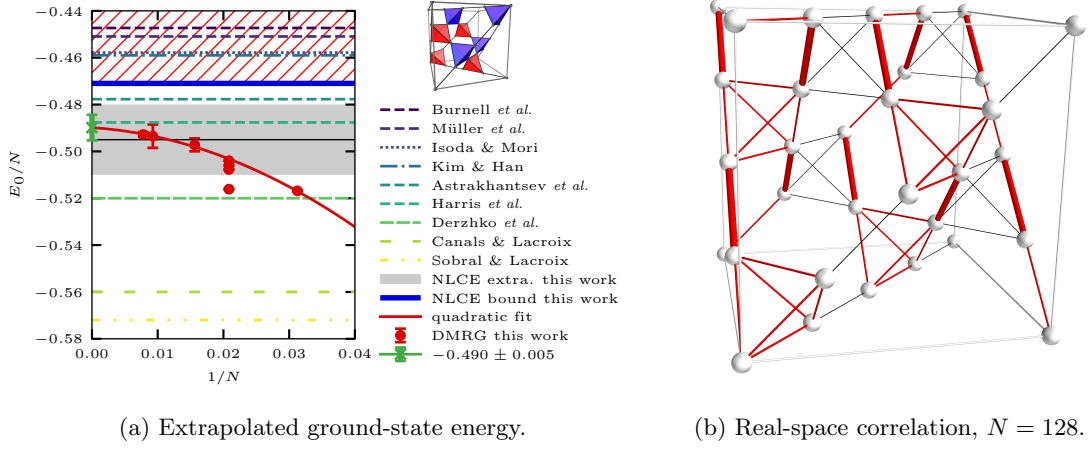


Figure 5.1: (a) Finite-size scaling of the extrapolated ground-state energies for different cluster sizes and geometries ($J = 1$). The DMRG results for periodic clusters are extrapolated to infinite bond dimension using a quadratic polynomial. Converged NLCE results from a tetrahedron-based expansion up to order eight ($T_{\text{conv}} \gtrsim 0.25$) define an upper bound ruling out energies above $E_{\text{bound}} = -0.471$ (blue line). Extrapolating the NLCE results to zero temperature yields an estimate for the ground-state energy, $E_{\text{NLCE}} = -0.495 \pm 0.01$, (black line). The confidence interval is shown in gray. The results are compared to different literature results: Burnell *et al.* -0.4473 [315], Müller *et al.* -0.4509 [261], Isoda and Mori -0.4578 [226], Kim and Han -0.459 [183], Astrakhantsev *et al.* -0.477 [234], Harris *et al.* -0.487 [225, 229], Derzhko *et al.* -0.52 [272], Canals and Lacroix -0.56 [222], Sobral and Lacroix -0.572 [314]. The plot in the upper right corner highlights the tetrahedral sublattice. (b) Real-space spin correlation of the ground state for $N = 128$ truncated to a cubic cluster. The thickness of the red bonds corresponds to their magnitude. The black lines indicate negligible correlations.

limit $1/N \rightarrow 0$. Gaussian resampling based on the DMRG error bars allows for estimating the confidence interval² $E_0/N = (-0.4898 \pm 0.0057) J$.

The excitation analysis, only possible for $N \leq 48$, suggests a finite triplet gap while the singlet gap is one order of magnitude smaller and potentially unstable. The reduced lattice symmetries for the clusters with $N = 48$ and strong finite-size effects induced by the periodic resonance loops do not allow a sophisticated analysis. However, the scenario of a finite triplet gap is compatible with predictions in Ref. [227, 231, 234, 6].

The finite-temperature NLCE data from Section 4.2 provides a complementary approach. The tetrahedron-based expansion up to the eighth order does not allow direct insight into the zero-temperature regime but provides unbiased results for the thermodynamic limit at finite temperature $T_{\text{conv}} \gtrsim 0.25 J$. This already admits an educated guess using a quadratic extrapolation to zero temperature and defines an upper bound for the ground-state energy as it is a monotonically decreasing function with temperature. The extrapolated energy, $E_{\text{NLCE}} = (-0.495 \pm 0.01) J$, lies within the error bars of the DMRG calculations. Importantly, the converged data at $T \approx 0.25 J$

²The fit only includes cluster $48d$, as it is most consistent.

Cluster	GS energy	Singlet gap	Triplet gap
32	-0.5168	0.0318	0.6872
48a	-0.5161	0.2166(4)	0.6709(4)
48b	-0.5077	0.027(2)	0.554(2)
48c	-0.5060(1)	0.053(7)	0.42(2)
48d	-0.5040(5)	0.06(3)	0.36(3)
64	-0.4972(25)	—	—
108	-0.4935(50)	—	—
128	-0.4928(10)	—	—

Table 5.2: Extrapolated ground-state energy, singlet, and triplet excitations for different clusters with periodic boundary conditions.

defines an unbiased upper bound, $E_{\text{bound}} = -0.471 J$, and thereby rules out several predictions from the literature [226, 183, 315, 261]. The energy per site up to order eight in the tetrahedron-based expansion, including non-trivial hexagonal and octagonal loops, is shown in Figure 5.2a.

Besides the precise determination of the ground-state energy, we present strong numerical evidence for a spontaneous inversion symmetry breaking. Carefully evaluating the real-space correlations reveals a breathing instability reflected as an energy density difference between both tetrahedral sublattices shown in Figure 5.1b. One tetrahedral sublattice (A-type) of the tetrahedron exhibits two strongly anticorrelated dimers on opposite edges, while the other (B-type) exhibits weak uniform correlations. The two strong bonds exhibit a correlation strength of $\sim -0.53 J$; they are only weakly coupled with another $\sim -0.01 J$. The uniformly correlated B-type tetrahedra have a correlation of $\sim -0.15 J$. The values are obtained from the best variational wavefunction of the $N = 128$ cluster. The precise pattern depends on the cluster size, its geometry, and the chosen snake path. The *cleanest* pattern (and best convergence for the larger clusters) is found for the largest cluster. We attribute this to the absence of competing non-physical resonance loops across the periodic boundaries, as they are of size eight in this case. Smaller clusters host periodic loops with even smaller circumferences than the bulk (hexagon of length six).

It is well known that DMRG has biases towards low entanglement and ordered states and is influenced by the one-dimensional topology of the snake path. Therefore, we carried out a careful analysis to prove that the symmetry broken state is intrinsic and not an artifact of the path and the finite bond dimension. Similar to a pinning field, a breathing anisotropy is applied to enhance the couplings on one sublattice and reduce the couplings on the other: $J \rightarrow J \pm \varepsilon$. The selection process between both broken states associated with the spontaneous symmetry breaking is illustrated in Figure 5.2b and is controlled by $\varepsilon \rightarrow -\varepsilon$. The order parameter corresponding to the inversion symmetry is the squared total spin on one tetrahedral sublattice, which essentially encodes the tetrahedral energy density, cf. Equation 4.17. An extrapolation of the order parameter for the 64-cluster yields $(\sum_{i \in \text{A-type}} \mathbf{S}_i)^2 = 1.211 \pm 0.068$ and $(\sum_{i \in \text{B-type}} \mathbf{S}_i)^2 = 0.819 \pm 0.037$.

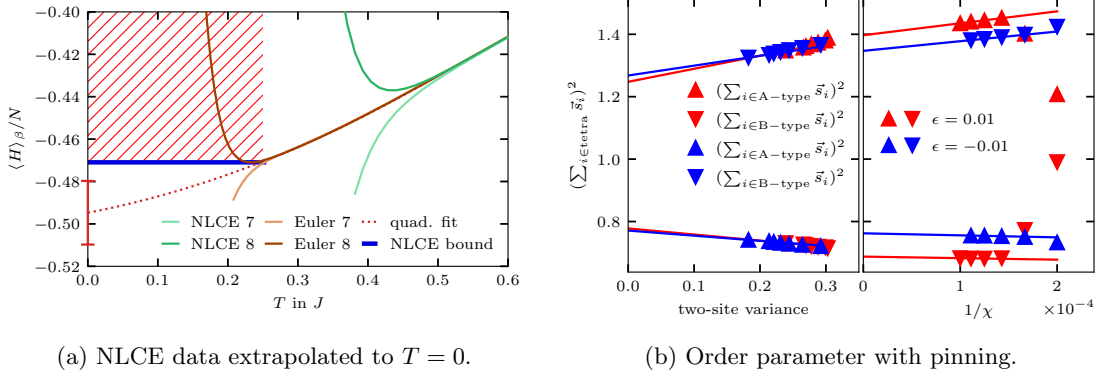


Figure 5.2: (a) Converged NLCE results (tetrahedron expansion, eighth order) defining an upper bound, $E_{\text{NLCE}} = -0.471 J$, and allow the extrapolation to zero temperature via a quadratic fit: $E_{\text{extra}} = (-0.495 \pm 0.01) J$. (b) Order parameter to detect spontaneous inversion symmetry breaking in the pyrochlore. We show the extrapolated energy density on the A- and B-type tetrahedra separately in the presence of a symmetry-breaking pinning field: $H = (1 - \epsilon)H_A + (1 + \epsilon)H_B$. The left (right) panel shows data for the cluster with $N = 64$ ($N = 108$).

Symmetry-breaking manifests itself in the spin structure factor:

$$S(\mathbf{Q}) = \frac{4}{3N} \sum_{ij} \langle \Psi_0 | \mathbf{S}_i \cdot \mathbf{S}_j | \Psi_0 \rangle \cos[\mathbf{Q} \cdot (\mathbf{R}_i - \mathbf{R}_j)] \quad (5.2)$$

It is evaluated for different lattice sizes, $N = 32, 64, 108, 128$, in Figure 5.3. In principle, it is accessible in neutron experiments as done in Section 4.3 – if a pyrochlore $S=1/2$ Heisenberg material would be available in nature. The upper/lower panels refer to the $(H, H, L)/(H, L, 0)$ scattering profile. Figure 4.5 shows both scattering planes at finite temperature for a cluster with 48 sites and reveals both similarities and discrepancies. Bowties, a hallmark for pyrochlores [225, 221, 160, 261, 254, 277], are well recognizable. The different structure of 64 site cluster is attributed to its reduced symmetry. The larger clusters exhibit a drastic change compared to smaller clusters in the $(H, L, 0)$ plane, reflecting the broken symmetry.

5.1.3 Conclusion

The three-dimensionality and its frustration make the pyrochlore antiferromagnet inaccessible for most approaches and only little definite is known despite decades of intense research. Extensive $SU(2)$ -DMRG calculations make it possible to obtain reliable results for clusters up to 128 sites, which do not exhibit competing hexagonal winding loops induced by the periodicity. We extended the great achievement of DMRG in the two dimensions to this long-standing problem and demonstrated the applicability of DMRG to strongly correlated problems in three dimensions. Although two approximations are used to derive the final ground-state energy, extrapolation to infinite bond dimension and extrapolation to the thermodynamic limit, the careful

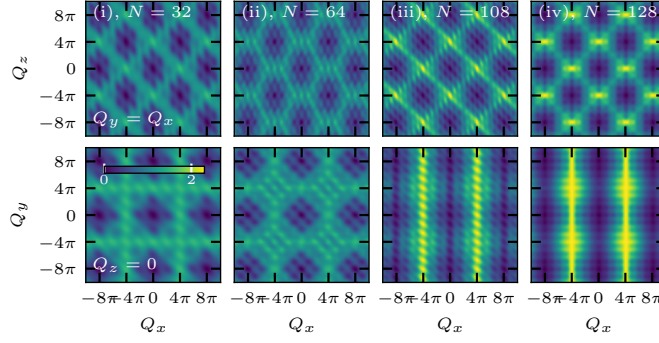


Figure 5.3: Spin structure factor in (H, H, L) and $(H, L, 0)$ plane for $N = 32, 64, 108, 128$ sites using $\chi = 20\,000, 16\,000, 16\,000, 12\,000$, respectively.

analysis provides a precise estimate firmly ruling out several theoretical proposals. Besides the estimate, previously unavailable *cf.* Figure 5.1a, strong evidence for a broken inversion symmetry in the ground state of the $S = 1/2$ pyrochlore Heisenberg antiferromagnet is presented. The symmetry-broken state violates the QSL assumption at zero temperature; hence, the findings suggest a transition from a finite-temperature liquid regime into an ordered state. The derived DMRG estimate in the thermodynamic limit is consistent with extrapolated NLCE data to zero temperature within error bars, which additionally provides an upper bound on the ground-state energy.

The strong dimer correlations observed in the A-type tetrahedra are reminiscent of the singlet ground states on a tetrahedron which motivates several perturbative approaches. Notably, our ground-state energy agrees well with the perturbative pioneering result by Harris, Berlinsky, and Bruder from three decades ago [225]. The idea, also studied by others [226, 221, 227, 228], naturally discards the lattice inversion by reducing all bond strengths on one tetrahedral sublattice, the B-type, similarly to a breathing anisotropy denoted by λ . The limit $\lambda = 0$ yields fully uncoupled and isolated tetrahedra exhibiting two degenerated singlet ground states. A finite perturbation, $\lambda > 0$ on the B-type bonds, is examined by an effective Hamiltonian defined on the degenerate subspace. The resulting effective Hamiltonian is diagonal up to third order, which is solved by a mean-field approach yielding $E_0/N = -0.487 J$ [225]. The proposed dimer covering [225, 227] is consistent with the observed correlation pattern in Figure 5.1b. Hence, their first pioneering approach might be closer to the solution to this long-standing and much-studied problem than expected during the last decades. The dimerization tendencies was observed numerically by other methods afterwards [234, 329].

Dr. Imre Hagymási performed the DMRG calculation.

5.2 Magnetization process and ordering

Magnetization process and ordering of the $S = 1/2$ pyrochlore Heisenberg antiferromagnet in a magnetic field

[Phys. Rev. B 106, L060411 \(2022\)](#)

I. Hagymási, R. Schäfer, R. Moessner, and D. J. Luitz

Frustrated magnets exposed to an external magnetic field are similarly inaccessible but also experience the same wealth of exotic and conventional magnetic phases of matter [330]. Due to the computational complexity, the magnetization process is largely unexplored in the pyrochlore $S = 1/2$ Heisenberg antiferromagnet. Extending the methodology applied in the last section allows sophisticated insights into its magnetic properties at zero temperature. Targeting individual magnetization sectors using large-scale DMRG reveals a pronounced half-magnetization plateau that breaks the lattice's rotational symmetry. Continuing the careful analysis of the bond dimension and different clusters provides strong evidence that the corresponding magnetization plateau is stable in a finite range of magnetic field strengths in the thermodynamic limit. An analogous state, known as kagomé ice [331, 332, 333], is known in spin ice, where the symmetry-breaking is not spontaneous, suggesting a responsible quantum order-by-disorder mechanism in the Heisenberg case. The magnetization jump at the saturation field is consistent with a magnon crystal description equivalent to the kagomé lattice but potentially unstable in the thermodynamic limit. Magnetic properties such as magnon crystals and magnetization plateaus are frequently studied in frustrated magnets [334, 335, 336, 337, 338, 339, 340, 341, 342, 343, 344, 345, 346, 111, 347].

5.2.1 Model and Methods

Particularly little is known about the magnetization process of pyrochlore [348, 337, 349, 350, 330, 351, 347]. Its two-dimensional relative, the kagomé Heisenberg antiferromagnet, is far more accessible by ED and MPS methods allowing detailed insights into the magnetic properties [334, 336, 338, 341, 343, 342, 344, 345, 352, 353, 111, 346]. The applied methodology is similar to [Section 5.1](#) but additionally includes an external field in [001] direction:

$$H = J \sum_{ij} \mathbf{S}_i \cdot \mathbf{S}_j - h \sum_i S_i^z. \quad (5.3)$$

The XXZ -Hamiltonian conserves the total magnetization, $S_{\text{tot}}^z = \sum_i S_i^z$, such that each symmetry sector corresponds to a fixed magnetization eigenvalue $m_z = -N/2, \dots, N/2 - 1, N/2$. Using $SU(2)$ and $U(1)$ DMRG we determine the ground-state energies for all clusters defined in [Table 5.1](#) for different magnetization sectors m_z . As done in [Section 4.2](#), the ground-state energies $E_m^0(h = 0)$ are determined in each sector for $h = 0$ and a finite field is included via: $E_m^0(h) = E_m^0(0) - hm$.

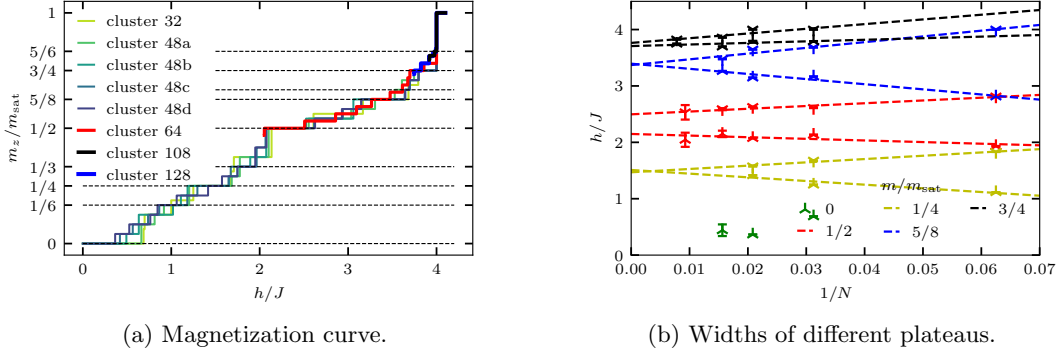


Figure 5.4: (a) Magnetization curve for different cluster sizes and geometries at zero temperature. Full magnetization curves are only accessible for smaller clusters. (b) Extrapolation to the thermodynamic limit using a linear fit in $1/N$ for different magnetization plateaus. We additionally include a periodic cluster with $N = 16$ sites.

While the ground state in the zero-field case is spin singlet with zero magnetization, the magnetization of the ground state monotonically increases with increasing field strength. This happens precisely when energies of two adjacent sectors agree for a critical value of h . The jump from sector m to m' occurs at

$$E_m^0 - hm = E_{m'}^0 - hm' \quad \Rightarrow \quad h = \frac{E_m^0 - E_{m'}^0}{m - m'}. \quad (5.4)$$

Note that multiple transitions can occur simultaneously, inducing a larger jump in the magnetization of the ground state. The final ground-state energy is obtained by extrapolating the truncated error or variance [323, 87, 324, 325, 326, 328].

5.2.2 Results

A robust gap of adjacent magnetization sectors in the thermodynamic limit yields a stable magnetization plateau whose width is proportional to the gap size, *cf.* Equation 5.4. In contrast, the absence of a gap in the thermodynamic limit induces a smooth and continuous increase of the magnetization in the sample. This leads to the characteristic magnetization curve shown in Figure 5.4a for the pyrochlore antiferromagnet evaluated for various clusters sizes and geometries. The ground state is fully polarized, $m_z/m_{\text{sat}} = 1$, for sufficiently large fields. The saturation field marks the jump to the fully polarized state, $h_{\text{sat}} = 4J$.

Equivalently to the kagomé lattice [335, 330], the ground state in high magnetic fields is described by a magnon crystal responsible for the saturation jump. This is one of the rare cases where analytic solutions for an interacting quantum many-body system can be constructed. A single magnon contains one magnetic excitation and reduces the energy by $4J$ compared to the fully polarized state. Magnons are localized on non-overlapping and non-neighboring hexagons,

meaning that at least one site separates adjacent magnon excitations. Therefore, magnons are energetically favored over the ferromagnetic state for field strengths below $h_{\text{sat}} = 4 J$. The densest packing of non-overlapping magnons requires three unit cells (12 sites) which can be placed on parallel kagomé planes. Each localized magnon exhibit one magnet excitation (compared to the fully polarized state) yielding the $m_z/m_{\text{sat}} = (11 - 1)/12 = 5/6$ plateau. While the predicted saturation field is consistent with Figure 5.4a, only a few clusters are commensurable (*e.g.* $N = 108$) with the densest magnon tiling. The resulting 5/6-plateau is very slim and potentially unstable in the thermodynamic limit.

The influence of periodic winding loops is even more severe than in the non-magnetic case, as they allow extremely dense magnon packings in smaller clusters. The circumferences of these non-physical magnons living on periodic winding loops can be smaller than six (*e.g.* four). Hence, they are not representative in the thermodynamic limit, and induce an artificial 3/4-plateau for clusters of size 32 or 48.

Besides the saturation jump at $h_{\text{sat}}/J = 4$, the $m/m_{\text{sat}} = 1/2$ -plateau seems to be stable across all cluster sizes. Other features strongly depend on the specific cluster and are likely to be unstable in the thermodynamic limit. We analyze the stability of various plateaus by extrapolating their width using a linear fit in $1/N$ as visualized in Figure 5.4b. Except for $m_z/m_{\text{sat}} = 1/2$, It indicates the instability of all plateaus as their width goes to zero for $N \rightarrow \infty$. Indeed, it provides evidence (red lines) for a robust 1/2-plateau in the thermodynamic limit located within $h_-^{1/2} \leq h \leq h_+^{1/2}$ with $h_-^{1/2} = 2.16 J$ and $h_+^{1/2} = 2.48 J$.

The triplet gap in the thermodynamic limit determines the zero-magnetization plateau. Obtaining a reliable estimate for the gap (and therefore its width) is not possible as it varies non-monotonically with cluster size. However, the predicted triplet gap of the 64-sites cluster, $\sim 0.42 J$, is consistent with variational MC simulations predicting a gap of $\sim 0.40 J$ in the thermodynamic limit [234]. Both estimates are further consistent with a recent estimate [6] on the ruby lattice $\sim 0.36 J$; the connection between the pyrochlore and the ruby lattice is discussed in the following section. The finite gap suggests a stable non-magnetic plateau for small but finite field strengths.

We further investigate the structure of the 1/2-magnetization plateau. While the ground state of smaller clusters like $N = 32$ exhibit a uniform magnetization, $\langle \Psi_0 | S_i^z | \Psi_0 \rangle = 0.25$, larger clusters develop a distinct magnetic order. It reveals a 3 : 1 spin polarization ratio restricted to alternating kagomé and triangular (not connected) planes as visualized in Figure 5.5a. The pattern breaks the rotational symmetry of the lattice. The alternating layers can be orientated in four directions, each corresponding to a single spin of the tetrahedral unit cell, which forms the intermediate triangular layer. Therefore, each tetrahedral unit cell contributes three spins to the triangular unit cell in the kagomé layer and the remaining apex spin participates in the intermediate triangular layer. Due to the absence of competing winding loops, the cleanest pattern was obtained for the 128-sites cluster yielding an average magnetization on the polarized kagomé planes of 0.43 and -0.28 on the anti-polarized triangular planes. Smaller clusters exhibit

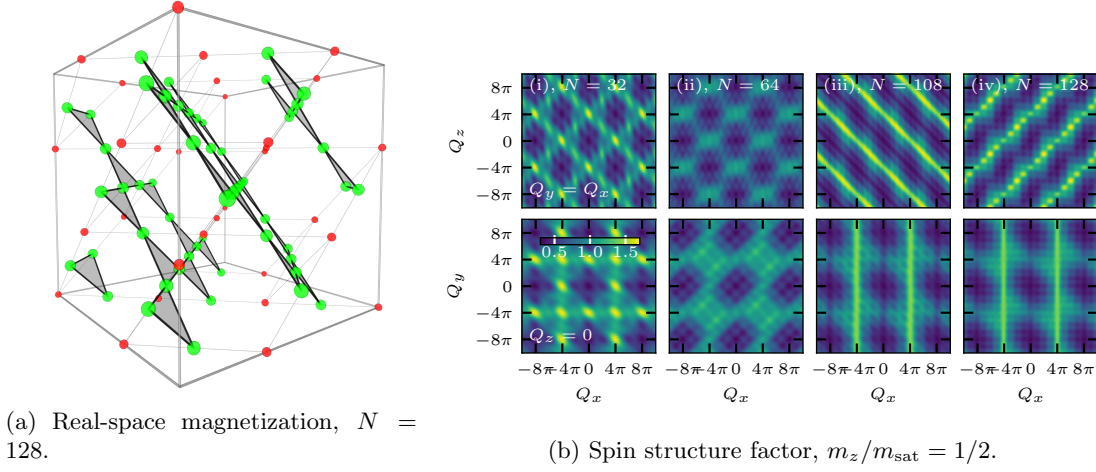


Figure 5.5: (a) Real-space magnetization for the $N = 128$ cluster truncated to a cubic cell. The radius of the balls is proportional to the on-site magnetization, $\langle \Psi_0 | S_i^z | \Psi_0 \rangle$. The color corresponds to the sign. The gray triangles highlight the alternating kagomé planes. (b) Spin structure factor in (H, H, L) and $(H, L, 0)$ plane.

defects in the form of non-magnetic chains passing through the planes, which are attributed to non-physical resonance loops induced by periodic boundaries.

The symmetry breaking of the plateau state is different from the previously found in [Section 5.1](#). Unlike the zero-field case, where the inversion symmetry, encoded via energy difference on the tetrahedral sublattice, is broken, the plateau state is invariant under inversion. It breaks the rotational symmetry where the rotational axis is not perpendicular to the planes. The broken symmetry is further encoded in the spin structure factor, *cf.* [Equation 5.2](#), in [Figure 5.5b](#). Similar to the zero-field case, the symmetries for smaller clusters appear intact.

5.2.3 Conclusion

For the pyrochlore magnet, one of the central questions – in zero and non-zero fields – is the existence of a spin liquid and its competition with possible (sometimes quite exotic) ordered phases. Like the zero-field case, the pyrochlore Heisenberg antiferromagnet in a field is equally inaccessible but exhibits similar phenomena associated with frustrated magnets. We provide evidence for a robust half-magnetization plateau that is stable in the thermodynamic limit and breaks the lattice rotation. The observed 3 : 1 ratio of oppositely polarized spins is not surprising as it is the only way to obtain a half-magnetized tetrahedron for Ising spins. However, the formation of the specific pattern expressed via alternating kagomé and triangular planes is surprising, taking into account the exponentially many possible 3 : 1 configurations. Mapping the tetrahedral sublattice to a diamond lattice allows the identification of valid configurations by a hard dimer covering where a dimer is associated with a negatively polarized spin shared among two tetrahedra. This

yields a residual entropy of $S \approx 0.13k_B$ [202, 354, 355]. Order-by-disorder drives the selection process towards specific configurations over others through fluctuations [24, 356, 357, 158]. Selecting the layered structure is reminiscent of a quantum order-by-disorder mechanism.

The observed plateau state is similar to kagomé ice, but its origin is different. As the layered structure in the quantum case arises spontaneously selected from an exponentially large configuration space, kagomé ice is encoded in the Hamiltonian. Spin-orbit coupling is responsible for an Ising anisotropy in pyrochlore materials, *cf.* Section 3.3 or Section 4.3. The local easy-axis transforms the uniform magnetic field into a staggered Zeeman term acting differently on the tetrahedral sublattice [196], *cf.* Equation 4.18. This naturally polarizes the triangular planes more than the kagomé plane. Therefore, the symmetry breaking is explicitly induced by the Hamiltonian and not spontaneously as in the quantum case.

While an isotropic spin-1/2 Heisenberg material is still lacking today, (approximate) realizations of higher spin models $\text{NaCaNi}_2\text{F}_7$ [254] ($S = 1$) and CdCr_2O_4 [358] ($S = 3/2$) are available. The latter one exhibits a stable half-magnetization plateau. Therefore, putting the obtained field values into an experimental context is interesting. The closest realization of this model is the spin-1 Heisenberg compound $\text{NaCaNi}_2\text{F}_7$ which exhibits exchange parameters of the order $J \approx 3.2 \text{ meV}$. Assuming similar values and the g -factor $g_z \approx 2$ for the spin-1/2 case yields a saturation field around $B_{\text{sat}} \approx 110 \text{ T}$ and the 1/2-plateau is expected for $B \approx 68 \text{ T}$. These field strengths are accessible in pulsed field experiments.

Ref. [349] proposed a specific ground state for the $S = 3/2$ model. Performing a careful DMRG analysis shows that the R -state has higher energy than the best variational wavefunction directly obtained from DMRG ($\sim 0.05 J$). Note that a pinning field at low bond dimensions compatible with the observed ordered 1/2-plateau state improves the convergence and yields lower energies.

This work demonstrated that the wealth of mechanisms occurring in frustrated magnets, such as quantum order-by-disorder, are present in the case of magnetic fields. Studying the magnetization process is equally demanding but hosts equally exotic phases. On the methodological side, the remarkable development of MPS techniques is capable of targeting sectors of finite magnetization, paving the way for further studies.

Dr. Imre Hagymási performed the DMRG calculation.

5.3 Hard-hexagon crystal

Abundance of hard-hexagon crystals in the quantum pyrochlore antiferromagnet

[10.48550/ARXIV.2210.07235](https://arxiv.org/abs/2210.07235) (2022)

R. Schäfer, B. Placke, O. Benton, and R. Moessner

We continue our endeavor to understand the zero-temperature limit of the pyrochlore Heisenberg antiferromagnet but take a different route than in the previous two sections. Indeed, instead of targeting clusters of finite size, we propose a family of valence-bond crystals in the form of hard hexagons as potential ground states. The ensemble emerges from resonating valence-bond rings localized on hard (non-overlapping) hexagons breaking rotation, inversion, and translation symmetries spontaneously. Strikingly, the pyrochlore lattice hosts exponentially many hard-hexagon coverings, demonstrating the abundance of competing low-energy states. A suitable dressing based on a variational wavefunction provides an exact energy estimate in the thermodynamic limit, not suffering from winding loops induced by periodic boundaries of finite clusters. The proposed energy competes, within error bars, with the best numerical estimates from [Section 5.1](#) and, therefore, the hard-hexagon crystals qualify as potential ground states. Besides the competitive energy, several arguments regarding its stability, including a detailed analysis of excitations, are presented. The broad applicability of the valence-bond state extends beyond the $S = 1/2$ pyrochlore lattice, as equivalent descriptions apply to higher spin models and other frustrated lattices. The previously overlooked family of low-energy states suggests a change in perspective on such frustrated quantum magnets, in which unfrustrated motifs – the resonating valence-bond rings – are effectively uncoupled by the frustration.

5.3.1 Model and Methods

The family of valence-bond crystals in the $S = 1/2$ pyrochlore is constructed from a non-overlapping hexagon covering [\[359, 230, 360, 361\]](#) as visualized in [Figure 5.6a](#). The essential ingredients yielding its stability and low energy are found in a broader class of models such as the two-dimensional checkerboard and ruby lattices shown in [Figure 5.6b](#) and [Figure 5.6c](#). All lattices allow a decomposition into non-overlapping unfrustrated motifs exhibiting a robust finite-size gap. A quartet of bonds from the tetrahedron shared between two adjacent motifs systematically couples two pairs of neighboring spins. In the valence-bond crystal, these pairs are strongly antiferromagnetically correlated such that the quartet of bonds is doubly frustrated.

From this moment forth, we focus on the pyrochlore $S = 1/2$ Heisenberg antiferromagnet and its hexagon decomposition. However, the arguments apply analogously to the other models. For a given hard-hexagon tiling, the nearest-neighbor Heisenberg model on the pyrochlore is divided

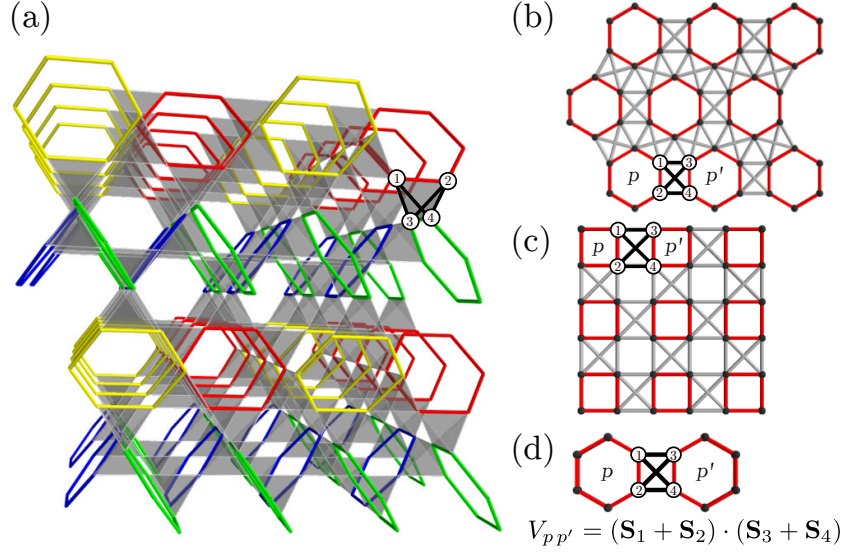


Figure 5.6: Unfrustrated motifs (hexagons and squares) in different frustrated lattices coupled via doubly frustrated bonds. (a) One hard-hexagon decomposition [230] of the three-dimensional pyrochlore lattice with $2 \times 2 \times 2$ unit cells with 48 sites each. The number of coverings is exponential in linear system size. (b) Ruby lattice with additional frustrated couplings hosting only a unique hard-hexagon tiling. The plaquette state does not break any lattice symmetry. (c) Checkerboard lattice highlighting one of two possible unfrustrated square decompositions. (d) Illustration of doubly frustrated bonds that effectively decouple the plaquettes p and p' .

into links forming hard hexagons, H_0 , and links connecting two adjacent hexagons, V :

$$H = H_0 + V = J \sum_{\langle i,j \rangle \in \square} \mathbf{S}_i \cdot \mathbf{S}_j + J \sum_{\langle i,j \rangle \notin \square} \mathbf{S}_i \cdot \mathbf{S}_j \quad (5.5)$$

5.3.2 Results

The stability and low energy of the state are based on multiple ingredients: (i) The pyrochlore lattice enables the possibility for a complete and non-overlapping tiling of unfrustrated motifs – the hard hexagons. The unfrustrated hexagons alone display a relatively low energy $E_0/N \approx -0.47 J$ already comparable to the estimates from Section 5.1. Besides its low energy, loops of even length exhibit a robust finite-size gap ($\sim 0.69 J$ in the hexagonal case) making them presumable stable towards local excitation. (ii) Couplings between two unfrustrated motifs are mediated by a quartet of bonds contributed from the tetrahedron shared between them. Linking two pairs of strongly antiferromagnetically ordered spins systematically makes them doubly frustrated as illustrated in Figure 5.6d. In that way, frustration effectively uncouples the unfrustrated motifs. (iii) One possibility to destabilize a valence-bond crystal is through the kinetic energy of local excitations. However, a detailed analysis based on a multiboson

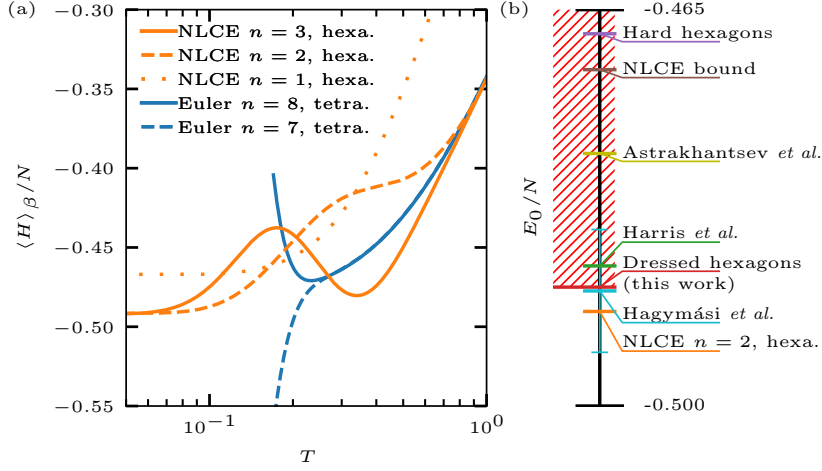


Figure 5.7: (a) Energy per site at finite temperature obtained by NLCE for the pyrochlore Heisenberg $S = 1/2$ antiferromagnet ($J = 1$). The energy of the tetrahedron-based expansion up to the eighth order from Section 4.2 is shown in blue. Orange curves are obtained from a hexagon-based expansion. (b) Comparison between different estimates of the ground-state energy per site: isolated hexagons (ground state of H_0), upper bound obtained by the converged tetrahedron expansion [1], Astrakhantsev *et al.* [234], Harris *et al.* [225], dressed hexagon state E_α/N [Equation 5.7], Hagymási *et al.* from Section 5.1 [2], and the NLCE hexagon expansion at the second order for $T = 0$. Estimates above the variational energy can be ruled out.

description suggests a suppressed kinetic energy of local defects in the valence-bond background. (iv) Hard-hexagon tilings are exponentially numerous in linear system size. However, despite their large number, different hard-hexagon decompositions in the pyrochlore are not connected by any finite order in perturbation theory.

Hard-hexagon state Taking into account the large finite-size gap, the low energy of isolated hexagons, and the suppressed coupling through the doubly frustrated bonds suggest a particular simple valence-bond crystal localized on the hexagons. This motivates the construction of a variational ansatz, minimizing the energy describing a weak dressing of isolated hexagon. Hence, the starting point for our variational wavefunction is simply the ground state of H_0 , which is composed of non-magnetic ground states on all hexagons $|s_0\rangle_p$ – a simple product state:

$$|\Psi_0\rangle = \bigotimes_p |s_0\rangle_p. \quad (5.6)$$

In order to minimize the energy further, correlations between the hexagons have to be introduced, as bonds on the hexagons already minimize their energy. A straightforward – but very successful – approach to achieve this is to evolve the initial state in imaginary time restricted on the

model	NLCE ₂	DMRG	E_{α_0}	(α_0)
pyrochlore, $S = 1/2$	-0.4917	-0.4898	-0.4895	(0.3932)
ruby, $S = 1/2$	-0.4917	-0.4883	-0.4895	(0.3935)
checkerboard, $S = 1/2$	-0.5139	-0.5136	-0.5134	(0.3053)
pyrochlore, $S = 1$	-1.4890	-1.5200	-1.4897	(0.2420)
ruby, $S = 1$	-1.4890	-1.4819	-1.4898	(0.2431)
checkerboard, $S = 1$	-1.5332	-1.5316	-1.5341	(0.1970)

Table 5.3: Comparison of ground-state energies ($J = 1$) obtained for various models. It includes estimates based on second-order NLCE, DMRG, and the variational wavefunction [Equation 5.7] evaluated for the optimal parameter α_0 . While the DMRG energies for the pyrochlore lattice are from Hagymási *et al.* [2, 95], the DMRG results for the checkerboard ($N = 144$) and ruby lattice ($N = 96$) were obtained using ITensor [105] ($\chi = 4000$, truncated error is of the order 10^{-5}) as a part of this thesis.

connecting tetrahedral bonds included in V :

$$|\Psi_\alpha\rangle = e^{-\alpha V}|\Psi_0\rangle \quad \Rightarrow \quad E_\alpha = \frac{\langle \Psi_\alpha | H | \Psi_\alpha \rangle}{\langle \Psi_\alpha | \Psi_\alpha \rangle} \quad (5.7)$$

The linked cluster theorem [152, 112, 113, 153, 154] provides a systematic approach to evaluate the variational energy in powers of α . The expansion fully converges around a pronounced minimum at $\alpha = \alpha_0$ exhibiting an energy competitive with previous estimates [225, 2, 234, 95]. The convergence is demonstrated in Section 2.3. The low energy found for the pyrochlore $S = 1/2$ Heisenberg antiferromagnet is illustrated in Figure 5.7b. As it is obtained variationally, it defines an upper bound on the ground-state energy, thereby ruling out approaches in the literature [225, 234]. The applied algorithm introduced in Section 2.3 to evaluate the variational energy is developed as a part of the thesis.

A hexagon-based NLCE calculation further confirms the robustness of the proposed valence-bond crystal at zero temperature. Previous NLCE studies of the pyrochlore exploited the tetrahedral structure [130, 131, 134, 132, 133, 135] as it yields remarkable results at finite temperatures as demonstrated in Section 4.2 and Section 4.3. The general approach to NLCE, as described in Section 2.2, makes the application to complex structures such as a unit cell consisting of eight hexagons (48 sites) possible. Typically, consecutive orders rapidly diverge from each other after a certain point signaling the failure of convergence below some critical temperature as observed for the tetrahedron-based expansion (blue) in Figure 5.7a. However, the situation is entirely different in the hexagonal case (orange). While the expansion fails to resolve intermediate temperatures, $0.06J \leq T \leq 0.8J$, it converges for $T \rightarrow 0$. Indeed, the predicted ground-state energy is remarkably close to predictions from the variational wavefunction and other methods [225, 2, 234]. Table 5.3 compares the optimal variational energy to DMRG and second-order NLCE at $T = 0$. This behavior is reminiscent of the NLCE on the Kitaev honeycomb lattice, *cf.* Figure 2.12b, as it fails to resolve temperatures between $0.03J \leq T \leq 0.1J$. A similar observation at $T = 0$ was

made in a distorted a kagomé lattice [137].

Strikingly, the low-temperature convergence is already achieved in the second order reflecting the simplicity and locality of the hexagon wavefunction. This allows for a simple evaluation in real-space for $T = 0$ using NLCE. The first order does not support any inter-hexagon correlations and is composed of the singlet ground states of individual hexagons $|\Psi_0\rangle = \bigotimes_p |s_0\rangle_p$. In the second order, *all* pairs $\{p, p'\}$ of adjacent hexagons contribute with respect to their weight which are obtained by subtracting the first order given by the ground state of two uncoupled hexagons $|s_0\rangle_p \otimes |s_0\rangle_{p'}$. In that way, a (strong) uniform energy density on the hexagons and (weak) uniform energy density on the bonds from the tetrahedron shared between any two hexagons is obtained in the second order. This state is consistent with the variational wavefunction. The correlation strength of the strong bonds on the hexagon and the weak bonds on the quartet are listed in Table 5.4. It is in excellent agreement with the variational wavefunction, DMRG, and ED on finite clusters with OBC.

Since the NLCE algorithm is sensitive to errors, approximate methods like quantum typically or finite-temperature DMRG can not be exploited. However, the Lanczos method [106, 107] becomes exact at zero temperature, making much larger hexagonal cluster (six instead of three hexagons) accessible. Hence, we compute the ground state for all clusters up to order six. The negligible influence on the ground-state energy of the larger cluster arising in the expansion is demonstrated in Figure 5.8a as their weight is of the order $10^{-4} J$. Hence, the robustness of the hexagon crystal is further expressed by its stability on finite clusters, making the convergence of NLCE possible in the first place. We further evolve all clusters in imaginary time starting from the uncoupled hexagon state and find that the optimal time step is very close to $\alpha_0 = 0.3955$ as suggested by the linked cluster theorem in the thermodynamic limit. The minimal energy obtained by the imaginary-time evolution is remarkably close to the actual ground-state energy for all finite clusters. This is demonstrated in Figure 5.8b and Figure 5.8c. Note that Figure 5.8 only contains clusters up to order five for clarity. However, we also considered the 283 clusters occurring at order six with $N = 36$. The final NLCE results for the ground-state energy per site suggested by the second- and sixth-order NLCE is $-0.4917 J$ and $-0.4919 J$, indicating the negligible influence of larger clusters. The NLCE estimate is below other predictions obtained within this thesis and literature results [225, 362, 363, 364, 365, 2, 234, 366] suggesting that the NLCE at $T = 0$ slightly underestimates the ground-state energy.

Hard-hexagon tiling and symmetry breaking The ensemble of hard-hexagon states is exponentially numerous in linear system size. A complete decomposition of the pyrochlore into hard hexagons is achieved when every site participates in exactly one hexagon. Each covering can be understood as long-ranged ordered planes consisting of two different hexagon orientations along one of three equivalent $\langle 001 \rangle$ stacking directions. The planes in Figure 5.6a are visualized by red-yellow and green-blue hexagons. Taking the covering shown in the figure as an example, a new covering is achieved by shifting one red-yellow plane along the $\langle 110 \rangle$ direction and, thereby,

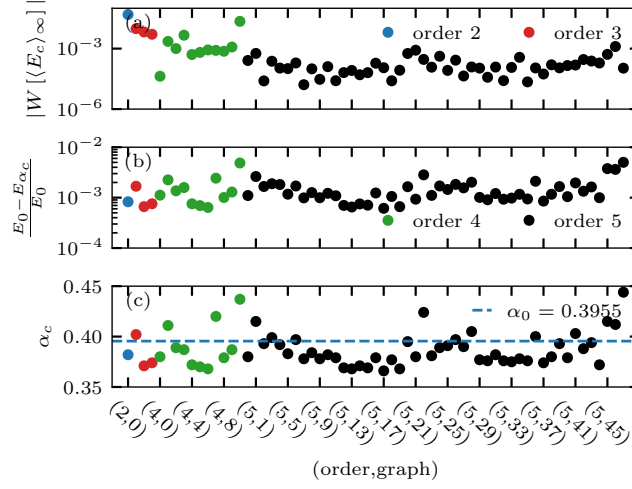


Figure 5.8: Different properties of finite clusters (order, label) arising in a hexagon-based NLCE calculation ($J = 1$). (a) The absolute value of weights for the ground-state energy. (b) Difference between the exact ground-state energy, and the variational energy obtained by optimizing $|\Psi_{\alpha_c}\rangle = e^{-\alpha_c V}|\Psi_0\rangle$ for each finite cluster c . (c) The optimal variational parameter, α_c , for each cluster.

interchange red with yellow hexagons. In this way, each plane exhibits two configurations similar to Ising spins in one dimension. Hence, the number of coverings scales with $N_{\text{cover}} \propto 2^{\sqrt[3]{N}}$. Classical MC simulations numerically verified this. Each covering corresponds to a weakly dressed wavefunction obtained by the imaginary-time evolution in V , cf. Equation 5.7.

In principle, a single hard-hexagon state can be destabilized by the exponentially large number of possible configurations. For this to happen, two family members – two different covering – have to be connected in a finite order of perturbation theory. However, this does not apply to the hexagon manifold, as generating a new covering demands shifting an entire (long-ranged ordered) plane. Another important question concerns the symmetry breaking of the ensemble along one stacking direction. In order to detect the symmetry breaking, the “dimer structure factor”, or bond correlator, is computed:

$$S_{\text{dimer}}(\mathbf{Q}) = \sum_{\langle ij \rangle, \langle kl \rangle} \exp \left(-i\mathbf{Q} \cdot \left[\frac{1}{2}(\mathbf{r}_i + \mathbf{r}_j) - \frac{1}{2}(\mathbf{r}_k + \mathbf{r}_l) \right] \right) \langle (\mathbf{S}_i \cdot \mathbf{S}_j) (\mathbf{S}_k \cdot \mathbf{S}_l) \rangle. \quad (5.8)$$

The four-point correlation function reveals pronounced Bragg peaks associated with translational and rotational symmetry breakings and broad features along the stacking direction attributed to the disorder induced by the averaging.

Excitations To provide further evidence for the stability of the hexagon crystal, we present a detailed analysis of its excitations. A simple ansatz motivated from the weakly dressed hexagon

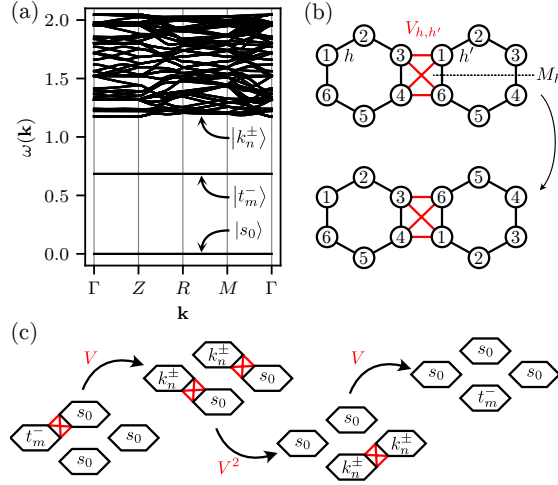


Figure 5.9: (a) Kinetic energy for all hexagon excitations in the first order of V using a multiboson theory [367, 368]. (b) Illustration of the perturbation and the mirror plane going through two hexagons. (c) Fourth-order process inducing a non-vanishing matrix element for the lowest-lying triplet. Plot and computations are from Benedikt Placke.

product state is localized excitations on a single hexagon. The lowest-lying excitation is a triplet state $|t_{m_z}^- \rangle$ with $m_z = 0, \pm 1$ exhibiting a relatively large gap of $\sim 0.69 J$. There are multiple ways to reduce the gap and make the hard-hexagon crystal potentially unstable.

One possibility is the gain of kinetic energy of these local excitations. The perturbation V allows excitations to hop across hexagons in their singlet ground state $|s_0 \rangle$, yielding a potential reduction of the gap. The kinetic energy associated with any excitation is evaluated using a multiboson theory [367, 368] in the first order of the perturbation V . Figure 5.9a shows the dispersion of all excitations on top of the non-magnetic singlet ground state. Strikingly, the lowest-lying triplet excitation $|t_{m_z}^- \rangle$ does not gain any kinetic energy and remains completely flat. The flatness is induced by the symmetry of the perturbation connecting adjacent hexagons as illustrated in Figure 5.9b. The mirror plane going through the perturbation ensures that the matrix element vanishes $\langle s_0; t_{m_z}^- | V | t_{m_z}^-; s_0 \rangle = 0$ as both states, the singlet $|s_0 \rangle$ and the triplet $|t_{m_z}^- \rangle$, are eigenstates of the symmetry operation with distinct eigenvalues $+1$ and -1 . The vanishing matrix element yields the flatness. In contrast, other excitations, *e.g.* the triplets $|k_{m_z}^\pm \rangle$, are not simultaneous eigenstates of the symmetry operation and exhibit dispersion yielding a reduction of the gap. Higher-order processes in V are necessary to achieve a finite kinetic energy of the lowest-lying triplet excitation, which potentially reduce the gap. One example is the fourth-order process illustrated in Figure 5.9c. However, we expect the effects to be suppressed due to their high order and high-energy virtual intermediate states.

As the multiboson theory predicts the irrelevance of the kinetic energy, DMRG provides insights into the local structure of the excitations [94, 105]. While a controlled analysis in the three-dimensional pyrochlore is impossible as the accessible cluster sizes are either incompat-

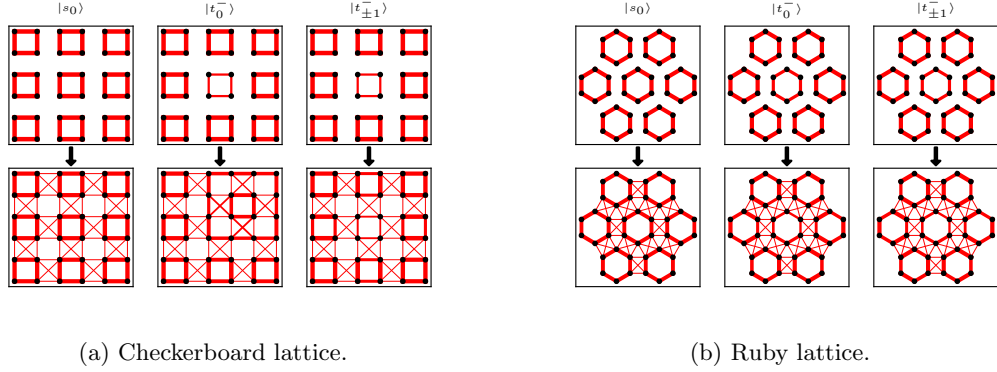


Figure 5.10: Real-space correlation obtained by DMRG for ground states (left), $m_z = 0$ excitations (center), and $m_z = \pm 1$ (right) excitations on the checkerboard ($N = 100$) and ruby ($N = 96$) lattices. The thickness indicates their strengths. The initial MPS, a simple plaquette product state, is shown in the top row. The lower row shows the optimized wavefunction obtained by ITensor [105] ($\chi = 4000$; truncation error is of the order 10^{-5}). To target the excitations, the center plaquette was initially prepared in the lowest-lying triplet excitations $|t_0^- \rangle$ (center) and $|t_{\pm 1}^- \rangle$ (right).

ible with a complete hexagon tiling or exhibit competing winding loops, we now turn to the two-dimensional checkerboard and ruby lattices. Besides a reliable estimate for the ground-state energy for both lattices, *cf.* Table 5.3, it allows targeting excitations restricted to specific magnetization sectors. To target the (presumable) local defects in the two-dimensional lattices, one plaquette is initially excited in its lowest-lying triplet state with $m_z = 0, \pm 1$ as illustrated in the top row of Figure 5.10. We find that the gaps Δ_{m_z} are stable across different system sizes and bond dimensions [6]. The gap for $m_z = 0$ is smaller than $m_z = \pm 1$, and presumably refers to a singlet excitation with $\Delta_0 \approx 0.47 J$ and $\Delta_0 \approx 0.27 J$ for the checkerboard ($N = 144$) and ruby lattice ($N = 150$), respectively. The excitations for $m_z = \pm 1$ exhibit a gap of size $\Delta_{\pm 1} \approx 0.64 J$ and $\Delta_{\pm 1} \approx 0.36 J$. Note that the gap is reduced compared to the uncoupled triplet excitation, which is $1 J$ for a square and $\sim 0.69 J$ for a hexagon. The reduction is attributed to an enhanced dressing around the defects. Figure 5.10 shows the real-space correlation pattern and reveals the local structure. Interestingly, in the case of the checkerboard lattice [bottom center of Figure 5.10a], the lowest-lying excitation for $m_z = 0$ suggests that plaquettes break up locally and reveals the formation of larger unfrustrated motifs.

5.3.3 Conclusion

This work introduces a previously overlooked family of valence-bond rings as potential ground-states of the quantum Heisenberg $S = 1/2$ pyrochlore antiferromagnet. The ensemble breaks rotation, translation, and inversion symmetry. Its stability arises from different mechanisms, including a robust finite-size gap, a suppressed kinetic energy of triplets, and the doubly frustrated bonds. The last point is conceptually the most interesting one. Indeed, instead of focusing

	Pyrochlore			Ruby			Checkerboard		
	E_{strong}	E_{weak}	E_0/N	E_{strong}	E_{weak}	E_0/N	E_{strong}	E_{weak}	E_0/N
$ \Psi_\alpha\rangle$	-0.4301	-0.0297	-0.4895	-0.4302	-0.0297	-0.4894	-0.4801	-0.0167	-0.5134
DMRG	–	–	-0.4898	-0.4357	-0.0264	-0.4885	-0.4758	-0.0190	-0.5139
NLCE 1	-0.4671	–	-0.4671	-0.4671	–	-0.4671	-0.5	–	-0.5
NLCE 2	-0.4235	-0.0341	-0.4917	-0.4235	-0.0341	-0.4917	-0.4792	-0.0173	-0.5139
ED OBC	-0.4272	-0.0337	-0.4945	-0.4337	-0.0267	-0.4871	-0.4798	-0.0176	-0.5150

Table 5.4: Comparison between strong and weak bonds of valence-bond crystals on different frustrated lattices ($S = 1/2$, $J = 1$). The ground-state energy per site is obtained by $E_0/N = E_{\text{strong}} + 2E_{\text{weak}}$. The first row corresponds to the in imaginary-time evolved wavefunction with the optimal time step [Equation 5.7]. The second row shows DMRG results where calculations on the two-dimensional lattices were performed using ITensor [105] ($\chi = 4000$, truncated error of the order 10^{-6}). The DMRG result for the pyrochlore lattice is from Section 5.1. NLCE 1 and NLCE 2 refer to the first- and second-order NLCE calculation at $T = 0$. The last row confirms the robustness of the valence-bond ring by an ED calculation of clusters ($N = 42$ and $N = 20$) with open boundary conditions. Each cluster is made up of a center plaquette of length L_p , which is coupled to L_p other plaquettes ($N = (L_p + 1)L_p$) via the doubly frustrated quartets. The values refer to the inner plaquette.

on the frustration-induced degeneracies, our approach concentrates on unfrustrated motifs – the hexagons – which are effectively uncoupled by frustration, thereby introducing a novel perspective on the field. Having understood its stability, it allows us to derive a relatively simple variational wavefunction describing a weak dressing of the ground states of uncoupled hexagons. Remarkably, the optimal variational energy is valid in the thermodynamic limit and competes, within error bars, with the previous estimate from Section 5.1, which is based on an extrapolation of finite clusters. The variational nature of our estimate makes it a strict upper bound on the ground-state energy in the thermodynamic limit, thereby ruling our predictions from the literature [225, 234]. Complementary, the robustness and simplicity of the state are further captured by various numerical methods. Strikingly, NLCE resolves the valence-bond crystal in the second order indicating its local structure. We further confirm the stability using ED (clusters containing up to 42 sites) and DMRG on two-dimensional relatives of the pyrochlore lattice. This is confirmed in Table 5.4, where the individual contributions of strong and weak bonds to the low-energy state are listed. All methods find the same ground state manifesting its robustness.

The proposed family of states is applicable beyond the three-dimensional $S = 1/2$ Heisenberg Hamiltonian on the pyrochlore. First, it applies analogously to larger spin models. While the variational energy in the $S = 1$ case is slightly higher than recent numerical DMRG estimates [95], it still provides a competitive energy taking into account the considerable finite-size effects induced by clusters containing only 48 sites. Second, the same reasoning is analogous to the two-dimensional relatives: the checkerboard and ruby lattices. The checkerboard allows only two tilings of unfrustrated squares yielding a broken inversion \mathbb{Z}_2 -symmetry. The valence-bond ring proposed here is consistent with the plaquette state in the literature [362, 363, 364, 365, 366].

In contrast, the ruby lattice hosts a unique tiling of hard hexagons respecting all the lattice symmetries. Therefore, it rather qualifies as a trivial quantum paramagnet and is, to some sense, comparable to the ground state of the Shastry-Sutherland model [177]. However, the ruby lattice is particularly interesting as it host, similar to the pyrochlore, a hard-hexagon tiling. Both lattices are equivalent up to second order in perturbation theory (and NLCE) as indicated by a similar variational wavefunction obtained for $\alpha_0 = 0.3932$ for the three-dimensional pyrochlore and for $\alpha_0 = 0.3935$ for the two-dimensional ruby lattice.

Understanding the low energy of the hexagon state allows for estimating its excitations. The suppressed kinetic energy suggests low-lying triplet excitations localized on a single hexagon. Another possibility observed in the checkerboard lattice is singlet excitations generated from larger unfrustrated motifs.

On the computational side, this work demonstrates the combination of highly optimized numerical routines described in [Chapter 2](#); without these, the result would not have been found. First, optimized ED routines are capable of diagonalizing clusters containing up to $N = 42$ sites. Second, the generic implementation of NLCE allows its application to complex geometries, such as a unit cell consisting of eight individual hexagons in three dimensions. Third, DMRG and TDVP further confirm the stability of the valence-bond crystal and the expansion in powers of α , cf. [Figure 2.14b](#). Fourth, the algorithm developed in [Section 2.3](#) describes a suitable dressing and makes the precise determination of the energy possible.

To conclude, we cannot provide a definite answer if the family of valence-bond crystals describes the ground state of the quantum pyrochlore Heisenberg $S = 1/2$ antiferromagnet. However, being exponentially numerous in the linear size of the system and exhibiting a remarkably low energy, the states will clearly affect the low temperature properties of the pyrochlore. Exquisitely low temperatures will be required to select one of these competing low-energy states, which will take place via residual deviations from an ideal Hamiltonian. The fact that the states have been previously overlooked and (maybe) the general difficulty to arrive at a consensus over the ground state in the quantum pyrochlore antiferromagnet is likely due to the presence of the vast number of near-degenerate states.

Introducing a new perspective on frustration and a new family of states associated with it comes with many exciting opportunities to study the low-energy physics of such quantum magnets. Being a ground-state candidate and allowing a precise determination of its energy makes its competition with the $U(1)$ QSL a legitimate and interesting question. The QSL regime might make way for the hard-hexagon crystal beyond the perturbative approximation around the CSI limit. Therefore, investigating its stability beyond the isotropic Heisenberg model is the next step. Our findings once more illustrate the difficulties and the lack of controlled methods in three dimensions when studying frustration. Note that none of the previous studies on finite clusters is consistent [[2](#), [234](#), [4](#), [95](#)] with a complete hexagon tiling. Hence, future investigations on finite clusters should provide the possibility to host the hard-hexagon crystal.

Benedikt Placke performed the symmetry analysis of the hexagon states and the multiboson theory.

Chapter 6

CONCLUSION AND OUTLOOK

Despite the arsenal of available numerical methods, frustration in three dimensions is not well understood. The fully frustrated quantum pyrochlore Heisenberg $S = 1/2$ antiferromagnet is barely accessible using established methods; hence, predictions in the fully frustrated regime beyond the perturbative QSI are primarily determined by uncontrolled methods. This inaccessibility of the problem is expressed by the lack of a reliable estimate for the ground-state energy and the *zoo* of candidate ground states. However, as this thesis demonstrates, cluster expansion methods are promising and powerful alternatives to obtain a glance into three-dimensional frustrated magnets. By design, they do not suffer from dimensionality or frustration as they mainly rely on exact diagonalization. Besides being unbiased and controlled, their great advantage is that they produce reliable insights into the thermodynamic limit without any restriction in the parameter space.

One crucial factor making the advances possible is the general description of the NLCE algorithms [125, 126, 127, 128]. The generic formalism based on a unit cell allows the dynamic inclusion of complex non-isotropic models using an input file at runtime. In that way, the code is adaptable to complicated problems such as unit cells comprised of eight hexagons (48 sites), anisotropies induced by the local easy-axis of the dipolar-octupolar pyrochlores, or the Kitaev model on the honeycomb lattice.

The success of NLCE presented in Chapter 4 is possible due to the extensive use of symmetries. Indeed, maximizing the benefits of automorphisms enables the inclusion of clusters with non-trivial hexagonal and octagonal loops containing up to 25 sites – unprecedented for generic clusters – for the first time. Converging down to non-trivial temperatures fully resolves the Schottky anomaly, revealing a large residual entropy up to remarkably low temperatures. It is possible to apply NLCE beyond the isotropic Heisenberg point and to study promising quantum spin-liquid candidates: the dipolar-octupolar pyrochlores. The thesis investigates systematically experimental data on Cerium-based pyrochlore and constrains their microscopic exchange parameters. Strikingly, despite a similar chemical decomposition, NLCE reveals fundamental differences between both materials by placing $\text{Ce}_2\text{Zr}_2\text{O}_7$ in a dipolar $U(1)_\pi$ QSL close to an octupolar character and $\text{Ce}_2\text{Sn}_2\text{O}_7$ in an ordered dipolar phase but in close proximity to a $U(1)_0$

QSL. The comprehensive applicability of NLCE calls for broader use in the quantitative modeling of quantum magnets.

The same lack of controlled methods applies to the zero-temperature case. Despite the challenges, [Chapter 5](#) reports significant progress in solving the notoriously difficult problem of finding the ground state of the pyrochlore Heisenberg $S = 1/2$ antiferromagnet. Using large-scale $SU(2)$ -symmetric DMRG, the first two sections demonstrate its capabilities beyond one and two dimensions by allowing a controlled calculation of finite clusters containing up to 128 sites. Besides a reliable extrapolation of the ground-state energy to the thermodynamic limit, the most striking finding is a robust and spontaneous inversion symmetry breaking stable across several finite clusters. Remarkably, our findings are supported by earlier perturbative treatments from three decades ago [225]. Extending this methodology provides insights into the magnetization process, suggesting a $1/2$ -magnetization plateau in the thermodynamic limit. The observed rotational symmetry-breaking, reminiscent of kagomé ice, is presumably induced by a quantum order-by-disorder mechanism. Finally, we proposed a family of valence-bond rings – exponentially numerous in the linear size of the system – as potential ground states of this long-standing problem. Understanding its stability (and simplicity) introduces a change of perspective on frustration with broad applicability where unfrustrated motifs are effectively uncoupled by frustration. Strikingly, all scenarios suggest a transition from a finite-temperature spin-liquid regime towards a symmetry-broken state at low temperatures contradicting the prominent spin-liquid assumption at zero temperature.

Discoveries found in this thesis pave the way for future studies starting from the novel physical insights but also aiming at further advances on the methodological front. First, pushing state-of-the-art numerics demands access to either (even) larger computing power or a more sophisticated (and environmentally friendly) alternative which is extending the use of symmetries. Hence, combining the $SU(2)$ symmetry and spatial automorphisms yields powerful improvements, particularly for higher spin models making the $S = 1$ pyrochlore Heisenberg antiferromagnet accessible up to order six. Second, the current NLCE code does not fully support spatially dependent observables such as spin correlations and the spin structure factor. Its implementation is of relevance for more sophisticated experimental comparisons. Third, a further promising approach to extending the NLCE algorithm is the controlled inclusion of approximate methods such as quantum typicality. Naively including approximate methods yields the breakdown of the NLCE as it is extremely sensitive to errors. However, as described at the end of [Section 2.2](#), having a reliable estimate of the error and observable allows for its inclusion in a controlled way. Fourth, this thesis reports fundamentally different convergence tendencies of NLCE, *e.g.* tetrahedron versus hexagon¹ expansion. Understanding the origin of this is an exciting question that may reveal further insights into these physical systems and the algorithm itself.

The discovery of the previously overlooked family of valence-bond rings opens up various possibilities for future studies. Having understood its stability and low energy, it seems natural

¹A similar observation was made on the Kitaev model on the honeycomb lattice.

to wonder about the robustness of the hexagon crystal beyond the isotropic Heisenberg point. As the hexagon crystal qualifies as a ground-state candidate, a transition from the $U(1)$ QSL into the valence-bond crystal beyond the perturbative QSI regime is a plausible scenario. In general, the new perspective, unfrustrated motifs effectively uncoupled by frustration, provides fertile ground for further studies. The weakly dressed variational wavefunction allows for various generalizations. First, one exciting possibility is the inclusion of anisotropic dressings that might further reduce the energy. Second, a dressed variational wavefunction starting from a dimer covering consistent with the broken inversion symmetry might yield a similar competing energy. Third, generalizing the procedure to larger unfrustrated motifs enables a possible description of excitations on top of the valence-bond crystal.

To conclude, the community will benefit from this thesis in two ways: the methodological advancements and the physical insights they allow. Many discoveries from [Chapter 4](#) and [Chapter 5](#) were only possible due to the advancements of controlled numerical methods presented in [Chapter 2](#). In particular, this thesis demonstrates that cluster expansion methods qualify as powerful approaches to the pyrochlore Heisenberg $S = 1/2$ antiferromagnet at *finite* and *zero* temperature.

LIST OF TABLES

2.1	Number of connected $ \mathcal{C}_n $ and topologically distinct $ \mathcal{T}_n $ clusters for the tetrahedron-based expansion.	44
2.2	Lowest variational energy E_{α_0}/N and the optimal parameter α_0 for all models considered and different spin lengths ($J = 1$).	51
2.3	Coefficients describing the energy contribution of the two different bonds derived using the linked cluster theorem in powers of α for different lattices and spin lengths ($J = 1$).	54
4.1	Optimal exchange parameters obtained from best-fit NLCE calculation from the specific heat and magnetic susceptibility.	94
5.1	Vectors \mathbf{v}_1 , \mathbf{v}_2 , and \mathbf{v}_3 framing the eight clusters considered in Section 5.1 and Section 5.2.	99
5.2	Extrapolated ground-state energy, singlet, and triplet excitations for different clusters with periodic boundary conditions.	101
5.3	Comparison of ground-state energies ($J = 1$) obtained for various models consistent with the valence-bond crystal.	112
5.4	Comparison between strong and weak bonds of valence-bond crystals on different frustrated lattices ($S = 1/2$, $J = 1$).	117

LIST OF ILLUSTRATIONS

2.1	Utilization of different symmetries to block-diagonalize the Hamiltonian.	20
2.2	(a) Maximal block sizes of the ground-state sector for different symmetries per system size. (b) Lowest energy in different symmetry sectors for a chain with PBC and $N = 42$	21
2.3	Possible paths to generate $SU(2)$ -symmetric states for $N = 4$ and $S = 1$	25
2.4	Different paths to generate $SU(2)$ -symmetric states for a system with $N = 2, 3, 4$ and $S = 1/2$ sites in panels (a), (b), and (c).	26
2.5	Eigenvalues of the isotropic Heisenberg Hamiltonian H_{XXX} on a periodic chain.	27
2.6	Illustration of the maximal commuting subgroup.	30
2.7	Reduced graph (left) for a triangular-based NLCE in the kagomé lattice (right).	36
2.8	Different steps of the NLCE algorithm for a triangular-based expansion in the kagomé lattice.	38
2.9	Cluster generated from different expansions in different lattices.	39
2.10	NLCE weight for a triangular-based expansion in the kagomé lattice.	40
2.11	Benchmarking different expansions in the pyrochlore lattice.	42
2.12	(a) Specific heat per site in the antiferromagnet Heisenberg model on the kagomé lattice and (b) the Kitaev model on the honeycomb lattice.	43
2.13	Reduced graph of the checkerboard lattice.	48
2.14	Variational energy E_α/N in the Heisenberg $S = 1/2$ model on the (a) pyrochlore and (b) checkerboard lattices.	52
3.1	Pyrochlore (Kagomé) lattice consisting of corner-sharing tetrahedra (triangles).	58
4.1	Heat capacity per site in the isotropic pyrochlore Heisenberg $S = 1/2$ antiferromagnet ($J = 1$).	74
4.2	Heat capacity of quantum pyrochlore Heisenberg $S = 1/2$ antiferromagnet ($J = 1$) calculated with NLCE, quantum typicality, and finite-temperature DMRG.	75
4.3	Heat capacity of quantum $S = 1/2$ pyrochlore Heisenberg antiferromagnet ($J = 1$) with an external field $h > 0$ and entropy for $h = 0$	76
4.4	Magnetic observables as a function of temperature computed for the quantum pyrochlore Heisenberg $S = 1/2$ antiferromagnet ($J = 1$).	77

4.5	(a) Static spin structure factor of a finite cluster ($N = 48$) at finite temperature using DMRG and (b) the total spin per tetrahedron as a function of temperature derived by different methods.	79
4.6	Interpolated specific heat data using with the entropy method [272].	80
4.7	Expected phases for the XYZ -Hamiltonian on the pyrochlore lattice.	86
4.8	Neutron experiments and fits for Cerium-based pyrochlores.	87
4.9	The lowest converged temperature in Kelvin of the sixth order NLCE data of the specific heat.	88
4.10	Goodness-of-fit of the heat capacity for Cerium-based pyrochlores.	90
4.11	Comparison between the experiments on Cerium-based pyrochlores and proposed exchange parameters of the heat capacity using the seventh order NLCE.	91
4.12	Goodness-of-fit of the magnetic susceptibility for Cerium-based pyrochlores.	93
4.13	Magnetic susceptibility measurements for Cerium-based pyrochlores.	95
5.1	(a) Finite-size scaling of the extrapolated ground-state energies for different cluster sizes and geometries ($J = 1$). (b) Real-space spin correlation of the ground state for a cluster with $N = 128$	100
5.2	(a) Converged NLCE results (tetrahedron expansion, eighth order) defining an upper bound. (b) Order parameter to detect spontaneous inversion symmetry breaking in the pyrochlore.	102
5.3	Spin structure factor in (H, H, L) and $(H, L, 0)$ plane for $N = 32, 64, 108, 128$ sites using $\chi = 20\,000, 16\,000, 16\,000, 12\,000$, respectively.	103
5.4	(a) Magnetization curve for different cluster sizes and geometries at zero temperature. (b) Extrapolation to the thermodynamic limit using a linear fit in $1/N$ for different magnetization plateaus.	105
5.5	(a) Real-space magnetization for the $N = 128$ cluster truncated to a cubic cell. (b) Spin structure factor in (H, H, L) and $(H, L, 0)$ plane.	107
5.6	Unfrustrated motifs (hexagons and squares) in different frustrated lattices.	110
5.7	(a) Energy per site at finite temperature obtained by NLCE for the pyrochlore Heisenberg $S = 1/2$ antiferromagnet ($J = 1$). (b) Comparison between different estimates of the ground-state energy per site.	111
5.8	Different properties of finite clusters (order, label) arising in a hexagon-based NLCE calculation ($J = 1$).	114
5.9	Excitation analysis using Multiboson theory.	115
5.10	Real-space correlation obtained by DMRG for ground states and excitations.	116

BIBLIOGRAPHY

- [1] R. Schäfer, I. Hagymási, R. Moessner, and D. J. Luitz, [Physical Review B](#) **102**, 054408 (2020).
- [2] I. Hagymási, R. Schäfer, R. Moessner, and D. J. Luitz, [Physical Review Letters](#) **126**, 117204 (2021).
- [3] E. M. Smith, O. Benton, D. R. Yahne, B. Placke, R. Schäfer, J. Gaudet, J. Dudemaine, A. Fitterman, J. Beare, A. R. Wildes, S. Bhattacharya, T. DeLazzer, C. R. C. Buhariwalla, N. P. Butch, R. Movshovich, J. D. Garrett, C. A. Marjerrison, J. P. Clancy, E. Kermarrec, G. M. Luke, A. D. Bianchi, K. A. Ross, and B. D. Gaulin, [Physical Review X](#) **12**, 021015 (2022).
- [4] I. Hagymási, R. Schäfer, R. Moessner, and D. J. Luitz, [Physical Review B](#) **106**, L060411 (2022).
- [5] R. Schäfer, J. C. Budich, and D. J. Luitz, [Physical Review Research](#) **4**, 033181 (2022).
- [6] R. Schäfer, B. Placke, O. Benton, and R. Moessner [10.48550/ARXIV.2210.07235](#) (2022).
- [7] D. R. Yahne, B. Placke, R. Schäfer, O. Benton, R. Moessner, M. Powell, J. W. Kolis, C. M. Pasco, A. F. May, M. D. Frontzek, E. M. Smith, B. D. Gaulin, S. Calder, and K. A. Ross [10.48550/ARXIV.2211.15140](#) (2022).
- [8] U. N. D. of Economic and P. D. Social Affairs, [World Population Prospects 2022: Summary of results](#) (2022).
- [9] P. Schultheiss, S. S. Nooten, R. Wang, M. K. L. Wong, F. Brassard, and B. Guénard, [Proceedings of the National Academy of Sciences](#) **119**, e2201550119 (2022).
- [10] E. Schrödinger, [Annalen der Physik](#) **384**, 361 (1926).
- [11] E. Schrödinger, [Physical Review](#) **28**, 1049 (1926).
- [12] P. W. Anderson, [Science](#) **177**, 393 (1972).
- [13] E. Fermi, P. Pasta, S. Ulam, and M. Tsingou, [STUDIES OF THE NONLINEAR PROBLEMS](#) (1955).

- [14] W. Pauli, *Zeitschrift für Physik* **43**, 601 (1927).
- [15] J. B. Goodenough, *Physical Review* **100**, 564 (1955).
- [16] P. W. Anderson, *Physical Review* **115**, 2 (1959).
- [17] J. Kanamori, *Journal of Physics and Chemistry of Solids* **10**, 87 (1959).
- [18] P. Fazekas, *Lecture Notes on Electron Correlation and Magnetism* (WORLD SCIENTIFIC, 1999).
- [19] F. Hund, *Zeitschrift für Physik* **33**, 345 (1925).
- [20] W. Kutzelnigg and J. D. Morgan, *Zeitschrift für Physik D Atoms, Molecules and Clusters* **36**, 197 (1996).
- [21] J. S. Gardner, M. J. P. Gingras, and J. E. Greedan, *Reviews of Modern Physics* **82**, 53 (2010).
- [22] J. G. Rau and M. J. Gingras, *Annual Review of Condensed Matter Physics* **10**, 357 (2019).
- [23] J. Villain, *Zeitschrift für Physik B Condensed Matter* **33**, 31 (1979).
- [24] J. Villain, R. Bidaux, J. P. Carton, and R. Conte, *Journal de Physique* **41**, 1263 (1980).
- [25] R. Moessner and J. T. Chalker, *Physical Review Letters* **80**, 2929 (1998).
- [26] G. H. Wannier, *Physical Review* **79**, 357 (1950).
- [27] P. W. Anderson, *Physical Review* **102**, 1008 (1956).
- [28] R. Moessner and J. T. Chalker, *Physical Review B* **58**, 12049 (1998).
- [29] L. Landau, *Nature* **138**, 840 (1936).
- [30] L. D. Landau, E. M. Lifshits, L. P. Pitaevskii, J. B. Sykes, and M. J. Kearsley, *Statistical physics* (1980).
- [31] P. M. Chaikin and T. C. Lubensky, *Principles of Condensed Matter Physics* (Cambridge University Press, Cambridge, 1995).
- [32] M. Plischke and B. Bergersen, *Equilibrium Statistical Physics* (WORLD SCIENTIFIC, 2006).
- [33] R. Moessner, in *Spin Ice*, Springer Series in Solid-State Sciences, edited by M. Udagawa and L. Jaubert (Springer International Publishing, Cham, 2021) pp. 37–70.
- [34] J. M. Kosterlitz and D. J. Thouless, *Journal of Physics C: Solid State Physics* **6**, 1181 (1973).

- [35] J. M. Kosterlitz, *Journal of Physics C: Solid State Physics* **7**, 1046 (1974).
- [36] P. Curie, *Ann Chim Phys.* **5**, 289 (1895).
- [37] L. Néel, *Annales de Physique* **10**, 5 (1932).
- [38] L. Néel, *Annales de Physique* **11**, 232 (1936).
- [39] A. Tribesinger, *Nature Physics* **8**, 263 (2012).
- [40] L. d. Broglie, *Recherches sur la théorie des quanta.*, Ph.D. thesis, Masson, Paris (1924).
- [41] L. d. Broglie, *The London, Edinburgh, and Dublin Philosophical Magazine and Journal of Science* **47**, 446 (1924).
- [42] W. Heisenberg, *Zeitschrift für Physik* **33**, 879 (1925).
- [43] W. Heisenberg, *Zeitschrift für Physik* **38**, 411 (1926).
- [44] M. Born, W. Heisenberg, and P. Jordan, *Zeitschrift für Physik* **35**, 557 (1926).
- [45] W. Heisenberg, *Zeitschrift für Physik* **49**, 619 (1928).
- [46] P. A. M. Dirac and R. H. Fowler, *Proceedings of the Royal Society of London. Series A, Containing Papers of a Mathematical and Physical Character* **117**, 610 (1928).
- [47] P. A. M. Dirac and R. H. Fowler, *Proceedings of the Royal Society of London. Series A, Containing Papers of a Mathematical and Physical Character* **126**, 360 (1930).
- [48] W. Pauli, *Zeitschrift für Physik A Hadrons and nuclei* **36**, 336 (1926).
- [49] M. Born, *Zeitschrift für Physik* **37**, 863 (1926).
- [50] M. Born and N. Wiener, *Zeitschrift für Physik* **36**, 174 (1926).
- [51] C. Eckart, *Physical Review* **28**, 711 (1926).
- [52] P. Jordan and E. Wigner, *Zeitschrift für Physik* **47**, 631 (1928).
- [53] J. C. Slater, *Physical Review* **34**, 1293 (1929).
- [54] W. Gerlach and O. Stern, *Zeitschrift für Physik* **9**, 349 (1922).
- [55] A. H. Compton, *Physical Review* **21**, 483 (1923).
- [56] C. D. Anderson, *Physical Review* **43**, 491 (1933).
- [57] W. E. Lamb and R. C. Retherford, *Physical Review* **72**, 241 (1947).
- [58] D. J. Griffiths and D. F. Schroeter, *Introduction to Quantum Mechanics* (Cambridge University Press, Cambridge, 2018).

- [59] Guth, *Monatshefte für Mathematik und Physik* **40**, A31 (1933).
- [60] J. von Neumann, *Mathematische Grundlagen der Quantenmechanik* (Springer, Berlin, Heidelberg, Berlin Heidelberg, 1996).
- [61] B. Falkenburg and P. Mittelstaedt, in *Compendium of Quantum Physics*, edited by D. Greenberger, K. Hentschel, and F. Weinert (Springer, Berlin, Heidelberg, 2009) pp. 485–491.
- [62] F. Bloch, *Physical Review* **70**, 460 (1946).
- [63] M. A. Nielsen and I. L. Chuang, *Quantum Computation and Quantum Information: 10th Anniversary Edition* (Cambridge University Press, 2010).
- [64] H. Bethe, *Zeitschrift für Physik* **71**, 205 (1931).
- [65] M. Born and P. Jordan, *Zeitschrift für Physik* **34**, 858 (1925).
- [66] R. P. Feynman, *Reviews of Modern Physics* **20**, 367 (1948).
- [67] R. P. R. P. Feynman, *Quantum mechanics and path integrals* (New York : McGraw-Hill, 1965).
- [68] I. Affleck, T. Kennedy, E. H. Lieb, and H. Tasaki, *Physical Review Letters* **59**, 799 (1987).
- [69] A. Kitaev, *Annals of Physics January Special Issue*, **321**, 2 (2006).
- [70] A. Y. Kitaev, *Annals of Physics* **303**, 2 (2003).
- [71] A. W. Sandvik and J. Kurkijärvi, *Physical Review B* **43**, 5950 (1991).
- [72] A. W. Sandvik, *Physical Review B* **59**, R14157 (1999).
- [73] O. F. Syljuåsen and A. W. Sandvik, *Physical Review E* **66**, 046701 (2002).
- [74] R. G. Melko, *Journal of Physics: Condensed Matter* **19**, 145203 (2007).
- [75] E. Y. Loh, J. E. Gubernatis, R. T. Scalettar, S. R. White, D. J. Scalapino, and R. L. Sugar, *Physical Review B* **41**, 9301 (1990).
- [76] Y. Kato and S. Onoda, *Physical Review Letters* **115**, 077202 (2015).
- [77] C.-J. Huang, C. Liu, Z. Meng, Y. Yu, Y. Deng, and G. Chen, *Physical Review Research* **2**, 042022 (2020).
- [78] F. Assaad and H. Evertz, in *Computational Many-Particle Physics*, Lecture Notes in Physics, edited by H. Fehske, R. Schneider, and A. Weiße (Springer, Berlin, Heidelberg, 2008) pp. 277–356.

- [79] A. W. Sandvik, [AIP Conference Proceedings](#) **1297**, 135 (2010).
- [80] E. Pavarini, E. Koch, and U. Schollwöck, *Emergent Phenomena in Correlated Matter*, FZJ-2013-04137 (2013).
- [81] J. Gubernatis, N. Kawashima, and P. Werner, *Quantum Monte Carlo Methods: Algorithms for Lattice Models* (Cambridge University Press, Cambridge, 2016).
- [82] N. Shannon, in *Spin Ice*, Springer Series in Solid-State Sciences, edited by M. Udagawa and L. Jaubert (Springer International Publishing, Cham, 2021) pp. 273–301.
- [83] S. R. White, [Physical Review Letters](#) **69**, 2863 (1992).
- [84] S. R. White, [Physical Review B](#) **48**, 10345 (1993).
- [85] U. Schollwöck, [Reviews of Modern Physics](#) **77**, 259 (2005).
- [86] K. A. Hallberg, [Advances in Physics](#) **55**, 477 (2006).
- [87] U. Schollwöck, [Annals of Physics January 2011 Special Issue](#), **326**, 96 (2011).
- [88] S. Östlund and S. Rommer, [Physical Review Letters](#) **75**, 3537 (1995).
- [89] J. Dukelsky, M. A. Martín-Delgado, T. Nishino, and G. Sierra, [Europhysics Letters](#) **43**, 457 (1998).
- [90] G. Vidal, J. I. Latorre, E. Rico, and A. Kitaev, [Physical Review Letters](#) **90**, 227902 (2003).
- [91] J. Latorre, E. Rico, and G. Vidal, [Quantum Information and Computation](#) **4**, 48 (2004).
- [92] F. Verstraete, V. Murg, and J. Cirac, [Advances in Physics](#) **57**, 143 (2008).
- [93] J. Eisert, M. Cramer, and M. Plenio, [Reviews of Modern Physics](#) **82**, 277 (2010).
- [94] E. Stoudenmire and S. R. White, [Annual Review of Condensed Matter Physics](#) **3**, 111 (2012).
- [95] I. Hagymási, V. Nocolak, and J. Reuther, [Phys. Rev. B](#) **106**, 235137 (2022).
- [96] S. R. White and A. E. Feiguin, [Physical Review Letters](#) **93**, 076401 (2004).
- [97] A. J. Daley, C. Kollath, U. Schollwöck, and G. Vidal, [Journal of Statistical Mechanics: Theory and Experiment](#) **2004**, P04005 (2004).
- [98] G. Vidal, [Physical Review Letters](#) **93**, 040502 (2004).
- [99] F. Verstraete, J. J. García-Ripoll, and J. I. Cirac, [Physical Review Letters](#) **93**, 207204 (2004).
- [100] A. E. Feiguin and S. R. White, [Physical Review B](#) **72**, 220401 (2005).

- [101] G. Vidal, [Physical Review Letters](#) **98**, 070201 (2007).
- [102] I. P. McCulloch [10.48550/ARXIV.0804.2509](#) (2008).
- [103] R. Orús and G. Vidal, [Physical Review B](#) **78**, 155117 (2008).
- [104] R. Orús, [Annals of Physics](#) **349**, 117 (2014).
- [105] M. Fishman, S. R. White, and E. M. Stoudenmire, [SciPost Phys. Codebases](#) , 4 (2022).
- [106] A. Wietek and A. M. Läuchli, [Physical Review E](#) **98**, 033309 (2018).
- [107] A. M. Läuchli, J. Sudan, and R. Moessner, [Physical Review B](#) **100**, 155142 (2019).
- [108] S. D. Pace, S. C. Morampudi, R. Moessner, and C. R. Laumann, [Physical Review Letters](#) **127**, 117205 (2021).
- [109] C. Lanczos, Journal of research of the National Bureau of Standards **45**, 255 (1950).
- [110] J. Jaklič and P. Prelovšek, [Physical Review B](#) **49**, 5065 (1994).
- [111] J. Schnack, J. Schulenburg, and J. Richter, [Physical Review B](#) **98**, 094423 (2018).
- [112] K. A. Brueckner, [Physical Review](#) **97**, 1353 (1955).
- [113] J. Goldstone, [Proceedings of the Royal Society of London. Series A. Mathematical and Physical Sciences](#) **239**, 267 (1957).
- [114] E. Noether, [Nachrichten von der Gesellschaft der Wissenschaften zu Göttingen, Mathematisch-Physikalische Klasse](#) **1918**, 235 (1918).
- [115] V. Hernandez, J. E. Roman, and V. Vidal, [Lect. Notes Comput. Sci.](#) **2565**, 377 (2003).
- [116] V. Hernandez, J. E. Roman, and V. Vidal, [ACM Trans. Math. Software](#) **31**, 351 (2005).
- [117] V. Hernández, J. E. Román, and A. Tomás, [Parallel Comput.](#) **33**, 521 (2007).
- [118] J. E. Roman, C. Campos, L. Dalcin, E. Romero, and A. Tomas, *SLEPc Users Manual*, Tech. Rep. DSIC-II/24/02 - Revision 3.17 (D. Sistemes Informàtics i Computació, Universitat Politècnica de València, 2022).
- [119] H. Lin, J. Gubernatis, H. Gould, and J. Tobochnik, [Computers in Physics](#) **7**, 400 (1993).
- [120] P. Nataf and F. Mila, [Phys. Rev. Lett.](#) **113**, 127204 (2014).
- [121] N. Borghini, [Symmetries in Physics](#) (2018).
- [122] A. Alex, M. Kalus, A. Huckleberry, and J. von Delft, [Journal of Mathematical Physics](#) **52**, 023507 (2011).

- [123] B. D. McKay and A. Piperno, [Journal of Symbolic Computation](#) **60**, 94 (2014).
- [124] J. Konc and D. Janežić, [MATCH - Communications in Mathematical and in Computer Chemistry](#) **58**, 569 (2007).
- [125] M. Rigol, T. Bryant, and R. R. P. Singh, [Physical Review Letters](#) **97**, 187202 (2006).
- [126] M. Rigol, T. Bryant, and R. R. P. Singh, [Phys. Rev. E](#) **75**, 061118 (2007).
- [127] M. Rigol, T. Bryant, and R. R. P. Singh, [Phys. Rev. E](#) **75**, 061119 (2007).
- [128] B. Tang, E. Khatami, and M. Rigol, [Computer Physics Communications](#) **184**, 557 (2013).
- [129] E. Khatami, J. S. Helton, and M. Rigol, [Physical Review B](#) **85**, 064401 (2012).
- [130] R. Applegate, N. R. Hayre, R. R. P. Singh, T. Lin, A. G. R. Day, and M. J. P. Gingras, [Physical Review Letters](#) **109**, 097205 (2012).
- [131] R. R. P. Singh and J. Oitmaa, [Physical Review B](#) **85**, 144414 (2012).
- [132] L. D. C. Jaubert, O. Benton, J. G. Rau, J. Oitmaa, R. R. P. Singh, N. Shannon, and M. J. P. Gingras, [Physical Review Letters](#) **115**, 267208 (2015).
- [133] O. Benton, [Physical Review Letters](#) **121**, 037203 (2018).
- [134] N. R. Hayre, K. A. Ross, R. Applegate, T. Lin, R. R. P. Singh, B. D. Gaulin, and M. J. P. Gingras, [Physical Review B](#) **87**, 184423 (2013).
- [135] O. Benton, L. D. C. Jaubert, R. R. P. Singh, J. Oitmaa, and N. Shannon, [Physical Review Letters](#) **121**, 067201 (2018).
- [136] T. Pardini, A. Menon, S. P. Hau-Riege, and R. R. P. Singh, [Physical Review B](#) **100**, 144437 (2019).
- [137] E. Khatami and M. Rigol, [Physical Review A](#) **84**, 053611 (2011).
- [138] E. Khatami and M. Rigol, [Physical Review B](#) **83**, 134431 (2011).
- [139] E. Khatami, R. R. P. Singh, and M. Rigol, [Physical Review B](#) **84**, 224411 (2011).
- [140] E. Khatami and M. Rigol, [Physical Review A](#) **86**, 023633 (2012).
- [141] M. Rigol, [Physical Review Letters](#) **112**, 170601 (2014).
- [142] M. Rigol, [Physical Review Letters](#) **116**, 100601 (2016).
- [143] K. Mallayya and M. Rigol, [Physical Review E](#) **95**, 033302 (2017).
- [144] J. Richter and R. Steinigeweg, [Physical Review B](#) **99**, 094419 (2019).

- [145] J. Qiao, W. Chang, X. Li, and J. Jin, [Journal of Physics Communications](#) **4**, 015020 (2020).
- [146] R. W. Hamming, *Numerical methods for scientists and engineers*, 2nd ed. (Dover Publications, 1987) p. 721.
- [147] W. H. Press, S. A. Teukolsky, W. T. Vetterling, and B. P. Flannery, *Numerical Recipes in C*, 2nd ed. (Cambridge University Press, Cambridge, USA, 1992).
- [148] E. J. Weniger [10.48550/ARXIV.MATH/0306302](#) (2003).
- [149] T. C. Eschmann, *Thermodynamics of Kitaev Spin Liquids*, [Ph.D. thesis](#), Universität zu Köln (2020).
- [150] C. Moler and C. Van Loan, [SIAM Review](#) **45**, 3 (2003).
- [151] J. Schnack, J. Richter, T. Heitmann, J. Richter, and R. Steinigeweg, [Zeitschrift für Naturforschung A](#) **75**, 465 (2020).
- [152] H. D. Ursell, [Mathematical Proceedings of the Cambridge Philosophical Society](#) **23**, 685 (1927).
- [153] J. K. Percus, [Communications in Mathematical Physics](#) **40**, 283 (1975).
- [154] S. B. Shlosman, [Communications in Mathematical Physics](#) **102**, 679 (1986).
- [155] M. Yang and S. R. White, [Phys. Rev. B](#) **102**, 094315 (2020).
- [156] P. Chandra, P. Coleman, and A. I. Larkin, [Physical Review Letters](#) **64**, 88 (1990).
- [157] A. Chubukov, [Physical Review Letters](#) **69**, 832 (1992).
- [158] C. Lacroix, P. Mendels, and F. Mila, eds., *Introduction to Frustrated Magnetism*, Springer Series in Solid-State Sciences, Vol. 164 (Springer, Berlin, Heidelberg, 2011).
- [159] J. G. Rau, E. K.-H. Lee, and H.-Y. Kee, [Annual Review of Condensed Matter Physics](#) **7**, 195 (2016).
- [160] S. V. Isakov, K. Gregor, R. Moessner, and S. L. Sondhi, [Physical Review Letters](#) **93**, 167204 (2004).
- [161] C. L. Henley, [Physical Review B](#) **71**, 014424 (2005).
- [162] C. L. Henley, [Annual Review of Condensed Matter Physics](#) **1**, 179 (2010).
- [163] M. J. Harris, S. T. Bramwell, D. F. McMorrow, T. Zeiske, and K. W. Godfrey, [Physical Review Letters](#) **79**, 2554 (1997).
- [164] S. T. Bramwell and M. J. Harris, [Journal of Physics: Condensed Matter](#) **10**, L215 (1998).

- [165] C. Castelnovo, R. Moessner, and S. L. Sondhi, *Nature* **451**, 42 (2008).
- [166] C. Castelnovo, R. Moessner, and S. Sondhi, *Annual Review of Condensed Matter Physics* **3**, 35 (2012).
- [167] L. Pauling, *Journal of the American Chemical Society* **57**, 2680 (1935).
- [168] M. Hermele, M. P. A. Fisher, and L. Balents, *Physical Review B* **69**, 064404 (2004).
- [169] L. Savary and L. Balents, *Physical Review Letters* **108**, 037202 (2012).
- [170] M. J. P. Gingras, P. A. McClarty, and J. G. Rau, in *Spin Ice*, Springer Series in Solid-State Sciences, edited by M. Udagawa and L. Jaubert (Springer International Publishing, Cham, 2021) pp. 1–18.
- [171] P. W. Anderson, *Materials Research Bulletin* **8**, 153 (1973).
- [172] R. Moessner and S. L. Sondhi, *Physical Review Letters* **86**, 1881 (2001).
- [173] X.-G. Wen, *Quantum Field Theory of Many-Body Systems: From the Origin of Sound to an Origin of Light and Electrons*, Oxford Graduate Texts (Oxford University Press, Oxford, 2007).
- [174] P. A. Lee, *Science (New York, N.Y.)* **321**, 1306 (2008).
- [175] X.-G. Wen, *Physical Review B* **65**, 165113 (2002).
- [176] E. J. Mele, *Topological insulators: mind the gap!* (2019).
- [177] B. Sriram Shastry and B. Sutherland, *Physica B+C* **108**, 1069 (1981).
- [178] J. Knolle and R. Moessner, *Annual Review of Condensed Matter Physics* **10**, 451 (2019).
- [179] Y. Ran, M. Hermele, P. A. Lee, and X.-G. Wen, *Physical Review Letters* **98**, 117205 (2007).
- [180] O. Ma and J. B. Marston, *Physical Review Letters* **101**, 027204 (2008).
- [181] M. Hermele, Y. Ran, P. A. Lee, and X.-G. Wen, *Physical Review B* **77**, 224413 (2008).
- [182] J.-W. Mei, J.-Y. Chen, H. He, and X.-G. Wen, *Physical Review B* **95**, 235107 (2017).
- [183] J. H. Kim and J. H. Han, *Physical Review B* **78**, 180410 (2008).
- [184] A. Wietek, A. Sterdyniak, and A. M. Läuchli, *Physical Review B* **92**, 125122 (2015).
- [185] M. Taillefumier, O. Benton, H. Yan, L. D. C. Jaubert, and N. Shannon, *Physical Review X* **7**, 041057 (2017).
- [186] P. W. Anderson, *Science (New York, N.Y.)* **235**, 1196 (1987).

- [187] M. B. Hastings, [Physical Review B](#) **63**, 014413 (2000).
- [188] Z. Zhou, J. Wildeboer, and A. Seidel, [Physical Review B](#) **89**, 035123 (2014).
- [189] D. S. Rokhsar and S. A. Kivelson, [Physical Review Letters](#) **61**, 2376 (1988).
- [190] J. B. Kogut, [Reviews of Modern Physics](#) **51**, 659 (1979).
- [191] P. A. Lee, N. Nagaosa, and X.-G. Wen, [Reviews of Modern Physics](#) **78**, 17 (2006).
- [192] A. Kitaev and J. Preskill, [Physical Review Letters](#) **96**, 110404 (2006).
- [193] C. Lhuillier and G. Misguich, in *Introduction to Frustrated Magnetism: Materials, Experiments, Theory*, Springer Series in Solid-State Sciences, edited by C. Lacroix, P. Mendels, and F. Mila (Springer, Berlin, Heidelberg, 2011) pp. 23–41.
- [194] L. Savary and L. Balents, [Reports on Progress in Physics](#) **80**, 016502 (2016).
- [195] D. Natelson, [Physics Today](#) [10.1063/PT.6.3.20181219a](#) (2018).
- [196] R. Moessner, [Physical Review B](#) **57**, R5587 (1998).
- [197] L. Savary and L. Balents, in *Spin Ice*, Springer Series in Solid-State Sciences, edited by M. Udagawa and L. Jaubert (Springer International Publishing, Cham, 2021) pp. 239–271.
- [198] W. F. Giauque and J. W. Stout, [Journal of the American Chemical Society](#) **58**, 1144 (1936).
- [199] J. D. Bernal and R. H. Fowler, [The Journal of Chemical Physics](#) **1**, 515 (1933).
- [200] S. T. Bramwell and M. J. P. Gingras, [Science](#) **294**, 1495 (2001).
- [201] V. F. Petrenko and R. W. Whitworth, *Physics of Ice* (Oxford University Press, Oxford, 2002).
- [202] J. F. Nagle, [Journal of Mathematical Physics](#) **7**, 1484 (1966).
- [203] S. V. Isakov, K. S. Raman, R. Moessner, and S. L. Sondhi, [Physical Review B](#) **70**, 104418 (2004).
- [204] D. J. P. Morris, D. A. Tennant, S. A. Grigera, B. Klemke, C. Castelnovo, R. Moessner, C. Czternasty, M. Meissner, K. C. Rule, J.-U. Hoffmann, K. Kiefer, S. Gerischer, D. Slobinsky, and R. S. Perry, [Science](#) **326**, 411 (2009).
- [205] H. Kadowaki, N. Doi, Y. Aoki, Y. Tabata, T. J. Sato, J. W. Lynn, K. Matsuhira, and Z. Hiroi, [Journal of the Physical Society of Japan](#) **78**, 103706 (2009).
- [206] M. E. Brooks-Bartlett, S. T. Banks, L. D. C. Jaubert, A. Harman-Clarke, and P. C. W. Holdsworth, [Physical Review X](#) **4**, 011007 (2014).

- [207] T. Fennell, P. P. Deen, A. R. Wildes, K. Schmalzl, D. Prabhakaran, A. T. Boothroyd, R. J. Aldus, D. F. McMorrow, and S. T. Bramwell, [Science](#) **326**, 415 (2009).
- [208] I. A. Ryzhkin, [Journal of Experimental and Theoretical Physics](#) **101**, 481 (2005).
- [209] R. Siddharthan, B. S. Shastry, A. P. Ramirez, A. Hayashi, R. J. Cava, and S. Rosenkranz, [Physical Review Letters](#) **83**, 1854 (1999).
- [210] B. C. den Hertog and M. J. P. Gingras, [Physical Review Letters](#) **84**, 3430 (2000).
- [211] S. V. Isakov, R. Moessner, and S. L. Sondhi, [Physical Review Letters](#) **95**, 217201 (2005).
- [212] J. P. C. Ruff, R. G. Melko, and M. J. P. Gingras, [Physical Review Letters](#) **95**, 097202 (2005).
- [213] I. Lindgren, [Journal of Physics B: Atomic and Molecular Physics](#) **7**, 2441 (1974).
- [214] D. A. Huse, W. Krauth, R. Moessner, and S. L. Sondhi, [Physical Review Letters](#) **91**, 167004 (2003).
- [215] A. Banerjee, S. V. Isakov, K. Damle, and Y. B. Kim, [Physical Review Letters](#) **100**, 047208 (2008).
- [216] N. Shannon, O. Sikora, F. Pollmann, K. Penc, and P. Fulde, [Physical Review Letters](#) **108**, 067204 (2012).
- [217] M. J. P. Gingras and P. A. McClarty, [Reports on Progress in Physics](#) **77**, 056501 (2014).
- [218] O. Benton, in [Spin Ice](#), Springer Series in Solid-State Sciences, edited by M. Udagawa and L. Jaubert (Springer International Publishing, Cham, 2021) pp. 303–323.
- [219] A. S. Patri, M. Hosoi, and Y. B. Kim, [Physical Review Research](#) **2**, 023253 (2020).
- [220] O. Benton, [Physical Review B](#) **102**, 104408 (2020).
- [221] B. Canals and C. Lacroix, [Physical Review Letters](#) **80**, 2933 (1998).
- [222] B. Canals and C. Lacroix, [Physical Review B](#) **61**, 1149 (2000).
- [223] L. Balents, [Nature](#) **464**, 199 (2010).
- [224] Y. Huang, K. Chen, Y. Deng, N. Prokof'ev, and B. Svistunov, [Physical Review Letters](#) **116**, 177203 (2016).
- [225] A. B. Harris, A. J. Berlinsky, and C. Bruder, [Journal of Applied Physics](#) **69**, 5200 (1991).
- [226] M. Isoda and S. Mori, [Journal of the Physical Society of Japan](#) **67**, 4022 (1998).
- [227] H. Tsunetsugu, [Physical Review B](#) **65**, 024415 (2001).

- [228] H. Tsunetsugu, [Journal of the Physical Society of Japan](#) **70**, 640 (2001).
- [229] A. Koga and N. Kawakami, [Physical Review B](#) **63**, 144432 (2001).
- [230] S.-H. Lee, C. Broholm, W. Ratcliff, G. Gasparovic, Q. Huang, T. H. Kim, and S.-W. Cheong, [Nature](#) **418**, 856 (2002).
- [231] E. Berg, E. Altman, and A. Auerbach, [Physical Review Letters](#) **90**, 147204 (2003).
- [232] R. Moessner, S. L. Sondhi, and M. O. Goerbig, [Physical Review B](#) **73**, 094430 (2006).
- [233] D. Tsuneishi, M. Ioki, and H. Kawamura, [Journal of Physics: Condensed Matter](#) **19**, 145273 (2007).
- [234] N. Astrakhantsev, T. Westerhout, A. Tiwari, K. Choo, A. Chen, M. H. Fischer, G. Carleo, and T. Neupert, [Physical Review X](#) **11**, 041021 (2021).
- [235] A. P. Ramirez, A. Hayashi, R. J. Cava, R. Siddharthan, and B. S. Shastry, [Nature](#) **399**, 333 (1999).
- [236] J. P. Clancy, J. P. C. Ruff, S. R. Dunsiger, Y. Zhao, H. A. Dabkowska, J. S. Gardner, Y. Qiu, J. R. D. Copley, T. Jenkins, and B. D. Gaulin, [Physical Review B](#) **79**, 014408 (2009).
- [237] J. G. Rau and M. J. P. Gingras, [Physical Review B](#) **92**, 144417 (2015).
- [238] H. W. J. Blöte, R. F. Wierlinga, and W. J. Huiskamp, [Physica](#) **43**, 549 (1969).
- [239] A. M. Hallas, J. Gaudet, and B. D. Gaulin, [Annual Review of Condensed Matter Physics](#) **9**, 105 (2018).
- [240] S. H. Curnoe, [Physical Review B](#) **78**, 094418 (2008).
- [241] S. Onoda and Y. Tanaka, [Physical Review B](#) **83**, 094411 (2011).
- [242] K. A. Ross, L. Savary, B. D. Gaulin, and L. Balents, [Physical Review X](#) **1**, 021002 (2011).
- [243] Y.-P. Huang, G. Chen, and M. Hermele, [Physical Review Letters](#) **112**, 167203 (2014).
- [244] Y.-D. Li and G. Chen, [Physical Review B](#) **95**, 041106 (2017).
- [245] J. Gaudet, E. M. Smith, J. Dudemaine, J. Beare, C. R. C. Buhariwalla, N. P. Butch, M. B. Stone, A. I. Kolesnikov, G. Xu, D. R. Yahne, K. A. Ross, C. A. Marjerrison, J. D. Garrett, G. M. Luke, A. D. Bianchi, and B. D. Gaulin, [Physical Review Letters](#) **122**, 187201 (2019).
- [246] B. Gao, T. Chen, D. W. Tam, C.-L. Huang, K. Sasmal, D. T. Adroja, F. Ye, H. Cao, G. Sala, M. B. Stone, C. Baines, J. A. T. Verezhak, H. Hu, J.-H. Chung, X. Xu, S.-W. Cheong, M. Nallaiyan, S. Spagna, M. B. Maple, A. H. Nevidomskyy, E. Morosan, G. Chen, and P. Dai, [Nature Physics](#) **15**, 1052 (2019).

- [247] R. Sibille, N. Gauthier, E. Lhotel, V. Porée, V. Pomjakushin, R. A. Ewings, T. G. Perring, J. Ollivier, A. Wildes, C. Ritter, T. C. Hansen, D. A. Keen, G. J. Nilsen, L. Keller, S. Petit, and T. Fennell, [Nature Physics](#) **16**, 546 (2020).
- [248] W. H. Bragg, [Nature](#) **95**, 561 (1915).
- [249] S.-H. Lee, H. Takagi, D. Louca, M. Matsuda, S. Ji, H. Ueda, Y. Ueda, T. Katsufuji, J.-H. Chung, S. Park, S.-W. Cheong, and C. Broholm, [Journal of the Physical Society of Japan](#) **79**, 011004 (2010).
- [250] S.-H. Lee, C. Broholm, T. H. Kim, W. Ratcliff, and S.-W. Cheong, [Physical Review Letters](#) **84**, 3718 (2000).
- [251] A. B. Sushkov, O. Tchernyshyov, W. R. II, S. W. Cheong, and H. D. Drew, [Physical Review Letters](#) **94**, 137202 (2005).
- [252] L. Clark, G. J. Nilsen, E. Kermarrec, G. Ehlers, K. S. Knight, A. Harrison, J. P. Attfield, and B. D. Gaulin, [Physical Review Letters](#) **113**, 117201 (2014).
- [253] Y. Iqbal, T. Müller, K. Riedl, J. Reuther, S. Rachel, R. Valentí, M. J. P. Gingras, R. Thomale, and H. O. Jeschke, [Physical Review Materials](#) **1**, 071201 (2017).
- [254] K. W. Plumb, H. J. Changlani, A. Scheie, S. Zhang, J. W. Krizan, J. A. Rodriguez-Rivera, Y. Qiu, B. Winn, R. J. Cava, and C. L. Broholm, [Nature Physics](#) **15**, 54 (2019).
- [255] M. Gen, Y. Okamoto, M. Mori, K. Takenaka, and Y. Kohama, [Physical Review B](#) **101**, 054434 (2020).
- [256] R. Gross and A. Marx, *Festkörperphysik* (De Gruyter Oldenbourg, 2014).
- [257] E. Ising, [Zeitschrift für Physik](#) **31**, 253 (1925).
- [258] L. Onsager, [Physical Review](#) **65**, 117 (1944).
- [259] S. T. Bramwell, in *Introduction to Frustrated Magnetism: Materials, Experiments, Theory*, Springer Series in Solid-State Sciences, edited by C. Lacroix, P. Mendels, and F. Mila (Springer, Berlin, Heidelberg, 2011) pp. 45–78.
- [260] E. M. Smith, Q. Barthélemy, S. Bhattacharya, B. D. Gaulin, E. Kermarrec, S. R. Kumar, and W. Andrew, [Polarization Analysis of the Dynamic Quantum Spin Ice Correlations in the GroundState of a Pyrochlore Magnet](#) (2021).
- [261] P. Müller, A. Lohmann, J. Richter, and O. Derzhko, [Physical Review B](#) **100**, 024424 (2019).
- [262] S. Goldstein, J. L. Lebowitz, R. Tumulka, and N. Zanghì, [Physical Review Letters](#) **96**, 050403 (2006).

- [263] S. Popescu, A. J. Short, and A. Winter, [Nature Physics](#) **2**, 754 (2006).
- [264] S. Sugiura and A. Shimizu, [Physical Review Letters](#) **108**, 240401 (2012).
- [265] S. Sugiura and A. Shimizu, [Physical Review Letters](#) **111**, 010401 (2013).
- [266] B. Bruognolo, Z. Zhu, S. R. White, and E. M. Stoudenmire [10.48550/ARXIV.1705.05578](#) (2017).
- [267] J. Haegeman, J. I. Cirac, T. J. Osborne, I. Pižorn, H. Verschelde, and F. Verstraete, [Physical Review Letters](#) **107**, 070601 (2011).
- [268] J. Haegeman, C. Lubich, I. Oseledets, B. Vandereycken, and F. Verstraete, [Physical Review B](#) **94**, 165116 (2016).
- [269] S. Paeckel, T. Köhler, A. Swoboda, S. R. Manmana, U. Schollwöck, and C. Hubig, [Annals of Physics](#) **411**, 167998 (2019).
- [270] J. J. García-Ripoll, [New Journal of Physics](#) **8**, 305 (2006).
- [271] H. J. Changlani [10.48550/ARXIV.1710.02234](#) (2017).
- [272] O. Derzhko, T. Hutak, T. Krokhmalskii, J. Schnack, and J. Richter, [Physical Review B](#) **101**, 174426 (2020).
- [273] A. Bhardwaj, S. Zhang, H. Yan, R. Moessner, A. H. Nevidomskyy, and H. J. Changlani, [npj Quantum Materials](#) **7**, 1 (2022).
- [274] D. J. Klein, [Journal of Physics A: Mathematical and General](#) **15**, 661 (1982).
- [275] J. T. Chayes, L. Chayes, and S. A. Kivelson, [Communications in Mathematical Physics](#) **123**, 53 (1989).
- [276] K. S. Raman, R. Moessner, and S. L. Sondhi, [Physical Review B](#) **72**, 064413 (2005).
- [277] Y. Iqbal, T. Müller, P. Ghosh, M. J. P. Gingras, H. O. Jeschke, S. Rachel, J. Reuther, and R. Thomale, [Physical Review X](#) **9**, 011005 (2019).
- [278] H.-J. Schmidt, A. Lohmann, and J. Richter, [Physical Review B](#) **84**, 104443 (2011).
- [279] A. Lohmann, H.-J. Schmidt, and J. Richter, [Physical Review B](#) **89**, 014415 (2014).
- [280] K. Kanô and S. Naya, [Progress of Theoretical Physics](#) **10**, 158 (1953).
- [281] B. Bernu and G. Misguich, [Physical Review B](#) **63**, 134409 (2001).
- [282] G. Misguich and B. Bernu, [Physical Review B](#) **71**, 014417 (2005).

- [283] H.-J. Schmidt, A. Hauser, A. Lohmann, and J. Richter, [Physical Review E **95**, 042110 \(2017\)](#).
- [284] O. Benton, O. Sikora, and N. Shannon, [Physical Review B **86**, 075154 \(2012\)](#).
- [285] F. Desrochers, L. E. Chern, and Y. B. Kim, [Physical Review B **105**, 035149 \(2022\)](#).
- [286] R. Sibille, E. Lhotel, V. Pomjakushin, C. Baines, T. Fennell, and M. Kenzelmann, [Physical Review Letters **115**, 097202 \(2015\)](#).
- [287] S. W. Lovesey and G. van der Laan, [Physical Review B **101**, 144419 \(2020\)](#).
- [288] L. Savary, K. A. Ross, B. D. Gaulin, J. P. C. Ruff, and L. Balents, [Physical Review Letters **109**, 167201 \(2012\)](#).
- [289] K. A. Ross, Y. Qiu, J. R. D. Copley, H. A. Dabkowska, and B. D. Gaulin, [Physical Review Letters **112**, 057201 \(2014\)](#).
- [290] J. Robert, E. Lhotel, G. Remenyi, S. Sahling, I. Mirebeau, C. Decorse, B. Canals, and S. Petit, [Physical Review B **92**, 064425 \(2015\)](#).
- [291] J. D. Thompson, P. A. McClarty, D. Prabhakaran, I. Cabrera, T. Guidi, and R. Coldea, [Physical Review Letters **119**, 057203 \(2017\)](#).
- [292] A. Scheie, J. Kindervater, S. Zhang, H. J. Changlani, G. Sala, G. Ehlers, A. Heinemann, G. S. Tucker, S. M. Koochpayeh, and C. Broholm, [Proceedings of the National Academy of Sciences **117**, 27245 \(2020\)](#).
- [293] A. Kiss and P. Fazekas, [Physical Review B **71**, 054415 \(2005\)](#).
- [294] P. Santini, S. Carretta, G. Amoretti, R. Caciuffo, N. Magnani, and G. H. Lander, [Reviews of Modern Physics **81**, 807 \(2009\)](#).
- [295] Y. Kuramoto, H. Kusunose, and A. Kiss, [Journal of the Physical Society of Japan **78**, 072001 \(2009\)](#).
- [296] P. Chandra, P. Coleman, and R. Flint, [Physical Review B **91**, 205103 \(2015\)](#).
- [297] H. Otake, A. Nakamura, T. Yamashita, and K. Minato, [Journal of Physics and Chemistry of Solids Proceedings of the 11th International Conference on High Temperature Materials Chemistry \(HTMC-XI\), **66**, 329 \(2005\)](#).
- [298] M. Powell, L. D. Sanjeewa, C. D. McMillen, K. A. Ross, C. L. Sarkis, and J. W. Kolis, [Cryst. Growth Des. **7**, 4920 \(2019\)](#).
- [299] B. Tang, D. Iyer, and M. Rigol, [Physical Review B **91**, 174413 \(2015\)](#).

- [300] E. Lhotel, S. Petit, S. Guitteny, O. Florea, M. Ciomaga Hatnean, C. Colin, E. Ressouche, M. R. Lees, and G. Balakrishnan, [Physical Review Letters **115**, 197202 \(2015\)](#).
- [301] J. Xu, O. Benton, V. K. Anand, A. T. M. N. Islam, T. Guidi, G. Ehlers, E. Feng, Y. Su, A. Sakai, P. Gegenwart, and B. Lake, [Physical Review B **99**, 144420 \(2019\)](#).
- [302] A. Yaouanc, P. Dalmas de Réotier, C. Marin, and V. Glazkov, [Physical Review B **84**, 172408 \(2011\)](#).
- [303] K. A. Ross, T. Proffen, H. A. Dabkowska, J. A. Quilliam, L. R. Yaraskavitch, J. B. Kycia, and B. D. Gaulin, [Physical Review B **86**, 174424 \(2012\)](#).
- [304] R. M. D'Ortenzio, H. A. Dabkowska, S. R. Dunsiger, B. D. Gaulin, M. J. P. Gingras, T. Goko, J. B. Kycia, L. Liu, T. Medina, T. J. Munsie, D. Pomaranski, K. A. Ross, Y. J. Uemura, T. J. Williams, and G. M. Luke, [Physical Review B **88**, 134428 \(2013\)](#).
- [305] K. E. Arpino, B. A. Trump, A. O. Scheie, T. M. McQueen, and S. M. Koohpayeh, [Physical Review B **95**, 094407 \(2017\)](#).
- [306] A. Mostaed, G. Balakrishnan, M. R. Lees, Y. Yasui, L.-J. Chang, and R. Beanland, [Physical Review B **95**, 094431 \(2017\)](#).
- [307] Z. Shafieizadeh, Y. Xin, S. M. Koohpayeh, Q. Huang, and H. Zhou, [Scientific Reports **8**, 17202 \(2018\)](#).
- [308] A. M. Hallas, J. Gaudet, N. P. Butch, M. Tachibana, R. S. Freitas, G. M. Luke, C. R. Wiebe, and B. D. Gaulin, [Physical Review B **93**, 100403 \(2016\)](#).
- [309] A. M. Hallas, J. Gaudet, N. P. Butch, G. Xu, M. Tachibana, C. R. Wiebe, G. M. Luke, and B. D. Gaulin, [Physical Review Letters **119**, 187201 \(2017\)](#).
- [310] H. Yan, O. Benton, L. Jaubert, and N. Shannon, [Physical Review B **95**, 094422 \(2017\)](#).
- [311] S. Petit, E. Lhotel, F. Damay, P. Boutrouille, A. Forget, and D. Colson, [Physical Review Letters **119**, 187202 \(2017\)](#).
- [312] C. L. Sarkis, J. G. Rau, L. D. Sanjeewa, M. Powell, J. Kolis, J. Marbey, S. Hill, J. A. Rodriguez-Rivera, H. S. Nair, D. R. Yahne, S. Säubert, M. J. P. Gingras, and K. A. Ross, [Physical Review B **102**, 134418 \(2020\)](#).
- [313] B. Placke, R. Moessner, and O. Benton, [Phys. Rev. B **102**, 245102 \(2020\)](#).
- [314] R. R. Sobral and C. Lacroix, [Solid State Communications **103**, 407 \(1997\)](#).
- [315] F. J. Burnell, S. Chakravarty, and S. L. Sondhi, [Physical Review B **79**, 144432 \(2009\)](#).
- [316] H. C. Jiang, Z. Y. Weng, and D. N. Sheng, [Physical Review Letters **101**, 117203 \(2008\)](#).

- [317] S. Yan, D. A. Huse, and S. R. White, [Science](#) **332**, 1173 (2011).
- [318] H.-C. Jiang, Z. Wang, and L. Balents, [Nature Physics](#) **8**, 902 (2012).
- [319] S. Depenbrock, I. P. McCulloch, and U. Schollwöck, [Physical Review Letters](#) **109**, 067201 (2012).
- [320] Y.-C. He, M. P. Zaletel, M. Oshikawa, and F. Pollmann, [Physical Review X](#) **7**, 031020 (2017).
- [321] R. M. Noack and S. R. Manmana, [AIP Conference Proceedings](#) **789**, 93 (2005).
- [322] V. R. Chandra and J. Sahoo, [Physical Review B](#) **97**, 144407 (2018).
- [323] I. P. McCulloch, [Journal of Statistical Mechanics: Theory and Experiment](#) **2007**, P10014 (2007).
- [324] C. Hubig, I. P. McCulloch, U. Schollwöck, and F. A. Wolf, [Physical Review B](#) **91**, 155115 (2015).
- [325] C. Hubig, F. Lachenmaier, N.-O. Linden, T. Reinhard, L. Stenzel, A. Swoboda, and M. Grundner, [The SYTEN toolkit](#).
- [326] C. Hubig, *Symmetry-Protected Tensor Networks*, [Ph.D. thesis](#), LMU München (2017).
- [327] J. Ummethum, J. Schnack, and A. M. Läuchli, [Journal of Magnetism and Magnetic Materials](#) **327**, 103 (2013).
- [328] C. Hubig, J. Haegeman, and U. Schollwöck, [Physical Review B](#) **97**, 045125 (2018).
- [329] M. Hering, V. Noculak, F. Ferrari, Y. Iqbal, and J. Reuther, [Physical Review B](#) **105**, 054426 (2022).
- [330] R. Moessner, [Journal of Physics: Conference Series](#) **145**, 012001 (2009).
- [331] M. Udagawa, M. Ogata, and Z. Hiroi, [Journal of the Physical Society of Japan](#) **71**, 2365 (2002).
- [332] K. Matsuhira, Z. Hiroi, T. Tayama, S. Takagi, and T. Sakakibara, [Journal of Physics: Condensed Matter](#) **14**, L559 (2002).
- [333] R. Moessner and S. L. Sondhi, [Physical Review B](#) **68**, 064411 (2003).
- [334] J. Schulenburg, A. Honecker, J. Schnack, J. Richter, and H.-J. Schmidt, [Physical Review Letters](#) **88**, 167207 (2002).
- [335] U. Schollwöck, J. Richter, D. J. J. Farnell, and R. F. Bishop, eds., *Quantum Magnetism*, Lecture Notes in Physics, Vol. 645 (Springer, Berlin, Heidelberg, 2004).

- [336] A. Honecker, J. Schulenburg, and J. Richter, *Journal of Physics: Condensed Matter* **16**, S749 (2004).
- [337] K. Penc, N. Shannon, and H. Shiba, *Physical Review Letters* **93**, 197203 (2004).
- [338] A. Honecker, D. C. Cabra, M. D. Grynberg, P. C. W. Holdsworth, P. Pujol, J. Richter, D. Schmalfuß, and J. Schulenburg, *Physica B: Condensed Matter Proceedings of the International Conference on Strongly Correlated Electron Systems*, **359-361**, 1391 (2005).
- [339] J. Schnack, H.-J. Schmidt, A. Honecker, J. Schulenburg, and J. Richter, *Journal of Physics: Conference Series* **51**, 43 (2006).
- [340] O. Derzhko, J. Richter, A. Honecker, and H.-J. Schmidt, *Low Temperature Physics* **33**, 745 (2007).
- [341] T. Sakai and H. Nakano, *Physical Review B* **83**, 100405 (2011).
- [342] S. Nishimoto, N. Shibata, and C. Hotta, *Nature Communications* **4**, 2287 (2013).
- [343] S. Capponi, O. Derzhko, A. Honecker, A. M. Läuchli, and J. Richter, *Physical Review B* **88**, 144416 (2013).
- [344] H. Nakano and T. Sakai, *Journal of the Physical Society of Japan* **83**, 104710 (2014).
- [345] S. Capponi, *Physical Review B* **95**, 014420 (2017).
- [346] X. Plat, T. Momoi, and C. Hotta, *Physical Review B* **98**, 014415 (2018).
- [347] S. Pal and S. Lal, *Physical Review B* **100**, 104421 (2019).
- [348] M. E. Zhitomirsky, A. Honecker, and O. A. Petrenko, *Physical Review Letters* **85**, 3269 (2000).
- [349] D. L. Bergman, R. Shindou, G. A. Fiete, and L. Balents, *Physical Review Letters* **96**, 097207 (2006).
- [350] M. E. Zhitomirsky and H. Tsunetsugu, *Physical Review B* **75**, 224416 (2007).
- [351] T. Coletta, M. E. Zhitomirsky, and F. Mila, *Physical Review B* **87**, 060407 (2013).
- [352] H. Nakano and T. Sakai, *Journal of the Physical Society of Japan* **87**, 063706 (2018).
- [353] X. Chen, S.-J. Ran, T. Liu, C. Peng, Y.-Z. Huang, and G. Su, *Science Bulletin* **63**, 1545 (2018).
- [354] J. F. Nagle, *Physical Review* **152**, 190 (1966).
- [355] L. Vanderstraeten, B. Vanhecke, and F. Verstraete, *Physical Review E* **98**, 042145 (2018).

- [356] E. Shender, [Journal of Experimental and Theoretical Physics](#) (1982).
- [357] C. L. Henley, [Journal of Applied Physics](#) **61**, 3962 (1987).
- [358] H. Ueda, H. A. Katori, H. Mitamura, T. Goto, and H. Takagi, [Physical Review Letters](#) **94**, 047202 (2005).
- [359] O. Tchernyshyov, R. Moessner, and S. L. Sondhi, [Physical Review Letters](#) **88**, 067203 (2002).
- [360] T. Yavors’kii, T. Fennell, M. J. P. Gingras, and S. T. Bramwell, [Physical Review Letters](#) **101**, 037204 (2008).
- [361] P. H. Conlon and J. T. Chalker, [Physical Review B](#) **81**, 224413 (2010).
- [362] W. Brenig and A. Honecker, [Physical Review B](#) **65**, 140407 (2002).
- [363] J.-B. Fouet, M. Mambrini, P. Sindzingre, and C. Lhuillier, [Physical Review B](#) **67**, 054411 (2003).
- [364] Y.-H. Chan, Y.-J. Han, and L.-M. Duan, [Phys. Rev. B](#) **84**, 224407 (2011).
- [365] R. F. Bishop, P. H. Y. Li, D. J. J. Farnell, J. Richter, and C. E. Campbell, [Phys. Rev. B](#) **85**, 205122 (2012).
- [366] P. Sindzingre, J.-B. Fouet, and C. Lhuillier, [Phys. Rev. B](#) **66**, 174424 (2002).
- [367] S. Sachdev and R. N. Bhatt, [Phys. Rev. B](#) **41**, 9323 (1990).
- [368] J. Romhányi and K. Penc, [Phys. Rev. B](#) **86**, 174428 (2012).

CONFIRMATION

MAGNETIC FRUSTRATION IN THREE DIMENSIONS

Robin Schäfer

Confirmation

I herewith declare that I have produced this paper without the prohibited assistance of third parties and without making use of aids other than those specified; notions taken over directly or indirectly from other sources have been identified as such. This paper has not previously been presented in identical or similar form to any other German or foreign examination board. The thesis was produced in Dresden under the scientific supervision of Roderich Moessner.

Ort, Datum

.....
(Robin Schäfer)